



Dottorato di Ricerca in Ingegneria Civile
Graduate School in Civil Engineering

Sede: Facoltà di Ingegneria - Università di Pavia - via Ferrata 1 – 27100 Pavia – Italy

Dottorato di Ricerca in Ingegneria Civile VIII Nuova serie (XXV Ciclo)

**Non-Contact High-Precision Positioning Systems
for Structural Monitoring**

Tesi di Dottorato
Ing. Li Jun Wu

Advisor:
Prof. Fabio Casciati

Revisor:
Prof. Lucia Faravelli

Pavia, May, 2013

To My Parents, My Husband and My Dear Son

Acknowledgements

I take this opportunity to extend my heartfelt thanks to Professor Fabio Casciati for constantly providing his enthusiastic support, scientific knowledge, patient guidance, and human experience during the whole Ph.D. study period, and for his useful and valuable suggestions and encouragement in the preparation of this thesis. Without his support, the opportunities to broad my knowledge boundary by participating several conferences and summer school, and by visiting other outstanding Universities, would have been missed. The detailed revisions, friendly collaboration and human experience from Prof. Fabio Casciati, Prof. Lucia Faravelli, and Doctor Sara Casciati are also greatly acknowledged. I would like to express my profound gratitude to Professor Ying Lei for his constant encouragement and support.

I also would like to address appreciations to my colleagues for helping me with various aspects of my life and research in the university of Pavia, including the colleagues from the department of structural mechanics: Matilde Notarangelo, Daniele Bortoluzzi, Clement Fuggini, Raed Alsaleh, Alessandro Marzi, Paolo Basso, Krzysztof Hinc, Umut Yildirim, and Lorenzo Elia; the colleagues from department of hydraulic and environmental engineering: Alessandro Abbà, Barbara Marianna Crotti, Veronica Cornalba and Matteo Canato.

The support of my family is gratefully acknowledged. Especially, I would like to address my grateful to my parents who insist their daughter should be educated as well. I also would like to thank my parents-in-law who take care for my dear little son and allow me to focus on my thesis work. Lastly, I would like to thank my husband ZhiCong Chen for his constant support, encouragement, and inspiration.

Description of the Graduate School

Settore: Field:	Ingegneria Engineering
Sede Amministrativa non consortile: Administrative location:	Università degli Studi di Pavia University of Pavia
Durata del dottorato: Duration:	3 anni 3 years
Periodo formativo estero: Period in foreign organization:	come previsto dal regolamento del Dottorato di Ricerca as required by the school's rules
Numero minimo di corsi: Minimum number of courses:	6 6

Recapiti - Addresses



Dipartimento di Meccanica Strutturale
via Ferrata 1 - 27100 Pavia - Italy
Tel. 0382 / 505450 Fax 0382 / 528422



Dipartimento di Ingegneria Idraulica e Ambientale
via Ferrata 1 - 27100 Pavia - Italy
Tel. 0382 / 505300 Fax 0382 / 505589

Coordinatore – Coordinator

CASCIATI Fabio - Professore Ordinario di Scienza delle Costruzioni (ICAR/08)

Dipartimento di Meccanica Strutturale

via Ferrata 1 - 27100 Pavia – Italy Tel. 0382 / 505458 Fax 0382 / 528422
e-mail: fabio@dipmec.unipv.it

Collegio dei Docenti – Teaching Staff

CIAPONI Carlo	Professore Straordinario (ICAR/02)
DEL GROSSO Andrea	Professore Ordinario, Unige (ICAR/09)
FARAVELLI Lucia	Professore Ordinario (ICAR/08)
GALLATI Mario	Professore Ordinario (ICAR/01)
GOBETTI Armando	Professore Associato (ICAR/08)
MOISELLO Ugo	Professore Ordinario (ICAR/02)
PAPIRI Sergio	Professore Associato (ICAR/02)
SALA Roberto	Professore Associato (ING-IND/08)
MARCELLINI Alberto	Dirigente di Ricerca. CNR – Milano

Organizzazione del corso

Il dottorato di ricerca in *Ingegneria Civile* presso la Scuola di Dottorato in Scienze dell'Ingegneria dell'Università degli Studi di Pavia è stato istituito nell'anno accademico 1994/95 (X ciclo).

Il corso consente al dottorando di scegliere tra quattro curricula: idraulico, sanitario, sismico e strutturale. Il dottorando svolge la propria attività di ricerca presso il Dipartimento di Ingegneria Idraulica e Ambientale per i primi due curricula o quello di Meccanica Strutturale per gli ultimi due.

Durante i primi due anni sono previsti almeno sei corsi, seguiti da rispettivi esami, che il dottorando è tenuto a sostenere. Il Collegio dei Docenti, composto da professori dei due Dipartimenti e da alcuni esterni all'Università di Pavia, organizza i corsi con lo scopo di fornire allo studente di dottorato opportunità di approfondimento su alcune delle discipline di base per le varie componenti. Corsi e seminari vengono tenuti da docenti di Università nazionali ed estere.

Il Collegio dei Docenti, cui spetta la pianificazione della didattica, si è orientato ad attivare ad anni alterni corsi sui seguenti temi:

- Meccanica dei solidi e dei fluidi
- Metodi numerici per la meccanica dei solidi e dei fluidi
- Rischio strutturale e ambientale
- Metodi sperimentali per la meccanica dei solidi e dei fluidi
- Intelligenza artificiale

più corsi specifici di indirizzo.

Al termine dei corsi del primo anno il Collegio dei Docenti assegna al dottorando un tema di ricerca da sviluppare sotto forma di tesina entro la fine del secondo anno; il tema, non necessariamente legato all'argomento della tesi finale, è di norma coerente con il curriculum, scelto dal dottorando.

All'inizio del secondo anno il dottorando discute con il Coordinatore l'argomento della tesi di dottorato, la cui assegnazione definitiva viene deliberata dal Collegio dei Docenti.

Alla fine di ogni anno i dottorandi devono presentare una relazione particolareggiata (scritta e orale) sull'attività svolta. Sulla base di tale relazione

il Collegio dei Docenti, "previa valutazione della assiduità e dell'operosità dimostrata dall'iscritto", ne propone al Rettore l'esclusione dal corso o il passaggio all'anno successivo.

Il dottorando può svolgere attività di ricerca sia di tipo teorico che sperimentale, grazie ai laboratori di cui entrambi i Dipartimenti dispongono, nonché al Laboratorio Numerico di Ingegneria delle Infrastrutture.

Il “Laboratorio didattico sperimentale” del Dipartimento di Meccanica Strutturale dispone di:

1. una tavola vibrante che consente di effettuare prove dinamiche su prototipi strutturali;
2. opportuni sensori e un sistema di acquisizione dati per la misura della risposta strutturale;
3. strumentazione per la progettazione di sistemi di controllo attivo e loro verifica sperimentale;
4. strumentazione per la caratterizzazione dei materiali, attraverso prove statiche e dinamiche.

Il laboratorio del Dipartimento di Ingegneria Idraulica e Ambientale dispone di:

1. un circuito in pressione che consente di effettuare simulazioni di moto vario;
2. un tunnel idrodinamico per lo studio di problemi di cavitazione;
3. canalette per lo studio delle correnti a pelo libero.

Course Organization

The Graduate School of Civil Engineering, a branch of the Doctorate School in Engineering Science, was established at the University of Pavia in the Academic Year of 1994/95 (X cycle). The School allows the student to select one of the four offered curricula: Hydraulics, Environment, Seismic Engineering and Structural Mechanics. Each student develops his research activity either at the Department of Hydraulics and Environmental Engineering or at the Department of Structural Mechanics. During the first two years, a minimum of six courses must be selected and their examinations successfully passed. The Faculty, made by Professors of the two Departments and by internationally recognized external scientists, organizes courses and provides the students with opportunities to enlarge their basic knowledge. Courses and seminars are held by University Professors from all over the country and abroad. The Faculty starts up, in alternate years, common courses on the following subjects:

- solid and fluid mechanics,
- numerical methods for solid and fluid mechanics,
- structural and environmental risk,
- experimental methods for solid and fluid mechanics,
- artificial intelligence.

More specific courses are devoted to students of the single curricula.

At the end of each course, for the first year the Faculty assigns the student a research argument to develop, in the form of report, by the end of the second year; the topic, not necessarily part of the final doctorate thesis, should be consistent with the curriculum selected by the student. At the beginning of the second year the student discusses with his Coordinator the subject of the thesis and, eventually, the Faculty assigns it to the student. At the end of every year, the student has to present a complete report on his research activity, on the basis of which the Faculty proposes to the Rector his admission to the next academic year or to the final examination. The student is supposed to develop either theoretical or experimental research activities, and therefore has access to the

Department Experimental Laboratories, even to the Numerical Laboratory of Infrastructure Engineering. The Experimental Teaching Laboratory of the Department of Structural Mechanics offers:

1. a shaking table which permits one to conduct dynamic tests on structural prototypes;
2. sensors and acquisition data system for the structural response measurements;
3. instrumentation for the design of active control system and their experimental checks;
4. an universal testing machine for material characterization through static and dynamic tests.

The Department of Hydraulics and Environmental Engineering offers:

1. a pressure circuit simulating various movements;
2. a hydrodynamic tunnel studying cavitation problems;
3. a micro-channels studying free currents.

Elenco delle tesi – Previous PhD Theses

Marco Battaini (X ciclo)	Sistemi strutturali controllati: progettazione e affidabilità. (February 1998).
Claudia Mariani (X ciclo)	Problemi di ottimizzazione per strutture bidimensionali anisotrope. (February 1998).
Antonella Negri (X ciclo)	Stima delle perdite idrologiche nei bacini di drenaggio urbani. (February 1999).
Aurora Angela Pisano (XI ciclo)	Structural System Identification: Advanced Approaches and Applications. (February 1999).
Carla Saltalippi (XI ciclo)	Preannuncio delle piene in tempo reale nei corsi d'acqua naturali. (February 1999).
Eugenio Barbieri (XI ciclo)	Thermo fluid Dynamics and Topology: Optimization of an Active Thermal Insulation Structure. (February 2000).
Barbolini Massimiliano (XII ciclo)	Dense Snow Avalanches: Computational Models, Hazard Mapping and Related Uncertainties. (February 2000).
Espa Paolo (XII ciclo)	Moti atmosferici generati da forze di galleggiamento: simulazioni numeriche e studio su modello fisico. (February 2000).
Petrini Lorenza (XII ciclo)	Shape Memory Alloys: Modelling the Martensitic Phase Behaviour for Structural Engineering Exploitation. (February 2000).
Podestà Stefano (XIV ciclo)	Risposta sismica di antichi edifici religiosi: una nuova proposta per un modello di vulnerabilità. (February 2002).

Sturla Daniele (XIV ciclo)	Simulazioni lagrangiane di flussi rapidamente variati nell'approssimazione di acque poco profonde. (February 2002).
Marazzi Francesco (XV ciclo)	Semi-active Control of Civil Structures: Implementation Aspects. (February 2003).
Nascimbene Roberto (XV ciclo)	Sail Modelling for Maximal Speed Optimum Design. (February 2003).
Giudici Massimo (XVI ciclo)	Progettazione in regime non lineare di strutture in CAP a cavi aderenti e non aderenti. (February 2004).
Mutti Matteo (XVI ciclo)	Stability Analysis of Stratified Three-phase Flows in Pipes. (February 2004).
Petaccia Gabriella (XVI ciclo)	Propagazione di onde a fronte ripido per rottura di sbarramenti in alvei naturali. (February 2004).
Casciati Sara (XVII ciclo)	Damage Detection and Localization in the Space of the Observed Variables. (February 2005).
D'Amico Tiziana (XVI ciclo)	Ricerca e sviluppo di metodologie diagnostiche per il recupero di edifici monumentali: prove vibroacustiche sul tufo. (February 2005).
Barco Olga Janet (XVII ciclo)	Modeling the Quantity and Quality of Storm Water Runoff Using SWMM. (February 2005).
Boguniewicz Joanna (XVIII ciclo)	Integration of Monitoring and Modelling in the Surface Water State Evaluation Process of a Sub-Alpine Lake Watershed. (February 2006).
Bornatici Laura (XVIII ciclo)	L'impiego degli algoritmi generici per la risoluzione dei problemi di progetto di reti di distribuzione idrica. (February 2006).

Collivignarelli Maria Cristina (XVIII ciclo)	Trattamento di rifiuti liquidi mediante processi biologici aerobici termofili e mesofili e processi avanzati di ossidazione chimica in diversa. (February 2006).
Domaneschi Marco (XVIII ciclo)	Structural Control of Cable-stayed and Suspended Bridges. (February 2006).
Ráduly Botond (XVIII ciclo)	Artificial Neural Network applications in Urban Water Quality Modeling. (February 2006).
Cappabianca Federica (XVIII attraverso ciclo)	La valutazione del rischio valanghivo la modellazione dinamica. (February 2006).
Callegari Arianna (XVIII ciclo)	Applicazione di tecnologie di monitoraggio on-line per la gestione dei processi di trattamento reflui. (February 2006).
Gazzola Elisa (XVIII ciclo)	Applicazione di processi biologici anaerobici al trattamento di acque reflue e fanghi di depurazione: aspetti tecnici ed energetici. (February 2006).
Antoci Carla (XVIII ciclo)	Simulazione numerica dell'interazione fluido-struttura con la tecnica SPH. (July 2006).
Giuliano Fabio (XIX ciclo)	Performance Based Design and Structural Control for Cable Suspension Bridges. (February 2007).
Maranca Federica (XVIII ciclo)	Valutazione del ciclo di vita (LCA): confronto tra sistemi di trasporto gas via gasdotto. (February 2007).
Falappi Stefano (XIX ciclo)	Simulazioni numeriche di flussi di fluidi viscosi e materiali granulari con la tecnica SPH (February 2007).
Zanaboni Sabrina (XIX ciclo)	Pre-trattamento di rifiuti liquidi industriali mediante ossidazione ad umido. (February 2007).

Matteo Bruggi (XX ciclo)	Topology optimization using mixed finite elements. (February 2008).
Gian Paolo Cimellaro (XX ciclo)	Passive Control of Industrial Structures for Natural Hazard Mitigation: Analytical Studies and Applications. (February 2008).
Alessandro Abbà (XXI ciclo)	Il recupero dei rifiuti speciali nel settore delle costruzioni: studio delle possibilità di recupero e valutazione dei meccanismi di lisciviazione. (February 2009).
Karim Hamdaoui (XXI ciclo)	Experimental Applications on Cu-based Shape Memory Alloys: Retrofitting of Historical Monuments and Base Isolation (February 2009).
Thomas Messervey (XXI ciclo)	Integration of Structural Health Monitoring into the Design, Assessment, and Management of Civil Infrastructure. (February 2009).
Filippo Ubertini (XXI ciclo)	Wind Effects on Bridges: Response, Stability and Control. (February 2009).
Fuggini Clemente (XXII ciclo)	Using Satellites Systems for Structural Monitoring: Accuracy, Uncertainty, and Reliability. (February 2010).
Raboni Massimo (XXII ciclo)	Impiego di tecniche numeriche e sperimentali per l'analisi di fenomeni multiphysics. (July 2010).
Alessandro Marzi (XXIII ciclo)	Impianti in materiale plastic per il trasporto dei fluidi nel settore navale. (February 2010).
Barbara Marianna Crotti (XXIII ciclo)	Verifiche di funzionalità e criteri di ottimizzazione degli impianti di potabilizzazione: alcuni casi di studio. (February 2010)
Luigi Franchioli (XXIII ciclo)	Analisi prestazionale dei sistemi di distribuzione idrica e calcolo della loro affidabilità. (February 2010)

Raed Alsaleh (XXIII ciclo)	Verification of Wind Pressure and Wind Induced Response of a Supertall Structure Using a Long Term Structural Health Monitoring System. (February 2010).
Emanuela Torti (XXIV ciclo)	Experimental and numerical analysis of a confined two-phase turbulent jet system. (December 2011).
Sidi Mohammed El-Amine Bourdim (XXIV ciclo)	Diagnosis and Seismic Analysis of a Historical Monument in Tlemcen. (December 2011).
Veronica Cornalba (XXIV Ciclo)	Recupero energetico da biomasse: aspetti tecnici e di impatto ambientale. (December 2011).
Zhicong Chen (XXIV ciclo)	Structural Monitoring and System Control Using a Wireless Sensor Network. (December 2011)
Paolo Basso (XXIV ciclo)	Optimal form-finding algorithms for the control of structural shapes. (June 2012).
Matteo Canato (XXV ciclo)	Tecniche innovative per il trattamento/recupero dei fanghi di depurazione delle acque reflue urbane. (December, 2012).
Roberta Pernetti (XXV ciclo)	Problematiche relative alla definizione e all'utilizzo di modelli delle prestazioni energetiche di edifici esistenti. (December, 2012).

Table of Contents

List of Figures.....	3
List of Tables.....	8
Abbreviations	9
Abstract.....	11
Chapter 1 Introduction.....	13
1.1 Background	13
1.2 State of the art	15
1.2.1 Wireless communication and self-positioning system.....	15
1.2.2 Positioning sensors.....	17
1.2.3 Vision-based LPS.....	22
1.3 Content and organization of this thesis	24
Chapter 2 Wireless Global Positioning System.....	27
2.1 Introduction.....	27
2.2 Leica GPS receiver system	29
2.2.1 The interface between receiver and computer	30
2.2.2 The power consumption of GRX 1200	31
2.2.3 Server and software.....	32
2.3 Wireless GPS data logger	33
2.3.1 24XStream	34
2.3.2 CC1110	36
2.3.3 Power consumption of CC1110	39
2.4 Experiment.....	39
Chapter 3 Wireless Laser-based Local Positioning System	45
3.1 Introduction.....	45
3.2 Hardware of the wireless laser-based LPS unit	46
3.2.1 The laser sensor YT89MGV80	48
3.2.2 The first version of wireless DAQ system	50
3.2.3 The updated version of the wireless DAQ system.....	53
3.3 Firmware design of the wireless sensing unit.....	54
Signal Processing Methods.....	58
3.4.1 The noise in wireless DAQ system	59
3.4.2 Moving average filter	60

3.4.3 Gaussian filter.....	61
3.4.4 Spectral subtraction methods.....	62
3.5 Experimental validation	63
3.5.1 Static experiments	64
3.5.2 Kinematic experiments.....	68
Chapter 4 Vision based Local Positioning System	75
4.1 Introduction	75
4.2 Theory and methodologies	77
4.2.1 2D projective geometry and camera model.....	77
4.2.2 2D direct linear transformation (DLT).....	85
4.2.3 Registration.....	88
4.2.4 Image processing routine.....	90
4.3 Operating Principle of a Digital Camera.....	93
4.3.1 CCD digital camera	93
4.3.2 The camera	97
4.4 Software implementation	97
4.4.1 Image acquisition.....	98
4.4.2 Image processing	101
4.5 Experimental validation	106
4.5.1 Feasibility of a vision-based system for displacement measurement.....	106
4.5.2 Performance of a vision-based displacement measurement system.....	110
Chapter 5 Conclusions and Future Directions	139
Bibliography	143

List of Figures

Figure1.1 Local Positioning System (LPS)	19
Figure1.2 Schematic representation of the adoption of repeaters toward LPS	21
Figure2.1 Scheme of a GPS receiver.....	28
Figure2.2 The GPS receiver system for GRX 1200 (elaborated form (Leica Geosystems AG 2010)).	30
Figure2. 3 The local site server interface of the software GPS Spider.	33
Figure2. 4 The objective of the wireless connection for the GPS system.	34
Figure2. 5 24XStream wireless links.....	35
Figure2. 6 X-CTU display window.	35
Figure2. 7 The block diagram of the wireless GPS system.....	37
Figure2. 8 Main loop.	37
Figure2. 9 (a) Radio reception interrupt service routine (ISR),(b) UART receive ISR.	38
Figure2. 10 Radio send.	39
Figure2. 11 The real-time tracking result of the GPS receiver.....	40
Figure2. 12 The real time tracking and positioning results of the GPS receiver.	41
Figure2. 13 The quality check report from GNSS QC V2.0.	41
Figure2. 14 The raw data status of GRX 1200-pro (by GNSS SPIDER software).	42
Figure2. 15 The quality check report (by GNSS QC V2.0).	42
Figure2. 16 The real-time tracked satellites (by GNSS Spider).	43
Figure3. 1 Diagram of the wireless signal collection board.....	47
Figure3. 2 Sensing range of the YT89MGV80.	49
Figure3. 3 Component level block diagram (Top) and prototype (Bottom) of the wireless sensing unit.....	51
Figure3. 4 Block Diagram of the Power management.	52
Figure3. 5 Prototype of the Power Management Module.	52
Figure3. 6 the PMOS AO3401	53
Figure3. 7 Transmitting a packet in reliable mode.....	55

Figure3. 8 Receiving a Packet in Reliable Mode.....	56
Figure3. 9 Wireless Sensing Unit Software Flowchart.....	57
Figure3. 10 Command Unit firmware flowchart	58
Figure3. 11 Frequency response of the moving average filter.....	61
Figure3. 12 The noise of first version of wireless DAQ system (red) and the corresponding wireless laser sensor (blue).....	64
Figure3. 13 The noises of the updated version of Wireless DAQ system (red) and of the updated wireless laser sensor (blue)..	65
Figure3. 14 Temperature drift of the laser sensor when the working distance is 750mm.....	66
Figure3. 15 Temperature drift of the laser sensor when the working distance is 1060mm.....	67
Figure3. 16 Temperature drift of the laser sensor when the working distance is 1350mm.....	67
Figure3. 17 The results of laser measurement before and after applying the moving average filter and Gaussian filter to the original signal which is obtained when the shaking table moves at 1Hz with the amplitude 1mm.....	69
Figure3. 18 Results of applying the moving average filter to the signal obtained when the shaking table moves following the signal $U_t = 0.4\sin\pi t + 0.2\sin 2\pi t + 0.1\sin 8\pi t$: (a) the recorded signal; (b) the filtered signal	70
Figure3. 19 Results of the moving average filter when the shaking table moves sinusoidally with an amplitude of 1mm and a frequency of 10Hz;	71
Figure3. 20 Performance of the spectral subtraction method-1.....	72
Figure3. 21 Performance of the spectral subtraction method-2.....	73
Figure 4. 1 the finite camera center (left) and the infinite camera center (right).....	75
Figure 4. 2 The pinhole camera model and the projective geometry	79
Figure 4. 3 Radial and tangential distortions	82
Figure 4. 4 effect of the radial distortion: solid lines, no distortion; dashed line, distortion	83

Figure 4. 5 Effect of the tangential distortion. Solid lines: no distortion; dashed lines: with tangential distortion.....	83
Figure 4. 6 Distortion distribution chart. Left: control plane, right: distortion distribution	84
Figure 4. 7 Forms of calibration: (a) extrapolation and (b) interpolation.....	88
Figure 4. 8 Distortions calibrated by the registration (a) translation (b) scale (c) shear (d) rotation.....	88
Figure 4. 9 Flow chart of the image processing procedure	90
Figure 4. 10 Block diagram of typical image application	93
Figure 4. 11 The influence of the lens focal length.....	94
Figure 4. 12 The relative light-gathering area for different apertures	95
Figure 4. 13 Diagram of wireless camera.....	96
Figure 4. 14 The displaying dialog.....	98
Figure 4. 15 The setup dialog	99
Figure 4. 16 Construction process of the image acquisition program	100
Figure 4. 17 The interaction of the three threads in the software..	101
Figure 4. 18 Preprocessing of the image to refine the image quality	102
Figure 4. 19 Image calibration through IPP6.0	103
Figure 4. 20 Segmentation through a color intensity feature	104
Figure 4. 21 Representation of potential objects	104
Figure 4. 22 Description of potential objects	105
Figure 4. 23 Photographs accounting for the initial position at rest. On the right side 4 markers are outlined.....	107
Figure 4. 24 The track of: (a) T1 (left-top); (b) T2 (right-top); (c) T3 (left-bottom); (d) T4 (Right-bottom); (The unit of x coordinate is the pixel)	107
Figure 4. 25 The maximum displacement of T1	108
Figure 4. 26 The instant when maximum shift occurred.....	108
Figure 4. 27 The vertical displacements of T1 and T2.....	109
Figure 4. 28 The vertical displacements of T3 and T4.....	109
Figure 4. 29 the calibration board.....	110

Figure 4. 30 The calibration of interpolation and extrapolation calibration based on the scale factor approach when the optical of camera is perpendicular to the image	111
Figure 4. 31 The calibration error of interpolation scale factor and interpolation DLT calibration when the optical of camera is perpendicular to the image.....	112
Figure 4. 32 Calibration results when the optical axis of camera is skewed with the image at a small angle.....	113
Figure 4. 33 Calibration results when the optical axis of the camera is skewed with the image at a large angle.....	114
Figure 4. 34 Performance of DLT under two skewed situations ..	115
Figure 4. 35 The GUI for configuring the tracking options.....	117
Figure 4. 36 Two markers too close each to the other	118
Figure 4. 37 Misjudgment for the two markers in Fig.4.36.....	118
Figure 4. 38 The markers tracked to examine the affection of different exposure times.....	119
Figure 4. 39 The observed fuzziness of the uppermost marker on the left column (a) the minimum fuzziness whose area is 15 pixels; (b) the maximum fuzziness whose area is 21 pixels.....	120
Figure 4. 40 The fuzziness introduced during exposure period when recording the motion	121
Figure 4. 41 The markers adhered on the frame	122
Figure 4. 42 Displacement of the markers on the bottom floor (perpendicular).....	123
Figure 4. 43 Spectra of the signal recorded for the markers on the bottom floor (perpendicular).....	124
Figure 4. 44 Displacement of the markers on the top floor (unit: mm VS Seconds) (perpendicular)	124
Figure 4. 45 Spectra of the signal recorded for the markers on the top floor (perpendicular)	125
Figure 4. 46 Displacements of the markers on the left column (perpendicular).....	125
Figure 4. 47 Spectra of the signal recorded for the markers on the left column (perpendicular).....	126

Figure 4. 48 Displacement of the markers on the left column (perpendicular).....	126
Figure 4. 49 Spectra of the signal recorded for markers on the left column (perpendicular).....	127
Figure 4. 50 The displacement of markers on the bottom (skewed)	127
Figure 4. 51 Spectra of the signals recorded for the markers on the bottom (skewed)	128
Figure 4. 52 The displacement of markers on the bottom (skewed)	128
Figure 4. 53 Spectra of the signals recorded for the markers on the bottom (skewed)	129
Figure 4. 54 The displacement of markers on the left column (skewed)	130
Figure 4. 55 The spectra of signals of markers on the left column (skewed)	130
Figure 4. 56 Image before and after registration	131
Figure 4. 57 The displacement of markers on the top floor (After registration).....	132
Figure 4. 58 Spectra of the displacement signal of the markers on the top floor (After registration)	132
Figure 4. 59 calibration board	133
Figure 4. 60 Markers distribution.....	134
Figure 4. 61 Track results (continued).....	136
Figure 4. 62 The movements of T2 (a) the horizontal direction (b) the vertical direction.	137

List of Tables

Table 2. 1 Features of the GRX 1200-pro receiver.....	31
Table 2. 2 The power consumption of the GRX 1200 pro receiver system.	32
Table 2. 3 Properties of the 24XStream RF Module (with 9600 bps throughput data rate)	34
Table 2. 4 Power consumption of the wireless transceiver based on the CC1110	39
Table3. 1 The properties of YT89MGV80	49
Table3. 2 Features of the LVDT sensor.....	68
Table3. 3 Features of the wireless DAQ systems	68
Table 4. 1 Typical uses of different focal lengths.....	95
Table 4. 2 The parameters of the SunTime FX30VC camera.....	97
Table 4. 3 The parameters of the lens for the SunTime FX30VC ..	97
Table 4. 4 The parameters of the SV642 camera.....	97
Table 4. 5 Portion of the commands of the macro <i>IpTrackMeasSet</i>	116
Table 4. 6 Coordinates of the points A-F.....	134

Abbreviations

ADC	Analogue to Digital Converter
AFE	Analogue Front-End
AGND	Analog Ground
AOI	Area of Interested
ARM	Advanced RISC Machines
ASIC	Application-Specific Integrated Circuit
AWGN	Additive White Gaussian Noise
CCD	Charge Coupled Device
CMOS	Complementary-Metal Oxide-Semiconductor
CORS	Continuously Operating Reference Station
CSB-SWC	Cable-Stayed Bridge in Shenzhen Western Corridor
CSS	Chirp Spread Spectrum
CLT	Central Limit Theorem
DAQ	Data Acquisition System
dBm	Decibel Milliwatt
DDS	Direct Digital Synthesis
DGND	Digital Ground
DLT	Direct Linear Transformation
DMA	Direct Memory Access
DMI	Displacement Measuring Interferometry
DRS	Displacement Recording Station
DSP	Digital Signal Processor
FMCW	Frequency Modulation Continuous Wave
FOV	Field of View
FPGA	Field-programmable Gate Array
FPS	Frames Per Second
FTP	File Transfer Protocol
GNSS	Global Navigation Survey Systems
GPS	Global Positioning System
GPU	Graphics processing unit
GUI	Graphic User Interface
IC	Integrate Circuit
IEEE	Institute of Electrical and Electronics Engineers
IF	Intermediate Frequency
INS	Inertial Navigation System
Intel® IPP	Intel® Integrated Performance Primitives

I/O	Input/Output
IPL	Image Processing Library
ISR	Interrupt Service Routine
IPP 6.0	Image Pro Plus 6.0
LASER	Light Amplification by Stimulated Emission of Radiation
LB2	Leica binary
LC filter	Inductor (L) Capacitor (C) filter
LDO	Low Dropout Regulator
LPS	Local Positioning System
LVDT	Linear Variable Differential Transformer
MAV	Moving Average Filter
MFC	Microsoft Foundation Classes
OpenCV	Open Source Computer Vision
OOP	Object-Oriented Program
PM	Power Modes
PMOS	P-Channel MOSFET, Metal-Oxide-Semiconductor Field-Effect Transistor
PCB	Printed Circuit Board
RAM	Random Access Memory
RF	Radio-Frequencies
RINEX	The Receiver Independent Exchange Format
RISC	Reduced Instruction Set Computing
RS 232	Recommended- Standard 232
RX	Receiver
SM	Structural Monitoring
SNR	Signal-Noise-Ratio
SoC	System-On-Chip
SRAM	Static Random-Access Memory
SVD	Singular Value Decomposition
TCXO	Temperature-Compensated Crystal Oscillator
TLS	Terrestrial Laser Scanner
TinyOS	Tiny Micro-threading Operating System
TOF	Time-Of-Flight
TX	Transceiver
UART	Universal Asynchronous Receiver/Transmitter
UML	Unified Modeling Language
UWB	Ultra Wide Band
WSN	Wireless Sensor Network

Abstract

SHM technologies utilize different types of sensors which are installed on the structure to be monitored and by recording its static or dynamic responses toward health diagnosis. The final goals are to detect and quantify damage, to promote a residual life-time prognosis of the structure and to guide the management in planning optimal cost-effective strategies for system maintenance, inspection, repair or rehabilitation. Employing a suitable data acquisition sensor network is a key implementation issue to link models with real world structures. A wireless sensor network, compared with a traditional wired network, provides easy installment and maintenance. Non-contact sensors could be easily installed on existing infrastructure in different scenes without changing their properties. A positioning system provides displacement information of the objects which is assumed to be the basic support to calibrate any structural mechanics model. These three attributes (wireless, non-contact, positioning) are the care of the thesis work. The thesis considers both global positioning system (GPS) and local positioning system (LPS) which includes laser-based and vision-based positioning system.

GPS provides satisfactory accuracy, absolute displacement measurement for SHM application. It requires an open area position to place the antennas but a roofed room to place its receiver and the power supply. At times, it is difficult to route cables between two positions due to the building constraint. In this work, two wireless links, which are based on the 24XStream and the CC1110 transmission systems, are applied to replace the cable transmission between the dual-frequency high precision GPS receiver and the user client computer which up to now was the only market offer. Some experiment results show a successful cable replacement. Limitations of GPS are obvious: open area is required and it is impossible to densely deploy GPS sensor due to the high cost of the devices. Hence, two low-cost LPS systems are discussed: laser-based wireless LPS and vision-based wired LPS.

The performance of the laser-based wireless LPS is studied and the possibility of increasing its accuracy by multiple readings and their differential elaboration is confirmed. Specially, two means are proposed to reduce the noise observed during the experiment: multiple reading with the help of signal processing (moving average filter, Gaussian filter and spectral subtraction) and an

improvement of the design of the wireless data acquisition (DAQ) system. The temperature compensation methodology is also studied. Some experiments results show that system performance is adequate for SHM.

LPS based on vision system is the last component of this work. This kind of system takes advantage of fast-developing digital image processing and computer vision technologies and is the new favorite non-contact sensor. Usually, the space coordinates is simply reconstructed from the image coordinates by multiplying a scale factor. Such simplified approach ignores the distortions introduced by projection and camera optical deficiency. To address these distortions, the camera model is first derived according to projection geometry. Based on the model, the camera calibration and the space coordinates' reconstruction methodologies are studied. A vision system, which covers a medium range investigation area, is constructed in this work to monitor the vibration of a reduced scale frame available in the laboratory.

Chapter 1 Introduction

1.1 Background

Among the research activities which address the development of smart materials and structures, Structural Health Monitoring (SHM) is a particularly promising branch. Structural monitoring technologies utilize different types of sensors which are installed on the structure to be monitored by recording its static deflection or its dynamic responses during forced vibration or natural excitation. The static deflection can be used for damage detection while the dynamic responses can be analyzed to identify the current status of the structure (Farrar and Worden 2007; Materazzi and Ubertini 2011; Ubertini 2013), which will be compared with its behaviors at healthy condition. Thus a health diagnosis of the structure can be performed to detect and quantify damage as well as to update its effects on the remaining integrity. All these will assist the structure and system manager toward the residual life-time prognosis and guide the management in planning optimal cost-effective strategies for system maintenance, inspection, repair or rehabilitation. By analyzing vibration data (caused by environmental interactions such as wind, mechanical and traffic loads) or severe vibration data (caused by earthquakes and strong winds), appropriate actuation can also be imposed on the structure in order to counteract the effect of severe loading event (Krommer, Irschik et al. 2005; Huber, Krommer et al. 2009; Schoeftner and Krommer 2012). In this way, the effective damage can be significant reduced (Ni, Chen et al. 2002; Faravelli, Fuggini et al. 2010; Ubertini 2010).

Uncertainties play an important role in the prediction of the safety of an infrastructure. The load and response uncertainties are quantified by adopting suitable sensor networks. As a key implementation issue to link the models with real world structures, the sensor network plays an important role in the usability and performance of any SHM system. Among several possible directions of SHM, sensor network, wireless, non-contact and positioning are three endearing directions and they are pursued in this work.

From a technological point of view, the main difficulties encountered in field applications are related to the cabling system: due to the high cost of the cables,

their difficulty of installation, their invasive effect on the monitored structure, their vulnerability to mechanical damage, and their high cost of maintenance. For these reasons, the adoption of wireless connections is regarded as a fundamental aspect for the spread of permanent monitoring solutions. Its feasibility is supported by the improving performance and declining cost of electronics and wireless communication technologies.

In view of reconstructing the stress and strain fields inside the medium, non-contact sensors are preferred. One of the main applications of SHM system is to monitor the existing structures which pose special constraints as the impossibility of using sensor networks installed during construction. Sensors, like LVDT, should be fixed to a reference point near the structure which could be difficult in the scenes of large-span bridges monitoring and high-stand towers monitoring. Experimental analysis of properly reduced scale models is utilized to obtain a better understanding of the behavior of large-scale structures. Conventional sensors sometimes are not feasible because the introduction of the sensor masses can affect the behavior of the models. For these reasons, there is growing interest in developing alternative techniques for measuring movement without any contact with the structure. Besides, non-contact sensors do not undergo the same force or deformation as the structure, they should be more durable.

All structural mechanics models assume the displacements as basic variables: to know the absolute displacements of a structural system means to dominate the structural response. The displacement are normally calculated by integrating the velocities obtained through velocimeter or by double integrating the accelerations obtained through accelerometer and such procedures introduce errors. Positioning system, which monitors the position of the object, directly provides the displacement information.

Based on the previous discussion, this work focuses on the positioning systems, both the global positioning system (GPS) and local positioning systems (LPS): laser-based and vision-based solutions. Wireless links are realized for high-precision GPS systems. The performance of a laser-based local positioning system is evaluated and the possibility of improving its resolution through difference from multiple readers is confirmed. A vision-based positioning system is also constructed for structure health monitoring and the image processing methodology is discussed to optimize the system performance. The camera calibration is discussed in detail.

1.2 State of the art

1.2.1 Wireless communication and self-positioning system

Current extensively monitoring systems are wire-based which is heavily time- and money-consuming while it encounters the requirement of dense deployment sensor network and the increasing scale of modern infrastructures. As an example, consider the Tsing Ma Suspension Bridge constructed in Hong Kong; a 600 channel structural monitoring system was installed at a cost of over \$16 million (Lynch, Sundararajan et al. 2003). The high cost of current structural monitoring systems results from labor intensive installation of system cables. Up to 25% of the total system cost and 75% of the installation time can be attributed solely to installation of systems cables. Also, wired monitoring systems would be too obtrusive for monitoring historic landmarks. In recent years, with the development of wireless communication, some academic and commercial wireless sensing systems have been proposed to eradicate the extensive lengths of wires associated with tethered systems.

Since 1990s, the research of wireless sensors has been reported by different research groups and several wireless hardwares have been designed (Lynch and Loh 2006). To provide good flexibility and extendibility, efforts focus on the network topological, the data-reducing methodology, the software system, the hardware improvement and the hardware interface flexibility. Thus they greatly improve the usability of the wireless sensor network.

In 2005, a star-topology wireless sensor system, WiMMS, was designed by Michigan University and Stanford University to work in both structural monitoring and structural control (Wang 2007; Wang, Lynch et al. 2007). This system utilizes 9XStream/24XStream transceiver which supports a single-hop data rate as 19.2kbps within several hundred meters: it cannot serve a large amount of sensors and this limits its application to large-scale infrastructure. The IEEE 802.15.4 standard and ZigBee protocol compliant wireless devices were regarded as promising alternatives: they support multiple topologies, including star, mesh and cluster tree, ensure a capacity of connecting more than 65,000 devices. The data rate is 250kbps at 2.4GHz. (Ergen 2004; Jin-Shyan, Yu-Wei et al. 2007). Thus, several IEEE 802.15.4/ZigBee based wireless networks are constructed for structure monitoring: Imote 2 from Illinois (Rice

and Spencer 2009), EMPA from DecentLab (Meyer, Bischoff et al. 2010), Narada from CIVIONICS (Swartz and Lynch 2009) and XMU unit (Lei, Liu et al. 2009).

Normally, all data collected by the sensors are sent back to a sink node which challenges the link data rate and the power of low-cost sensor network. According to the characteristic of structure response, technologies to reduce the data quantum are proposed. On one hand, data compression is an available method since the sensing data of structure response is sparse which is able to be compressed with little information loss (Kimura and Latifi 2005; Marcelloni and Vecchio 2008; You-Chiun, Yao-Yu et al. 2009; Casciati, Faravelli et al. 2012). On the other hand, on-line calculation can relieve this problem since only abnormal information is interested in SHM which suggests embedding health diagnosis algorithms into the local sensors to extract useful information (Lynch 2002; Wang 2007; Nagayama, Spencer et al. 2009). For example, the spatiotemporal correlations among the sensors' measurements are exploited via adaptive filters executed at both the sensor node and sink node to predicate the next measurement which decides what data needed to be sent back to the sink node: the preceding measurement will be sent back only when the predict error is larger than a predefined threshold, otherwise it is just exchanged among neighbor nodes. (Ampeliotis, Bogdanovi'c et al. 2012).

To facilitate embedding on-line calculation algorithms into a wireless sensor, embedded operating systems, such as Tiny Micro-threading Operating System (TinyOS) (Hill 2003) or Linux, are required. TinyOS enables users focusing on the application of the sensor system without being bothered by transmission issues (Pakzad, Fenves et al. 2008). To comply with the limited resource of WSN, algorithms should be optimized to reduce the computational burdens and communicational burdens, therefore distributed calculation and substructure approach are proposed. (Lynch 2002; Johnson, Brown et al. 2004; Gao, Spencer et al. 2006; Nagayama, Spencer et al. 2009; Lei, Liu et al. 2011).

In recent years, more and more processors were made available to the low-power and low-cost WSN application potential while providing high performance compare to the popular 8-bit microcontroller: examples are the 32-bit micro controller ARM (Nagayama, Spencer et al. 2009) or the digital signal processor (DSP) (Gong 2011). Power-harvesting techniques are also proposed to acquire energy from solar energy, vibration energy or thermal energy to extend the life-time of each wireless sensor. In addition, a better way

to balance the power consumption of different sensors is investigated in order to extend the life time of the whole wireless sensor network as well as the robustness of the wireless communication (Gong 2011).

Effort is also made by the author's team of University of Pavia toward the realization of a wireless unit which provides flexible interfaces and efficient power management in order to make it to be compatible with various existing sensors which work in different voltages and possess different output sensibilities (Casciati, Faravelli et al. 2010; Chen 2011; Casciati, Faravelli et al. 2012; Casciati, Faravelli et al. 2012).

These developments ensure the wireless sensors can be utilized as a good cable-replaced data transmitting tool.

1.2.2 Positioning sensors

Traditional displacements measurement methodologies, such as LVDT, require a reference point, creating significant challenges to the field application of large scale structure. Acceleration measurements, which do not require a reference point on the structure, are traditionally used to determine the dynamic characteristics of structures. The displacement is then obtained through double integration of acceleration data, but the result may not be stable due to a bias in low-frequency contents. The most common method to avoid the bias involves filtering the low-frequency content from the data in order to reduce the effects of (usually) unimportant low-frequency components. However, this operation has to be done with care so as not to filter out significant low frequency components which become more important as the structure becomes larger and more dispersed. Therefore, non-contact displacement measurement sensors are more and more preferable.

GPS positioning sensor is one of this kind of sensors: indeed, it is adopted in the structural monitoring of very flexible structures, such as suspended bridges or tall buildings, and offers a mm-level accuracy which is sufficient for accurate deformation measurements in the structural monitoring (Casciati and Fuggini 2008; Casciati and Fuggini 2009; Fuggini 2010; Casciati and Fuggini 2011). To reduce the cost, the potential of using off-the-shelf low cost GPS receivers into SHM were also investigated (Ramin and Helmi 2009; Jo, Sim et al. 2011) but the accuracy of low-cost GPS is still to be improved.

GPS is only effective in open area, and therefore it requires a visible sky position to place its antenna, but a roofed position to place its processor and the power supply. At times, it is difficult to route cables due to the building structure constraint. Therefore, a wireless data logger can greatly facilitate the setup and use of GPS receivers. Indeed, there are several products of wireless GPS data logger (Solomon, Wagealla et al. 2002; CES 2012; Houlux 2013; Kreatit Design 2013; Sysbyte Telecom INC. 2013). But these products focus on providing data logger for the vehicle tracking and therefore low-accuracy GPS receiver is built-in. In addition, either GPRS or WIFI is adopted in those ready-made data logger and this means high power consumption.

Another deficiency of high-accuracy GPS is that the system is only effective in open area with a satisfactory number of the available satellites and a suitable geometric distribution. Therefore, continuous monitoring with equal precision in all position components at any time is a challenge for GPS sensor. Hence, various methods were proposed to enable robust indoor positioning.

First, inertial systems, which include all the techniques that take advantage of the inertial properties of any movement, were proposed to improve the robustness of a GPS system. This system can bridge GNSS outages as well as provide accurate short-term data with very high rate to interpolate GPS trajectory while GPS provide bound data for inertial sensors. Few coupled integrations are employed to share information between the GPS and INS system (Hide, Moore et al. 2004; Casciati and Wu 2011a). Currently, Trimble provides a serial of GNSS-Inertial system which provides centimeter level mobile positioning accuracy (Trimble Navigation Limited 2012). For structural Health monitoring, this accuracy cannot be regarded as sufficient.

Secondly, another way to provide indoor positioning measurement could be the pseudolite LPS whose main idea is to deploy pseudolites around the measuring sensor unit to assure the sensor can measure its distances to each pseudolite at any time through which the sensor position then is obtained, as shown in Figure 1.1. The distance is obtained by multiplying the signal propagation time by speed of the electromagnetic wave. Providing the sensor is synchronized with pseudolites, several technologies can help assessing the propagation time more accurately: Chirp Spread Spectrum (CSS), Ultra Wide Band (UWB), Frequency Modulation Continuous Wave (FMCW), Carrier phase shift measurement. CSS and UWB are adopted by 802.15.4a standard and offer accuracies of meterlevel

and decimeter-level, respectively (DecaWave 2012; Nanotron 2012; The Institute of Electrical and Electronics Engineers 2012). FMCW and carrier phase shift are utilized in laser radar-based LPS (Mohammad Nejad and Olyae 2006) which provide accuracy of the centimeter level (Ellinger, Eickhoff et al. 2007) and of the millimeter level or even better (Du Plessis 2008), respectively. For example, IBIS-S is an interferometric radar displacement sensor which can provide with an accuracy between 1/100 and 1/10 of a millimeter through comparing the phase difference between the transmitted signal and the received signal (Gentile 2009; De Pasquale, Bernardini et al. 2010). Specially, this radar sensor achieves a spatial resolution dense to 0.5meters via a technology called step frequency continuous wave (SF-CW) (Gentile 2010). Carrier phase shift is also used in dual-frequency high performance GPS which provide positioning accuracy of mm-levels (Casciati and Fuggini 2008; Casciati and Fuggini 2009; Fuggini 2010; Casciati and Fuggini 2011) and it is also employed in the pseudolite based LPSs which provide cm-level accuracy (Locata 2012).

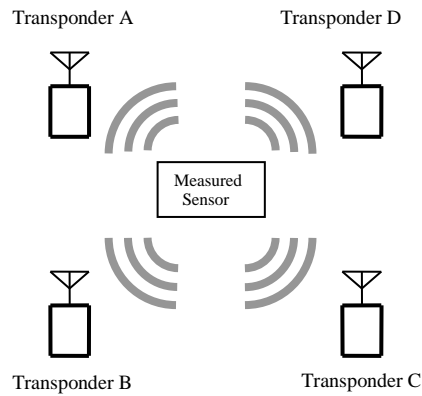


Figure1.1 Local Positioning System (LPS)

As one of the few successful pseudolite LPS systems, Locata creates terrestrial networks that serve as a “local ground-based replica” of the GPS-style positioning. The Locata system includes three or more transceivers, called LocataLites, which provide signals that enable highly accurate range measurements, and some standalone receivers, called Rovers, which track LocataLite signals and calculate latitude, longitude and elevation. This system works on the free-license 2.4G radio frequency. Different from GPS satellites which uses high-cost atomic clock to keep the accurate time, the Locatalite

employs a low-cost temperature-compensated crystal oscillator (TCXO) clock (Barnes and Van Cranenbroeck 2006). The main difficulties of this system are how to synchronize all of the base stations accurately and how to mitigate the multipath error which is dominant in the positioning accuracy (Jardak and Samama 2010). A Direct digital synthesis (DDS) technology is used in the time-synchronization procedure within the LocataNet, known as Time-Loc (Barnes, Rizos et al. 2003; David 2009). Currently, TimeLoc synchronizes Locata transmitters and receivers to an accuracy of 1nanosecond, which is a level substantially more accurate than that which can be attained using the multiple atomic clocks on board GPS satellites (Locata 2012). Locata utilizes an antenna array, called TimeTenna, to mitigate the multipath signal under indoor environment (Rizos and Li 2011). The resulting position standard deviation of outdoor test of this system was approximately 2mm and there were no long term drifts (Barnes and Rizos 2007). For most points measured under indoor static test, the mean error is less than 2cm while during the dynamic test, the error is no more than 3cm after the algorithm has converged (Rizos, Roberts et al. 2011).

A further proposed cheap solution to indoor pseudolite LPS is to import satellite signals in a satellite un-visible area through repeater (Vervisch-Picois and Samama 2009), which consists of an amplifier with two kinds of antenna: one, external, has full visibility of the satellites; the other kind of antenna irradiates the amplified signal toward the measurement environment (see Figure 1.2). Four irradiating antennas are generally required. Different latency steps are introduced in different irradiating antennas in order to avoid signal conflicting since the signals are reproduced by the same external signal. If the latency step is big enough for the wished cover range, the signals from different irradiating antennas become uncorrelated inside the covered range and can be simultaneously demodulated by the receiver, namely, received simultaneously. Theoretically, using a minimum of four antennas appended in different positions, the repeater can reproduce the situation of an open sky measurement node even with just a single visible satellite (provided the signal from it is good enough). So far, there is not off-the-shelf latency device which can provide precise time-delay for such a pseudolite LPS.

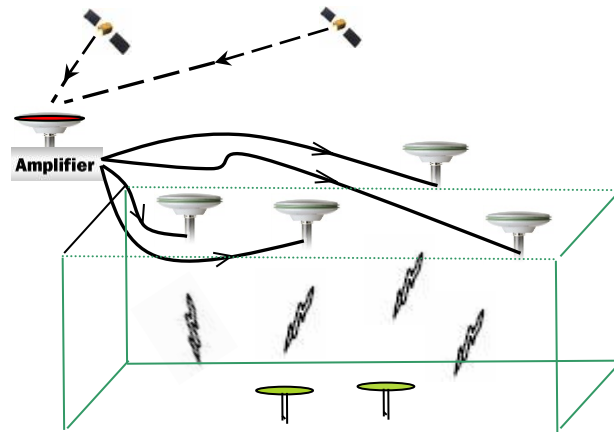


Figure 1.2 Schematic representation of the adoption of repeaters toward LPS

But the positioning accuracy of these two pseudolite methodologies is yet to be improved in view of SHM.

As a third option, laser-based LPS is a good alternative for indoor displacement measurements since the laser possesses a monochromatic character. The emitted laser light possesses high degree of spatial coherence which assures narrow output beam with limited diffraction. Therefore, there is not multipath error and large distance can be reached since the power is concentrated. These special features let laser distance measurement sensors to be universally applied. There are a variety of techniques utilized for laser distance measurement (Du Plessis 2008; Krüger, Bahr et al. 2010): time-of-flight (TOF), triangulation, phase-shift, frequency modulated continuous wave (FMCW) and displacement measuring interferometry (DMI). In the TOF distance measurement, a short laser pulse is projected to a target. The time the pulse takes to travel forward and backward is measured. The distance to the target is calculated from the TOF and the speed of the light in the medium. Driven by the progress in sensor technology, computer methods and data processing capabilities, 3D laser scanning, such as Terrestrial Laser Scanner (TLS), has found its application in monitoring the static and dynamic behavior of large infrastructures and provide high accuracy (González-Aguilera, Gómez-Lahoz et al. 2008). Laser positioning system could provide displacement measurement accuracy as high as from pm to nm when using DMI technology, such as the modular vibrometer system OFV-5000 from Polytec for example, but the maximum full scale displacement measurement range is relatively small: $\pm 82\text{mm}$ even though the working

distance is configurable up to 10m(Polytec 2012). However, these devices are expensive.

1.2.3 Vision-based LPS

Another candidate of LPS, vision-based LPS, is discussed. Velocity and displacement measurements using images are based upon tracking the object motion between sequences of images. This system, although it requires a “sight-on-line scene”, enables accurate dense measurements of both dynamic processes and, especially, static deformations which are more attractive. Consider damage detection for instance: data for damage detection can be either dynamic, (i.e., vibration-based properties) or static deformation profiles. It is usually more convenient to obtain dynamic types of data because they contain more information regarding a given structure (Kohut and Kurowski 2006; Kohut and Kurowski 2009). Unfortunately, to obtain the high frequencies which characterize the high-order vibration mode shapes, to collect dynamic data requires devices which are expensive to set up, maintain and automate, but mainly it can be very difficult (or even impossible) to excite a large structure to vibrate at those frequencies. The static deformation profile requires much less effort, and therefore using the static deflection for damage detection is sometimes more attractive (Uhl, Kohut et al. 2011).

Vision-based displacement measurement systems have been installed on large scale structures: six video cameras have been installed on the health monitoring system of the cable-stayed bridge in Shenzhen Western Corridor (CSB-SWC), eighteen video cameras have been installed on the SHM system of the Stonecutter Bridge (Ni, Wong et al. 2011), and three video cameras have been installed on the SHM system of GuangZhou TV Tower (Liao 2012). In the last system, the space coordinates of the object are reconstructed simply through multiplying the image coordinates by a scale factor (Ni, Liao et al. 2013) which does not take the projective distortion and camera distortion into consideration and therefore errors are introduced. More precise camera calibration methodologies are required.

A tailor-made two-channel camera system is utilized to monitor the two-dimension motion of a bridge in the work of Olaszek (Olaszek 1999). The errors in this vision-based measurement system were discussed. But the camera calibration is still based on simple scale factor calculations. Similarly, in the

work of Lee, the scale factor camera calibration is adopted. The scale factor is calculated through two pairs of known-distance white spots which are perpendicular each to the other (Lee and Shinozuka 2006). On the work of Uhl, a vision-based measuring apparatus is used to measure the in-planer deformation of a steel frame loaded by a point force in a laboratory experiment. They utilize a circular intensity pattern, with a known diameter to calibrate the camera which allows calibration in any direction. In their publication, a full camera calibration is also referred (Uhl, Kohut et al. 2011). The authors also apply the camera system onto 3D experiment to monitor a steel frame which is forced to vibrate by sinusoid signals (Uhl, Kohut et al. 2009).

In the laboratory experiment carried out by Jurjo (Jurjo 2010; Jurjo, Magluta et al. 2010), a vision system ,which includes a camera and an associated image processing program, is used to study the 2D non-linear dynamic behavior of a clamped-free slender metallic column subject to its own weight and large displacements and rotations under both tension and compression. Direct linear transformation (DLT) is utilized to calibrate the camera. The calibration is performed following an interpolation way which means to put the reference markers in a region around the structure thus ensuring that any configuration of the structure will always be within the calibration region, and therefore, provides precise results when compared to those obtained by following an extrapolation way. The experiment results corroborate the precision of this system and this system represents an advance in the monitoring of structures that cannot be instrumented through conventional sensors, as is the case of some reduced-scale models in which the responses would be affected by the introduction of sensors. Based on the computer vision and epipolar geometry theory(Hartley and Zisserman 2004), the camera model is built and is utilized to reconstruct the three dimension space coordinates of object (Jahanshahi, Masri et al. 2011; Jahanshahi and Masri 2012). A vision system was also proposed to monitor the 3D crack in real structures (Iyer and Sinha 2005).

Basically, the aforementioned systems are constructed based on a self-developed program which requires a well-understand of both the program language (such as Visual C++) and the digital image processing methodologies, and those requirements limit the utilization of vision-based displacement system.

1.3 Content and organization of this thesis

This work studies available solutions for non-contact displacement sensors in view of structure monitoring applications. It starts from the well-known Global Positioning System (GPS). Although GPS is not a strictly non-contact sensor, since the receiver must be mounted on the structure, it possesses the same merits of non-contact displacement sensors while it is used in field experiment: it does not require reference fix points near the monitored points and provides directly high accuracy displacement measurements.

A significant limitation in the GPS applications is the spatial distribution of the receiver. The connection between the receiver and the control display unit available on the market is of the wired type which causes inconveniences when this system is used for monitoring the roof of a building or the cables of a suspension bridge. Indeed, the final control display unit in such a long-term monitoring GPS system is a computer which is not conveniently located near-by the antenna, thus resulting in cables of the length of 80- 100 m. Therefore, wireless connection is considered to be employed to replace this wire connection as well as the power support cable. In this work, a low-power-consumption wireless cable replacement is implemented to transmit data back to the center in real time for GPS receiver whose sample rate is up to 20Hz. Two wireless links, which are based on the 24XStream and the CC1110 transmission systems, are applied to replace the cable transmission between the dual-frequency high precision GPS receiver and the user client computer which up to now was the only market offer. Experiment results show a successful cable replacement.

Since GPS is only effective on an open area scene, non-contact Local Positioning Systems (LPS) are studied as potential solutions for indoor situations. In this work, a low-cost TOF-based laser sensor, YT89MGV80 is utilized. The static and dynamic performances of the laser sensor are studied with the help of a wireless DAQ system which was developed at the University of Pavia (Casciati, Faravelli et al. 2010; Chen 2011; Casciati, Faravelli et al. 2012; Casciati, Faravelli et al. 2012). While the amplitude of the measured signal is smaller than 1mm or when the frequency of monitored motion increases, the noise cannot be ignored. This noise is introduced by both the laser sensor and the wireless sensor. Hence, on one hand, the design of the wireless DAQ system is improved to eliminate the system noise. On the other hand,

several methodologies, including temperature compensation, average moving filtering, Gaussian filtering, and spectral subtraction are adopted to improve its accuracy. Experiment results confirm the effective of those methodologies.

A further candidate for LPS is based on vision techniques, which enable dense measurements of static deformations, as well as dynamic processes, with low-cost apparatus. They are currently made available by ongoing technology developments in more and more sophisticated formats. In this work, the 2D camera model is first derived. Based on this model, the camera calibration methodology, image registration and direct linear transformation (DLT), as well as the space coordinates' reconstruction methodology will be introduced. At last, a vision-based displacement system is constructed and is used to monitor the motion of a frame in laboratory experiments. Instead of a self-developed software, those vision systems make use of commercial software to simplify the process of constructing a first-step vision-based displacement measurement system. That allows one to build its own system without going deep into the image processing methodologies and sophisticate programming languages. Two vision systems, which cover a medium range investigation area, are implemented in this work to monitor the vibration of two reduced-scale frames available in the laboratory. Several markers are placed on the positions of interest. An image processing procedure is used to acquire the 2D displacements of the markers.

The thesis is organized as follows: In chapter 2, two wireless networks are employed to realize the wireless links for the GPS system: the potential and the implementation are illustrated. Experiment results corroborate the success of the cable replacement. Chapter 3 investigates the first LPS displacement sensors. The performance of an available laser distance measurement sensor is discussed with the assist of a wireless DAQ system. Two means are proposed to reduce the noise observed during the experiment: multiple reading with the help of signal processing and an improvement of the design of the wireless DAQ system. Experiment results confirm the effective of those two means. In chapter 4, the other LPS displacement sensor approach, the vision-based LPS is studied, designed and implemented. Camera model and camera calibrations methodologies are detailed in this section. The performance of the system is discussed on the basis of the laboratory experiments. Conclusions and future works are discussed in the last chapter.

Chapter 2 Wireless Global Positioning System

2.1 Introduction

In the Global Positioning System (GPS), there are 32 satellites all around the Earth which periodically broadcast their position information. A GPS receiver measures its distances from at least four satellites based on the corresponding signal propagation time and the light speed. These four distances can also be expressed according to the coordinates of the GPS receiver and of the four satellites. Thus, four equations can be constructed. The unknowns in these equations are the position coordinates of the receiver (x, y, z) and the clock offset between the single GPS receiver and the GPS system. These four unknown quantities can be obtained by solving the above four equations.

The GPS positioning system can work all the day providing that its antenna has an open view to the sky. Therefore, its use is particularly suitable in the long-term monitoring of the motions of high-rise buildings or the long-span bridges (Kijewski-Correa, Kareem et al. 2006; Casciati and Fuggini 2009; Wong and Ni 2009; Ni, Wong et al. 2011). Generally, the GPS antenna and the GPS receiver are mounted on a high position which is not sheltered to receive good quality signal, and the obtained positioning recorded is transmitted to a control display center to be further processed, displayed and archived. That control display center is normally a computer and must be located in a sheltered room. Currently, wires are universally adopted to connect the receiver and the control display room which significant limits the spatial distribution of the receiver. Therefore, in this section, the possibility of a wireless wire-replacement solution for long-term monitoring GPS receivers, such as the Leica GMX 902 and the Leica GRX 1200-pro, is discussed

The GPS receiver system generally consists of six components: an antenna, a receiver, a processor, an input/output (I/O) interface connecting the last two with a control unit (a PC) and a power supply (as shown in Figure 2.1). It is worth noting that usually the receiver and the processor are integrated in a single block: thus one only sees five components. The radio-frequencies (RF) satellite signal is received via the antenna, which is mounted on the monitored object, and then in the receiver, it is down converted into intermediate

frequency (IF) before it is sampled as a digital signal which is correlated with an internally generated replica of the satellite code in order to acquire, track and demodulate the GPS signals. The correlation result is delivered to the processor which extracts the GPS raw data, (such as pseudo-range, integrated carrier phase, Doppler shift, satellite ephemeris), and controls the software signal tracking loops. The raw data is then sent via a cable to the control display center for being further processed by positioning algorithms to obtain position and velocity of the receiver which are eventually displayed.

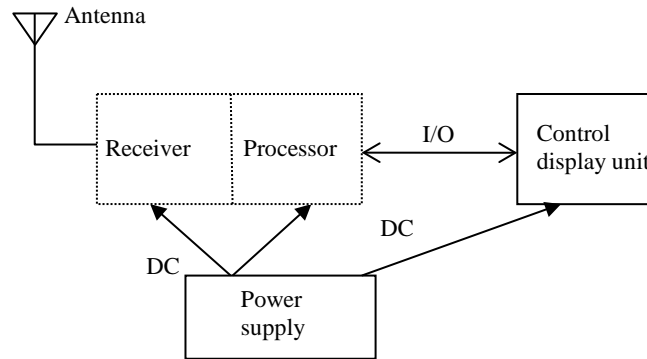


Figure 2.1 Scheme of a GPS receiver

Presently, the connection between the receiver and the control display unit available on the market is of the wired type. However, wireless-replacement is feasible since the signal communicated between the receiver and the control display unit is in digital form. In addition, the power support cable could be another inconvenience: it is likely that nearby one of the receivers there is a connection to the power network, but it is also true that several receivers must be displayed and again several meters of electrical cables must be left in an aggressive environment. The power supply cable could be replaced by a battery in order to increase the flexibility of the system and the battery must be coupled with a power harvesting device able to recharge it (Casciati, Faravelli et al. 2012).

Indeed, today, there are several products of wireless GPS data logger (Solomon, Wagealla et al. 2002; CES 2012; Houlux 2013; Kreatit Design 2013; Sysbyte Telecom INC. 2013). But these products focus on providing data logger for the vehicle tracking and therefore low-accuracy GPS receiver is built-in. In addition,

either GPRS or WIFI is adopted in those ready-made data logger which means high power consumption. In our case, not only the communication cable, but also the removal of the power supply cable is pursued. Therefore, in this work, a low-power-consumption wireless cable replacement is implemented to transmit the data back to the center in real time for a GPS receiver. Long-term monitoring GPS receivers, such as the Leica GMX 902 and the Leica GRX 1200-pro, are selected to test the performance of the proposed wireless links. Since the GRX 1200-pro supports to work by battery power supply, in this case, power supply only reaches the computer by a wired link and the other modules rely on batteries re-charged by power harvesting devices.

Two wireless transceivers, the 24XStream, which provides a baud rate of universal asynchronous receiver and transmitter (UART) at 9600 bit per second (MaxStream 2006), and the CC1110, which supports a baud rate of UART at 115200 bit per second, are then described. The power consumption of the system is also analyzed. Some experiments based on the coupling of the GMX902 with the transceiver 24XStream are first executed to check the feasibility of replacing the wired communication cable between the GPS receiver and the computer by a wireless link. Due to some unsatisfactory outcomes, some experiments based on the GRX 1200-pro coupled with the transceiver CC1110 are finally executed to check the performance of this second wireless solution.

2.2 Leica GPS receiver system

This section deals with the application of wireless transmission technology to long-term monitoring GPS receivers — like the Leica GMX 902 and the Leica GRX 1200-pro. As shown in Figure 2.2, the Leica GPS receiver system includes: a compact geodetic antenna (AX 1202), a receiver (GMX 902 or GRX 1200-pro), a computer and software (GPS or GNSS Spider and GNSS QC V2.0: GNSS means Global Navigation Satellite System).

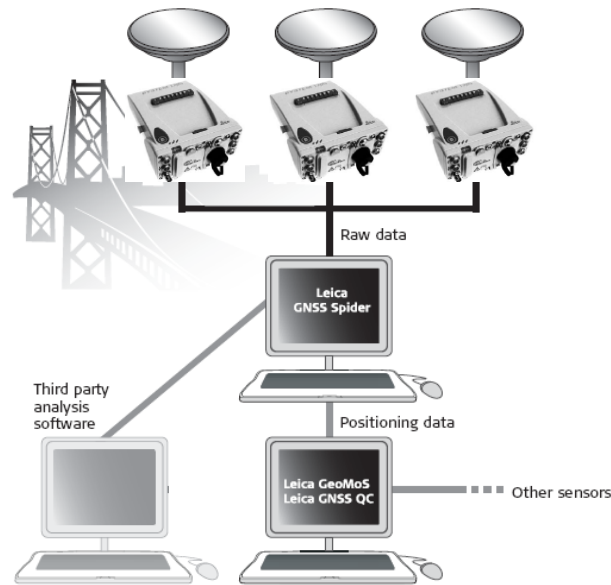


Figure2.2 The GPS receiver system for GRX 1200 (elaborated form (Leica Geosystems AG 2010)).

The antenna is mounted on the object to be monitored and is connected with the receiver by a coaxial-cable through which the radio frequency signals are transmitted. The receiver unit acquires, tracks and demodulates the satellite signals and provides, through an interface, the resulting GPS raw data to the user client computer for being further processed by suitable software. As said, the receivers can be put in the roof of buildings, on the top of bridges or along suspended cables. Thus it is evident that to have physical links between the receiver and the computer is undesirable. Therefore, the interface is conveniently made wireless in this case.

2.2.1 The interface between receiver and computer

The Leica GRX1200-pro is a high-performance GNSS receiver, specially developed to monitor sensitive structures. It provides precise GPS dual frequency raw data (12 L1 + 12 L2 GPS, from 0.17 Hz up to 20 Hz), enabling precise data capture of fast moving objects. The data are logged into the Leica binary (LB2) raw data format and could be sent back to the computer via a

RS232 compatible interface by which the receiver also receives control commands from the computer. A compact flash card up to 8 GB is used to log data in the receiver.

Table 2.1 lists the parameters of the GRX 1200-pro receiver (Leica Geosystems AG 2008). In the available device, the compact flash card is 32 M Bytes, which is sufficient for around 41 recording hours at the logging rate of 1s (according to Table 2.1). The data rate could be calculated as 2071bps when the data logging rate is 1s (the data rate will be 40kbps when the logging rate is 0.02s).

Table 2. 1 Features of the GRX 1200-pro receiver.

No. of channels	12 L1 + 12 L2
Code and Phase Measurement Precision (irrespective whether AS off/on)	Carrier phase on L1 / L2 0.2mm rms / 0.2mm rms Code (pseudorange) on L1 / L2 2cm rms / 2cm rms
Accuracy (rms) with post processing	Static (phase), choke ring antenna, long lines, long observation time : Horizontal: 3mm + 0.5ppm, Vertical: 6mm + 0.5ppm
Position update rate Selectable	0.05 sec (20Hz) to 60 secs (0.17Hz)
Data capacity (1 GB)	1152h GPS L1 + L2 data logging at 1s rate 17600h GPS L1+L2 data logging at 15s rate

Note: if the standard deviation of the positioning result is a mm+b ppm (ppm: parts per million), the distance from the rover to the reference station is D (km). Then, the positioning accuracy is:

$$\sigma_D = \pm \sqrt{a^2 + b^2 \times D^2}, \text{ unit: mm}$$

The GMX 902 GG receiver, which is also produced by the Leica company, possesses similar features as the GRX 1200-pro. But in addition to GPS signals, it can also receive the signal from GLONASS. GMX 902 GG provides precise GPS/GLONASS dual frequency raw data (14 L1 + 14 L2 GPS, 12 L1 + 12 L2 GLONASS, up to 20 Hz), and there is not the battery power supply option.

2.2.2 The power consumption of GRX 1200

To make the receiver able to work without power cable, its power consumption is discussed and self-power-supply solutions are proposed.

The power consumption of GRX 1200 and its antenna AX 1202 are shown in Table 2.2. Inside the GRX1200, there is an interface for the battery: GEB171, which is a rechargeable 8000mAh/12V NiCd battery (8000mAh/12 V means the battery could work 1 hour if it works in the nominal voltage (12V) and the discharge current is 8000mA). Therefore, the receiver could work around 25 hours with the battery (Leica Geosystems AG 2007). The work time of the battery must therefore be extended by adopting an energy harvesting module able to recharge the battery. Normally, the receiver is installed on open sky location in order to capture signals from enough satellites which ensure taking advantage of solar energy or wind energy. In some cases, e.g. the cable-suspended bridges, the vibration energy of the monitored structure could also be collected to recharge the battery (Casciati and Rossi 2007; Casciati, Faravelli et al. 2012).

Table 2.2 The power consumption of the GRX 1200 pro receiver system.

	GRX 1200+ GNSS	AX 1202	Total
Voltage	12V	4.5-18V DC	--
Current	Non specified	50mA maximum	--
Power	3.6-4 W	0.25- 1W	3.85- 5W

2.2.3 Server and software

The computer acts as a server on which two software tools (Leica GNSS Spider and GNSS QC V 2.0) are installed.

Leica GNSS Spider manages single and multiple receivers and provides file products service (automatic data management, data compression, quality control and FTP service) for standard continuously operating reference station (CORS) applications. It supports data in the formats of RAW, RINEX and Compact RINEX. GNSS Spider provides continuously streamed raw data archiving or downloading data logged files from the receiver. The validation of the raw data, for quality and completeness, is performed automatically (see Figure 2.3). This software also offers positioning services both in real-time or post-processing. Through GNSS Spider, one can also read the details of the signal such as which

or how many satellites are tracked and their navigation information. The achieved data are also accessible in the computer.

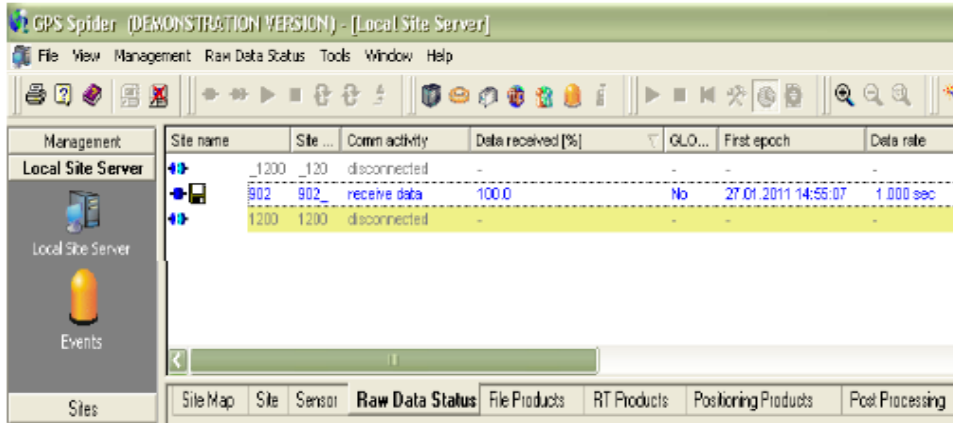


Figure2. 3 The local site server interface of the software GPS Spider.

Another software tool, GNSS QC V2.0, performs an assessment of the quality of both the tracked satellites signals and the positioning results (Leica Geosystems AG 2010).

2.3 Wireless GPS data logger

The goal of this section is to illustrate how one moves from Figure 2.1 to Figure 2.4. Two wireless transceivers, 24XStream and CC1110, are employed toward this cable replacement.

First, a wireless data logger is implemented using the transceiver 24XStream to communicate between the Leica GMX 902 and the computer for performing a feasibility study. The specifications of 24XStream are illustrated in Table 2.3. It supports a 9600 bps data rate within 180 meters. A variety of network topologies could be realized based on the 24XStream: peer-to-peer, point-to-multipoint, and point-to-point. At the meantime, it offers the Hopping Channel Command by which different sub-networks could have different hopping channel numbers and they can communicate in parallel. In addition, the 24XStream could be configured as a repeater through which the signal received will be passed and the communication range is increased. In this way,

all these features enable the 24XStream as adequate to be adopted for building a flexible network.

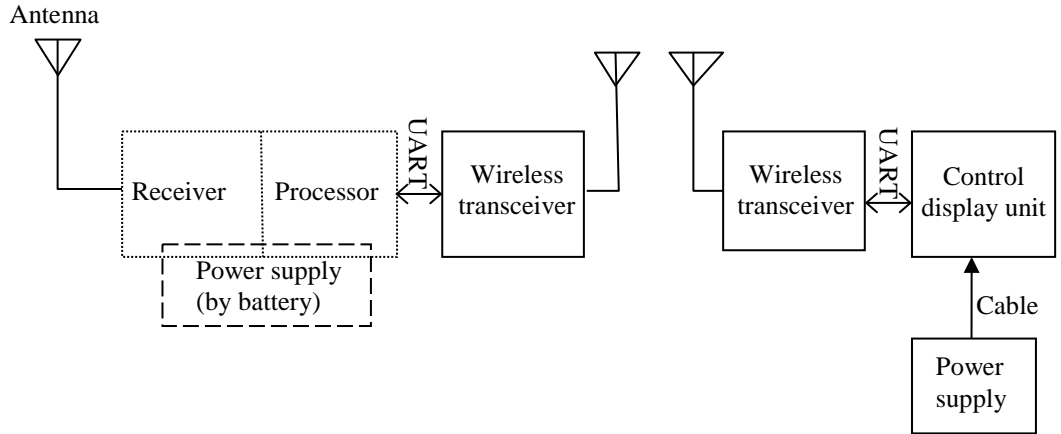


Figure2. 4 The objective of the wireless connection for the GPS system.

Table 2. 3 Properties of the 24XStream RF Module (with 9600 bps throughput data rate)

Urban communication Range	Up to 180 m for single hop
Supply Voltage	5V DC
Receive/Transmit/Power Down Current	80 mA/ 150 mA/ < 26 uA
Frequency Range	2.4000 – 2.4835 GHz
Spread Spectrum	Frequency Hopping, Wide band FM modulator
Network Topology	Peer-to-Peer, Point-to-Multipoint, Point-to-Point
Channel Capacity	7 hop sequences share 25 frequencies
Serial Data Interface	CMOS UART

The 24XStream RF Module is designed as an easy-to-use wireless solution that yields reliable, long range and low cost wireless links. It communicates with its controller via the Universal Asynchronous Receiver/Transmitter (UART) interface (Figure 2.5). It is worth to noting that, one protocol conversion Integrate Circuit (IC), MAC3161, is employed to enable the communication between the 24XStream and the computer since the signal from the 24Xstream

side is at a complementary-metal oxide-semiconductor (CMOS) compatible voltage (in which logic “1” is at -3V, logic “0” is at 3V) and the signal from computer side is at a recommended- standard (RS) 232 compatible voltage (in which logic “1” is at -15V, logic “0” is at 15V).

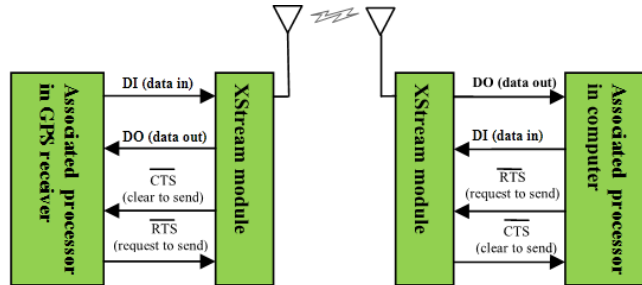


Figure2. 5 24XStream wireless links.

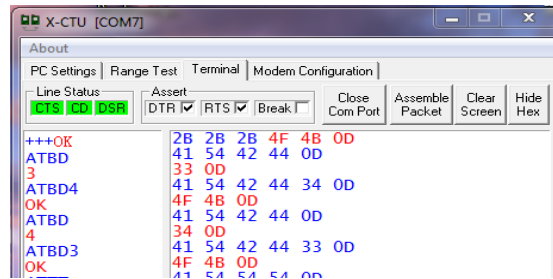


Figure2. 6 X-CTU display window.

The parameters of the 24XStream, such as the baud rate of RS 232 or the address of the wireless module, can be configured through the software tool X-CTU by AT commands (Figure 2.6) (Digi International 2008).

After being powered on, the 24XStream initializes itself and enters the normal operation processes: idle, receive, transmit, sleep or command. That module works in simplex mode which means it can only be in one mode at any moment, i.e. it can either receive or transmit at one time. When 24XStream is applied to replace the RS232 connection, this simplex mode may prevent the system from working correctly if the channel is occupied by one direction, such as by the transmitting from GPS receiver to the computer: In that case, the command from computer to the receiver would never find its chance to be transmitted. To address this problem, 24XStream introduces a streaming limit configuration (so

called TT Command) for limiting the maximum number of bytes that can be sent by the module in one transmission event. This avoids the indefinite occupation of the channel and therefore in this way one simulates the duplex mode of RS232.

Another noteworthy point is that the baud rate of the interface between the GPS receiver and the connected wireless module should be lower than the data rate of the wireless link (Casciati and Wu 2011b). If the data which arrive at the wireless module are not able to be transmitted in time, they will be cached in the wireless module's memory. Data loss occurs when the memory is overflow due to the continuously arriving data stream. The wireless data rate of the 24XStream transceiver is 9600 bps, therefore the baud rate of the interface between GPS receiver and wireless module is set to be 4800bps.

2.3.2 CC1110

Another wireless transceiver was developed: it is based on CC1110 and the software was programmed to fulfill the cable-replacement task for the GRX 1200-pro system. The baud rate cannot be set in the GRX 1200-pro, but the transmitting rate of the CC1110 is compatible with the receiver properties. Since the CC1110 wireless module accesses the link by a frequency division multiplexing (FDM) technology (Casciati, Faravelli et al. 2009), different modules can transmit signals using different frequency channels at the same time and the communication of several GPS receivers to the computer is ensured.

The CC1110 is a low-power RF system-on-chip (SoC) with microcontrol unit (MCU), memory and transceiver. It has 32 kB of in-system flash memory and 4 kB of RAM, data rate up to 500 k Baud and transmission power up to +10 dBm (decibel mW). All these components are programmable. The frequency range adopted in the present application is one of the ISM frequency: 433MHz. CC1110 supports the use of DMA (direct memory access) for both receiver and transmitter proceedings which minimizes the requirement of CPU intervention. This spares the CPU from the transmission and the reception processes and enables power saving. The line-of-sight communication range of the CC1110 is around 150m. Figure 2.7 is the block diagram of the wireless GPS system. The signal from the GPS receiver is transmitted to the radio transceiver CC1110 through a UART-RS232 bridge, SP3223, which converts the RS232 signal into

a UART signal and vice versa. On the computer side, there is another transceiver CC1110 connected with the computer by a USB-UART bridge. The main tasks of the CC1110 connected to the GPS receiver are to receive data from the GPS receiver via UART, and to receive commands from or to transmit data back to the CC1110 connected with the computer. Therefore, the flow chart of the embedded program in CC1110 can be illustrated from Figure 2.8-Figure 2.10.

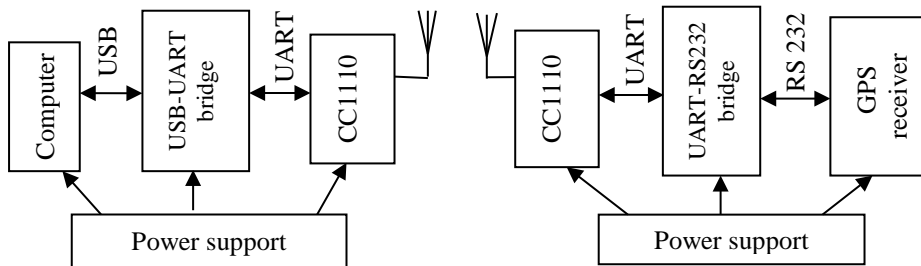


Figure2. 7 The block diagram of the wireless GPS system.

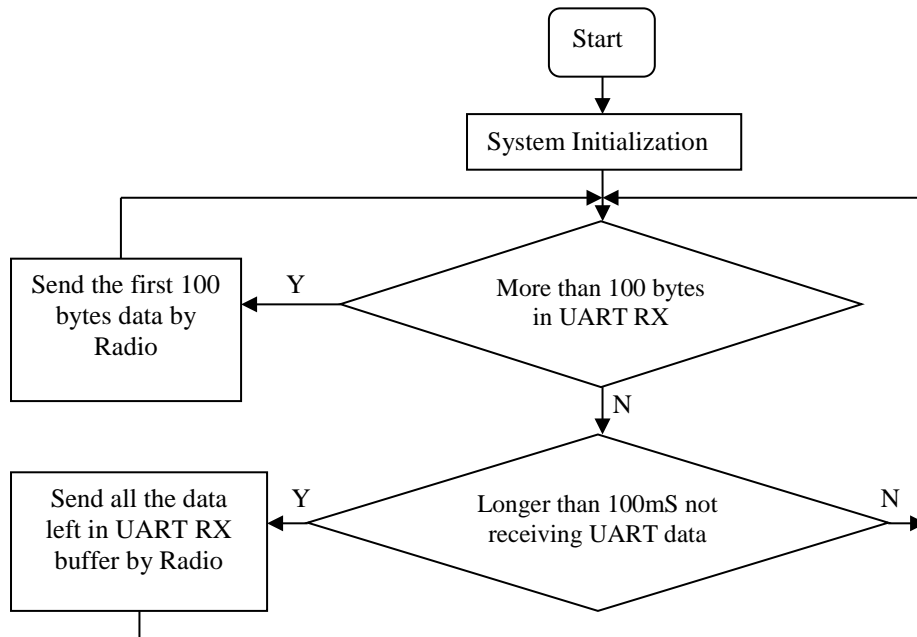


Figure2. 8 Main loop.

Figure 2.8 is the main loop of the program. Figure 2.9(a) illustrates the data reception interrupt service routine (ISR) both in the Radio or UART. Figure 2.9(b) shows the routine of radio send.

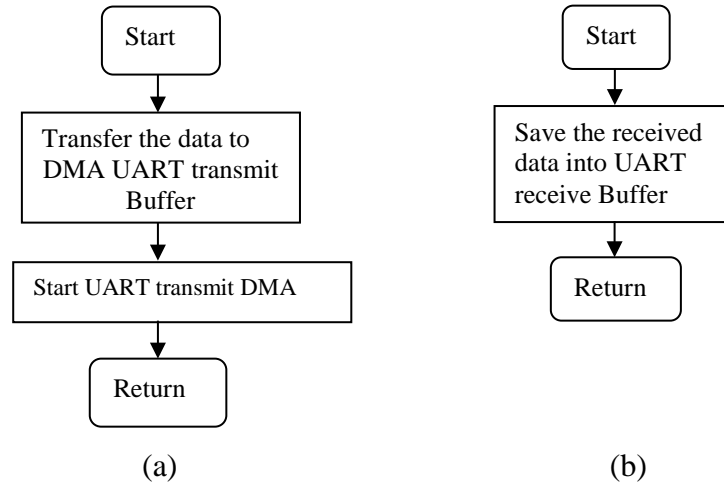


Figure2. 9 (a) Radio reception interrupt service routine (ISR),(b) UART receive ISR.

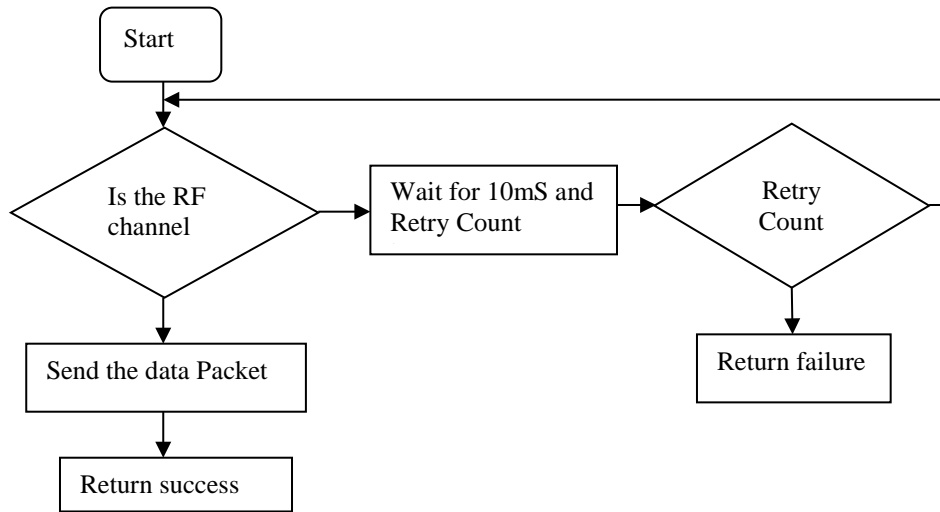


Figure2. 10 Radio send.

2.3.3 Power consumption of CC1110

The power consumption of the wireless transceiver and the UART module are shown in Table 2.4 (Texas Instruments 2007). The capacity of a common AAA size Battery is 1175mAh/ 1.5V, two of which allow the wireless transceiver and interface adapter work for nearly 34.6 hours.

Table 2. 4 Power consumption of the wireless transceiver based on the CC1110

	Voltage	Current	Power consumption
CC1110	3.0 V	20.5(RX)/33.3(TX) mA	61.5/ 100 mW
SP3223	3.0 V	1mA	3mW

2.4 Experiment

To verify the performance and the reliability of these two wireless links (24XStream and CC1110,) for Leica system, several experiments were conducted. It is worth noticing that in this case laboratory experiments are precluded since the GPS receivers must have open sky visibility. The antenna of the GPS receiver is installed on the roof of a three-story building.

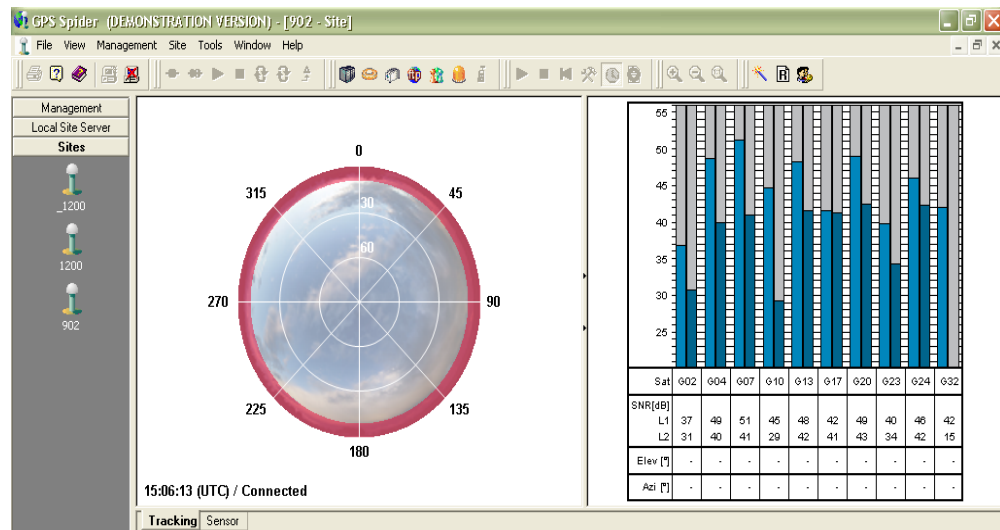


Figure2. 11 The real-time tracking result of the GPS receiver.

In the first experiment, two 24XStream modules are used. One 24XStream is connected with the GPS receiver and the other one is connected with the computer. The baud rate is set to be 9600 bps and the data logged rate in the GPS receiver is 1Hz. The wireless module works without streaming limit. GNSS Spider is configured to manage the data received by the computer: one can also read the data received percent (Figure 2.3), the tracking progress (Figure 2.11) and the real time positioning result (Figure 2.12). Then the completeness of the archived data is examined by the GNSS QC 2.0. Figure 2.13 shows the quality report given by GNSS QC 2.0 which includes the file details, station details and session summary among other items. Since the data reached back to the computer via wireless link passed the quality check, the feasibility of the wireless link is confirmed. But when the logged rate is set to 0.5s, the capacity of serving as a wireless data link of the 24XStream is small and that gives rise to improperly working situations, like the failure of the connection or a high data lose rate. Therefore, another wireless link, based on CC1110, is introduced.

Moreover, the power support cable of the GMX902 could not be removed since it can only work with power support cable (Leica Geosystems AG 2007).

Therefore, another GPS receiver, GRX 1200-pro, which is also produced by Leica and comes with a battery power support, is adopted.

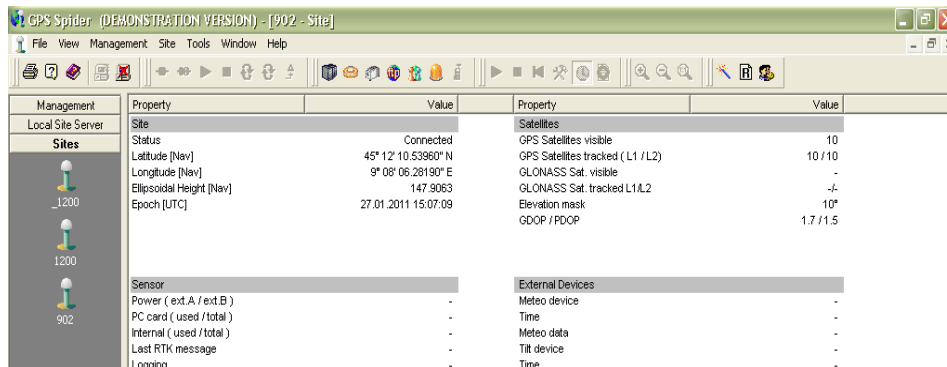


Figure2. 12 The real time tracking and positioning results of the GPS receiver.

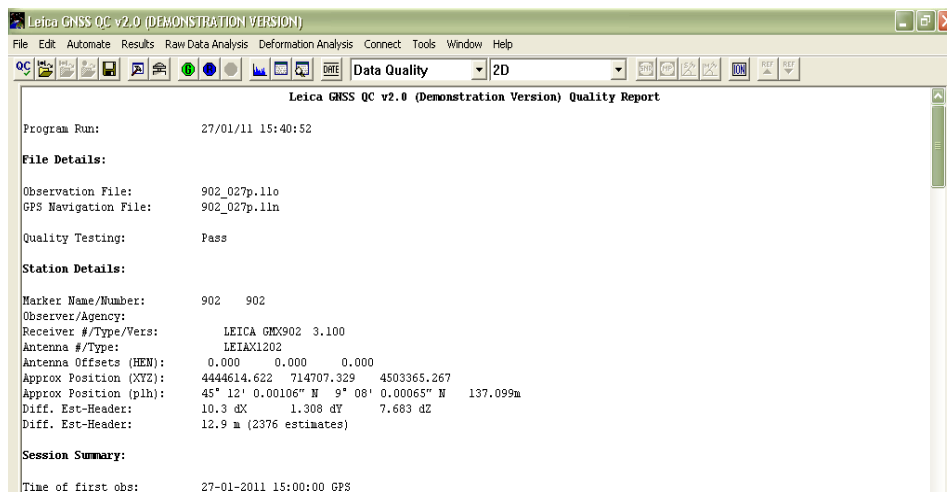


Figure2. 13 The quality check report from GNSS QC V2.0.

Management	Site name	Site ...	Comm activity	Data received [%]	Data rate	Last Gap	Total no. of gaps	Age [sec.]	Avrg. age
Local Sit...	_1200	_120	receive data	97.5	0.200 sec	15.05.2...	1	-154.13	-154.24
	902	902	disconnected	-	-	-	-	-	-
	1200	1200	disconnected	-	-	-	-	-	-

Date/Time	User	Text
15.05.2011 10:37...	Spider Server	Site _1200: Create product sensors1200_bis finalized : C:\GPS Spider\Data_120\2011\05\15_120135k35.rnx.zip -

Figure2. 14 The raw data status of GRX 1200-pro (by GNSS SPIDER software).

Observation File:	_120135k35.11o
GPS Navigation File:	_120135k35.11n
Quality Testing:	Pass
Station Details:	
Marker Name/Number:	_1200 _120
Observer/Agency:	
Receiver #/Type/Vers:	451011 LEICA GRX1200PRO 1.21/2.120
Antenna #/Type:	LEIAX1202
Antenna Offsets (HEM):	0.000 0.000 0.000
Approx Position (XYZ):	4444614.513 714707.013 4503362.911
Approx Position (plh):	45° 12' 0.00105" N 9° 08' 0.00065" N 135.316
Diff. Est-Header:	-0.2 dX -1.767 dY 5.412 dZ
Diff. Est-Header:	5.7 m (1496 estimates)
Session Summary:	
Time of first obs:	15-05-2011 10:35:00 GPS
Time of last obs:	15-05-2011 10:39:60 GPS
Session length:	5.00 minutes
GPS week:	1636, day 0
Num SVs with obs:	9
Num SVs with nav:	12
SVs with obs:	G2 G4 G5 G7 G8 G10 G13 G26 G28
SVs without obs:	G1 G3 G6 G9 G11 G12 G14 G15 G16 G17 G18 G19 G20 G23 G24 G25 G27 G29 G30 G31 G32
SVs with nav:	G2 G4 G5 G7 G8 G10 G13 G16 G20 G23 G26 G28
SVs without nav:	G1 G3 G6 G9 G11 G12 G14 G15 G17 G18 G19 G21 G22 G27 G29 G30 G31 G32
Total GPS orbits:	20
Obs interval:	0.20 seconds

Figure2. 15 The quality check report (by GNSS QC V2.0).

A further experiment in which the logged rate of GPS receiver is 0.2s is carried out for the new wireless link. Please, note that GPS receivers are used today in monitoring structures of relatively high own period and hence a sample rate of 5Hz is enough to monitor the vibration of the structure. Figure 2.14 is the raw data status of the receiver, by which one can see that the wireless UART works properly. Since there is a receive gap at the beginning, the data received rate is 97.5% instead of 100%. Then the archived data is sent to the quality check of GNSS QC V2.0, which shows that the data are satisfactorily transmitted (Figure 2.15). Figure 2.16 shows the real-time tracked satellites.

The results show that this replacement is feasible. Two types of wireless module, the 24XStream and the CC1110 were utilized for the cable replacement. The experiment results showed that the link between the block antenna-receiver and the computer can be successfully replaced by a wireless connection under indoor environment even though the wireless signal is affected by multipath and deep attenuation.

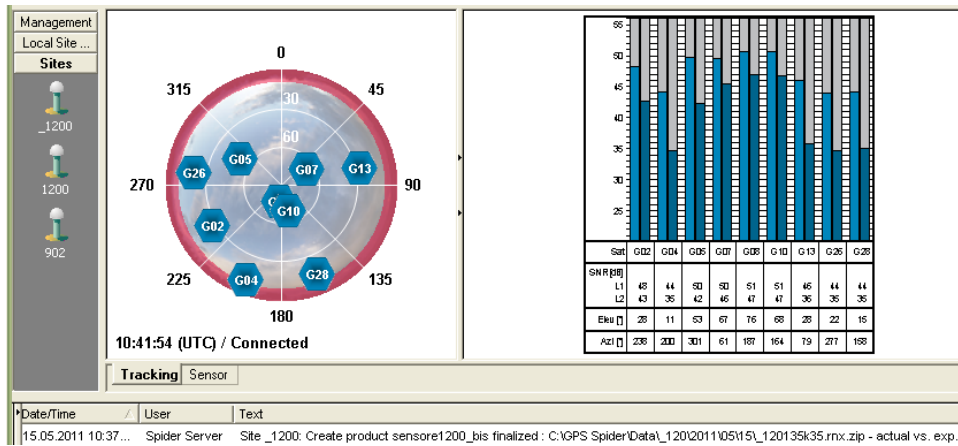


Figure2. 16 The real-time tracked satellites (by GNSS Spider).

Chapter 3 Wireless Laser-based Local Positioning System

3.1 Introduction

In structural monitoring, displacement measurements play an important role since the displacements are explicitly related to the strains and hence to the stress. Laser sensors could be a good alternative for indoor displacement measurement since the laser possesses a monochromatic character (the term "laser" originated as an acronym for Light Amplification by Stimulated Emission of Radiation). The emitted laser light is notable for its high degree of spatial coherence which is typically expressed through the output, being a narrow beam with limited diffraction. Therefore, there is not multipath error in the laser system. In addition, the light can be launched into a beam of very low divergence in order to concentrate the power at a large distance. These special features let laser distance measurement sensors to be universally applied.

There is a variety of techniques utilized for laser distance measurement (Plessis 2008): (1) time-of-flight (TOF); (2) triangulation; (3) phase-shift; (4) frequency modulated continuous wave (FMCW); (5) displacement measuring interferometry (DMI). In the TOF distance measurement, a short laser pulse is projected to a target. The time the pulse takes to travel forward and backward is measured. The distance to the target is calculated from the TOF and the speed of the light in the medium. In the triangulation techniques, the distance to a point, or the coordinates of a point, are found by using the known relationships of angles and sides in a triangle. In the phase-shift measurement, the laser signal is modulated and the phase-shift between transmitted and received signals is measured: it is proportional to the signal travel time (Wang and Xu 2003). In the FMCW technique, the difference of time is converted into (as well as it is amplified into) a frequency difference which could be easily measured (Casciati and Wu 2010). DMI uses the interference between two light beams to determine the displacement of an object. It could provide displacement measurement accuracy as high as from pm to nm when using the modular vibrometer system OFV-5000 from Polytec for example, but the maximum full scale displacement measurement range is relatively small: $\pm 82\text{mm}$ (Polytec 2012). However, they are very expensive. Regular-reflective laser sensors, which bases on the triangulation principle, can provides high accuracy for displacement

measurement, such as OMRON Z4M-S100 which provides a resolution of 0.008 mm within a measurement distance of 100 ± 40 mm(OMRON 2013). But their accuracy is affected by the angles of inclination at the measurement point or by the materials of the monitored objects (OMRON 2013). Contrarily, the laser sensor based on TOF can work in longer distance and provides stable accuracy for different materials of monitored objects and is insensitive to external light influences. Therefore, in this study, the laser sensor, YT89MGV80, available in the laboratory, was adopted.

Along this section, emphasis is also put on the noise of the wireless data acquisition device. As aforementioned, a cable can be a technical problem for the field experiment and a wireless sensor is preferred. Up to now, several wireless solutions have been proposed, such as the Stanford unit, Illinois Imote2, EMPA, Narada, MicroStrain, WiseSPOT and XMU unit (Chen 2011). But none of them provide flexible interface solution to currently universally utilized sensors which cannot really solve the technical problem. Moreover, they didn't address on the problem of noise introduced by the wireless sensor and cannot provide comparable accuracy to a wired system. This further limits their application onto the field experiment. Therefore, new wireless sensor systems were designed at the University of Pavia to provide flexible electrical interface and communication interface to universal utilized sensors (Chen 2011). Based on the results of laboratory tests, the second version of wireless sensing system was designed to further reduce the noise and improve the system stability. The resulting system is then suitable for field experiments and long-term monitoring.

This section investigates the possibility of increasing the accuracy of the wireless laser sensor. The wireless sensing unit is utilized to collect the data from laser sensor. The noise introduced by this wireless data acquisition system is assessed and several methods to mitigate the noise floor of both laser sensor and wireless sensing unit, such as signal processing based on multiple readings and the statistic characteristics of noise, and low noise design of the hardware circuit, were introduced.

3.2 Hardware of the wireless laser-based LPS unit

Figure 3.1 demonstrate the diagram of the wireless laser sensor. As one can see, the wireless laser sensor is composed of six modules: sensors, signal

conditioning module (adjustable amplifier and filters for each channel of signal), the analogue to digital converter (ADC) module, Microcontroller unit (MCU) and Static random-access memory (SRAM) module, wireless transmitter module, and power supply and management module.

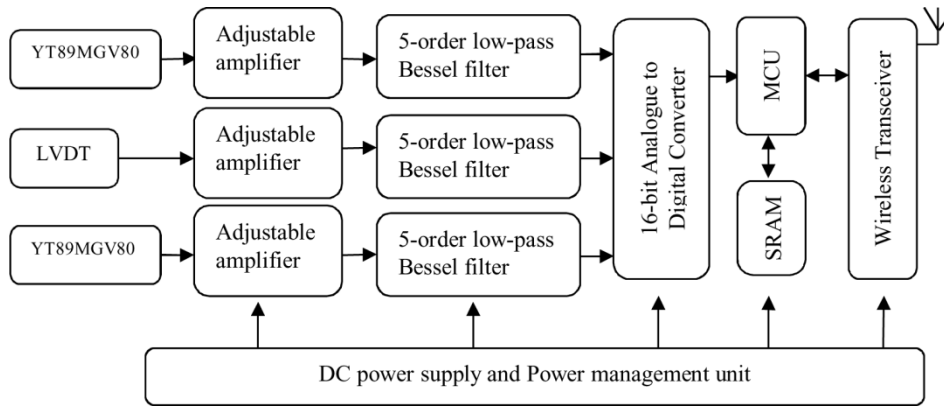


Figure3. 1 Diagram of the wireless signal collection board

In addition to the signals from the two laser sensors, named L1 and L2, the signal of the shaking table embedded LVDT (whose output is from -10V to +10V, corresponding to movement ranges from -75mm to +75mm), is also collected by the wireless data acquisition system.

Since the vibration to be measured could be relatively small, one adjustable amplifier is designed for each channel. Actual signals have finite duration and their frequency content, as defined by the Fourier transform, has no upper bound. Some amount of aliasing always occurs when such functions are sampled. That means the unwanted signal whose frequencies are higher than the Nyquist frequency (equal to $f_s/2$, half of the sample frequency) will be projected into the 0~ Nyquist frequency domain and cause aliasing. For this reason, a low-pass filter is designed for each channel to remove this high frequency signal before the signal is sent to the ADC module to obtain a series of 16-bit digital records. Normally, a voltage offset circuit is also demanded to make the sensor output to be electrical compatible with the input of ADC. For example, the output of the ADC is from 0 to 0xFFFF

which corresponds to the input from $V_{\text{ref}} - 2.5\text{V}$ to $V_{\text{ref}} + 2.5\text{V}$ (V_{ref} means reference signal). Given that the output of the laser sensor centers at 5V, the reference signal of the laser-sensor channels is set at 5V by a voltage offset circuit. The output of the LVDT centers at 0V: thence, the reference signal of the LVDT channel is set to be 0V.

The resolution is one important character one should consider when choosing the ADC unit. The resolution of the ADC must be good enough to discriminate the minimum changes one want to measure (Lockhart 2013) and the input voltage range of the ADC unit must be compatible with the output of the sensor it measures. In this wireless sensing system, a 16bits analogue-to-digital converter (ADC) is used.

The behavior of the ADC is controlled by a MCU and the resulting digital signals are cached in the SRAM to be sent to the storage computer by a wireless link. They are finally processed by Matlab.

3.2.1 The laser sensor YT89MGV80

The laser displacement sensor adopted in this case study is the YT89MGV80 which converts the distance from the sensor to a target object into a voltage output. Table 3.1 summarizes its properties: Static sensitivity, Linearity, Resolution, Working range, Temperature drift and Cut-Off Frequency. The “Static sensitivity” is defined as the ratio between the voltage output range and the magnitude of the mechanical input. In this case the voltage output is from 0 to 10 Volt while the mechanical input is 3000mm (centered at the “measuring distance”). Hence, the static sensitivity is 3.33mV/mm. The term “Linearity” denotes the maximum deviation of the calibration curve of the instrument from a straight line. For YT89MGV80, it is equal to 1.5%. With the purpose of minimizing the linearity deviation, when measuring the vibration of an object, one should ensure that the static distance from the laser sensor to the object is as close as possible to the “measuring distance” (as shown in Figure 3.2, the output of the YT89MGV80 at the “measuring distance”, is adjustable in a range of $\pm 200\text{mm}$ from 2000mm, is 5V). The “Resolution” is equal to 1mm: it is defined as the smallest measurable change in the size of the entry signal. Therefore, if one intends to convert the signal output from this laser sensor into a digital signal and to achieve the same nominal resolution, the ADC should be adequate to distinguish the smallest measureable change in the output of the laser sensor:

1mm, i.e., 3.33mV. As one can see, the “Working range” is from 300 to 3700mm, and the Cut-Off Frequency, which means the frequency response boundary of this laser sensor at which energy flowing through the system begins to be reduced, attenuated or reflected, rather than passing through, is 60Hz.

Table3. 1 The properties of YT89MGV80

Index	Static sensitivity	Linearity	Resolution	Working range	Temperature drift	Cut-Off Frequency
Value	3.33mV/mm	1.5%	1mm	300-3700mm	< 2 mm/°C	60 Hz

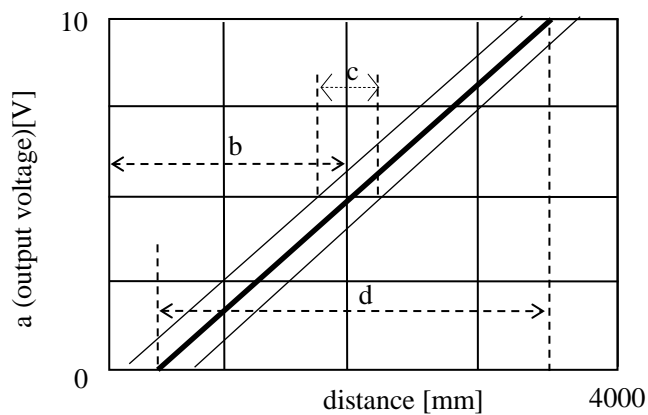


Figure3. 2 Sensing range of the YT89MGV80.

Note: The ordinate *a* is the analogue voltage output from 0V to 10V; along the abscissa, *b* is the measuring distance (2000mm), *c* is the measuring range adjustment (± 200 mm), *d* is the measuring range (3000mm, i.e., from 500(± 200 mm) to 3500mm(± 200 mm)).

In this work, the performance of the YT89MGV80 laser sensor is studied by the wireless sampling and transmission units. Two YT89MGV80 are utilized to improve its accuracy by taking the advantage of the correlation of the noises in two different laser sensors. The first sensor is pointed at an object at rest while

the second sensor is pointed at an object which is fixed on a shaking table. The chance improving the accuracy is investigated.

3.2.2 The first version of wireless DAQ system

A wireless sensor node is usually composed of sensor, signal conditioner, analog to digital converter, microcontroller, RF transceiver and power management module. As shown in Fig. 3.3, the wireless sensing unit designed by UNIPV consists of three amplifiers (AD620B) for three input channels, a 4-channel anti-aliasing Bessel filter, a 4-channel 16 bits ADC (ADS8343), a System on Chip (SoC) RF transceiver (CC1110), and a multiple outputs power management module with a 4.5Volts batteries power supply. The amplifier role is to amplify the analog signal output from the sensor. The amplification can indirectly help to improve the sampled signal resolution. Thus, a relatively lower resolution ADC is adequate. In addition, a low-pass filter is required to avoid the aliasing when there are signal components with frequency higher than half the ADC sampling frequency. In this work, a 5 order Anti-aliasing Bessel filter is utilized. The ADC role is to convert an analog signal into a digital series for consequent data processing algorithm. The SoC RF transceiver CC1110 includes not only a RF transceiver which is for RF wireless communication, but also a 8051 integrated microcontroller, such that another external microcontroller is not necessary. The microcontroller controls the activities of the wireless sensing unit through executing the embedded program. The RF transceiver (CC1110) adopted in this wireless sensing unit operates in ISM sub-1GHz instead of 2.4GHz, and uses its proprietary communication protocol instead of the commonly used standard ZigBee.

As a cable-replacement solution, the UNIVP wireless unit is designed to have flexible electrical interface with various laboratory existing sensors. Therefore the power management and signal conditioning modules are stressed. There are several power supply outputs in the power management module, including $\pm 12\text{V}$, $+5\text{V}$ and $+3.3\text{V}$. The output of $\pm 12\text{V}$ power supplies are adjustable in a wide range, (The output voltage of the $+12\text{V}$ power supply can be adjusted from input voltage up to $+28\text{V}$; The output voltage of the -12V power can be adjusted from -1V to -16V). The diagram of the power management module is illustrated in Fig. 3.4. The power management is implemented by 1 electronic switch (AO3401), 1 ultralow noise voltage reference (ADP431), and two types of

voltage regulators: LDO (low dropout regulator, MCP1700) and switching regulators (MAX1722, MAX618 and MAX765).

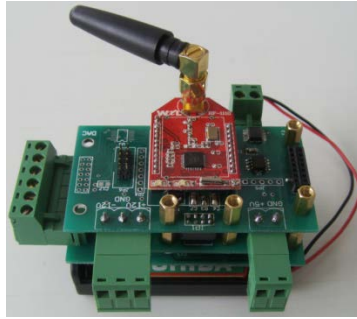
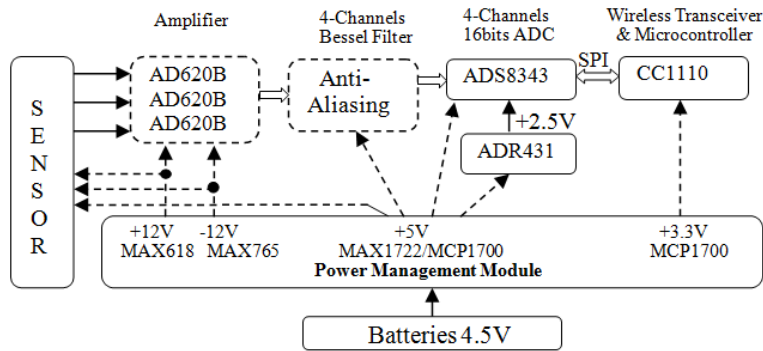


Figure3. 3 Component level block diagram (Top) and prototype (Bottom) of the wireless sensing unit

The batteries directly supply power to the first +3.3V LDO regulator for the SoC RF transceiver CC1110, and supply power to other regulators through the electronic switch which is controlled by the microcontroller inside CC1110. Therefore, only the power supply of CC1110 is not switchable, since it is the controller of the whole unit.

The 5.0V voltage supply is for filter and ADC which are sensitive to noise, so that it is implemented by a switching regulator MAX1722, which has a switching noise, followed by a second +5.0V LDO MCP1700 which acts as an active filter to filter the noise.

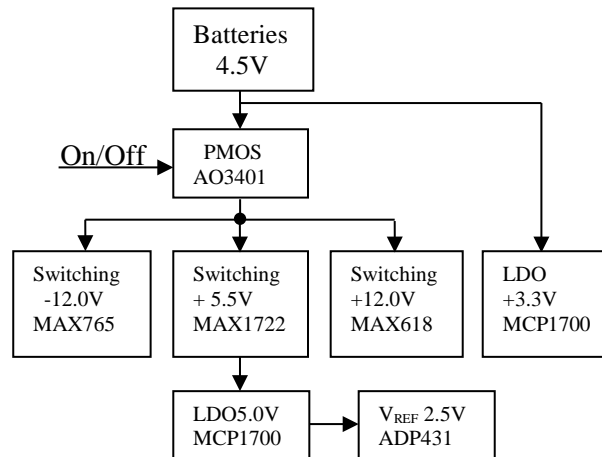


Figure3. 4 Block Diagram of the Power management.

When the electronic switch is off, in the wireless sensor only the CC1110 is powered. The overall supply current from the batteries consists of the quiescent current of the MCP1700 (only $1.6\mu\text{A}$) and current drawn by the CC1110 which has 4 power modes (PM). In PM2, the current supply is only $0.5\mu\text{A}$ and the microcontroller can be woken up by the internal timer. Figure 3.5 is the prototype of the power management module.

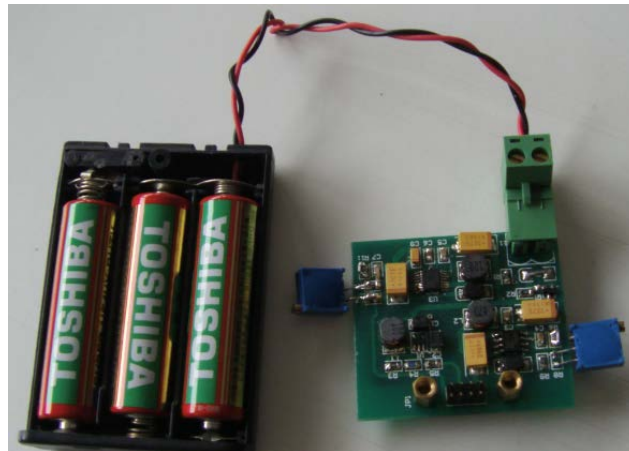


Figure3. 5 Prototype of the Power Management Module.

The PMOS (P-Channel MOSFET, metal-oxide-semiconductor field-effect transistor) power transistor AO3401 is used as electronic switch which can completely cut off the power supplies of sensor and some components of the sensing unit so as to minimize the power consumption when the wireless sensor is in sleep mode. The symbol of AO3401 is shown in Figure 3.6 where G is the gate for control, D is the drain and S is the source. In a sensing unit, S is directly connected to batteries, D is directly connected to the input of the switching regulators, and G is connected to the output pin of the CC1110. When G is pulled down to 0V, the channel between S and D will be open. When G is pulled up close to the voltage of the batteries, the channel between S and D will be closed.

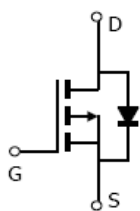


Figure3. 6 the PMOS AO3401

3.2.3 The updated version of the wireless DAQ system

One of the problems which are often encountered in wireless sensor links is the noise caused by the radio activity which requires a relative high current consumption. For example, if the radio sends data packet every 200ms, it might cause a spike noise of 5Hz in the power supply of the radio. In some way, the noise may be coupled to the amplifier in the signal chain especially when the gain is high, and then deteriorate the sampled signal, as one can see from Fig. 3.13. This problem is addressed from 3 aspects in the hardware design of this wireless sensor link.

Firstly, the analog ground path is completely separated from the digital ground path. Separating analogue and digital ground generally has to do with return currents and ground noise. Even though one considers GROUND as having zero impedance, it is a wire like anything else. Even ground planes have some impedance, and so currents flowing through these grounds cause voltage drops in the planes. Therefore, the digital circuit noise can get to the analogue signal

path if one does not separate grounding systems for digital and analogue parts (which are interconnected only in one place). Digital grounds are invariably noisier than analog grounds because of the switching noise generated in digital chips when they change state. For large current transients, PCB (Printed Circuit Board) trace inductances causes voltage drops between various ground points on the board (also known as "ground bounce"). Ground bounce translates into varying voltage level bounce on signal lines. For digital lines this is not a problem unless it crosses a logic threshold. For analog it's just plain noise to be added to the sampled signals. That is especially important for building an analogue to digital converter circuit, since the introduced noise will significantly reduce the resolution. The Analog-Ground (AGND) and Digital-Ground (DGND) pins of the ADC IC should connect to the analogue ground, preferably with it flooded under the whole IC package. Otherwise, noise on the DGND pin from the digital supply will get injected into the analogue section inside the IC. The analogue and digital grounds are connected together only in one single well-designed place. Besides, two completely separated power supplies are utilized for analogue circuit and digital circuit, which allow switching currents to be separated and optimized for each regulator, thus having analog power supply of low noise.

Secondly, an LC filter, which consists of an inductor (L) and a capacitor (C), is adopted in both the voltage regulators for analog and digital circuits to further filter out the ground bounce currents.

Lastly, low noise voltage regulators are adopted in the analog circuits.

In these ways, noise in analogue circuit is greatly reduced, as one can see from Fig.3.14 (Casciati, Faravelli et al. 2012).

In addition, a new wireless transceiver CC2430 is adopted in the new version of the wireless unit. Programmable gain of amplifier module and programmable switch off/on of different power supply module are also designed to facilitate the utilization of this new wireless sensing unit.

3.3 Firmware design of the wireless sensing unit

The embedded firmware is developed by C language in the integrated development environment IAR Embedded Workbench. The firmware mainly

includes communication module, sampling module, command modules. Figures 3.7 and 3.8 are the flowcharts corresponding to transmitting and receiving data. An acknowledgement and retry mechanism is used to ensure that a data packet is successfully received by the receiver.

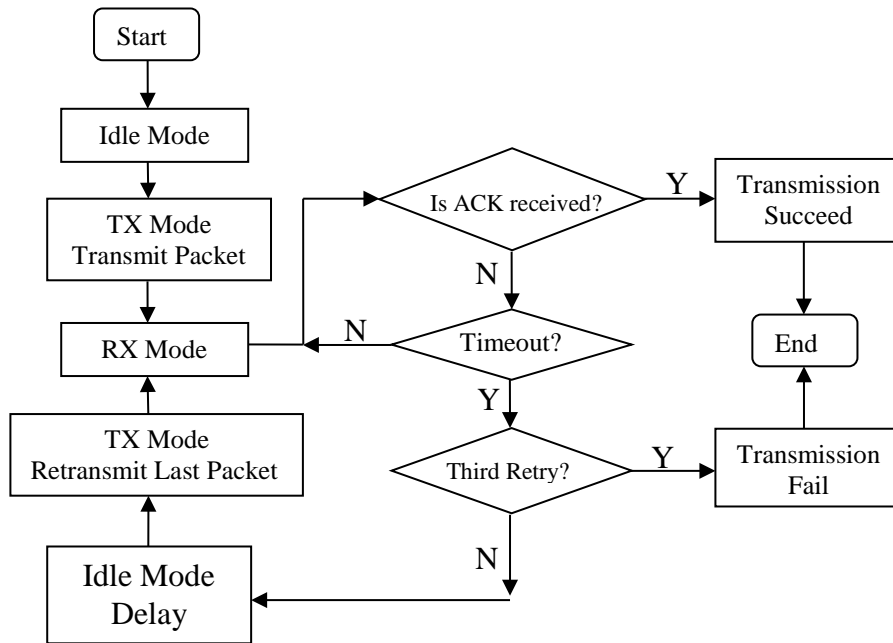


Figure3. 7 Transmitting a packet in reliable mode

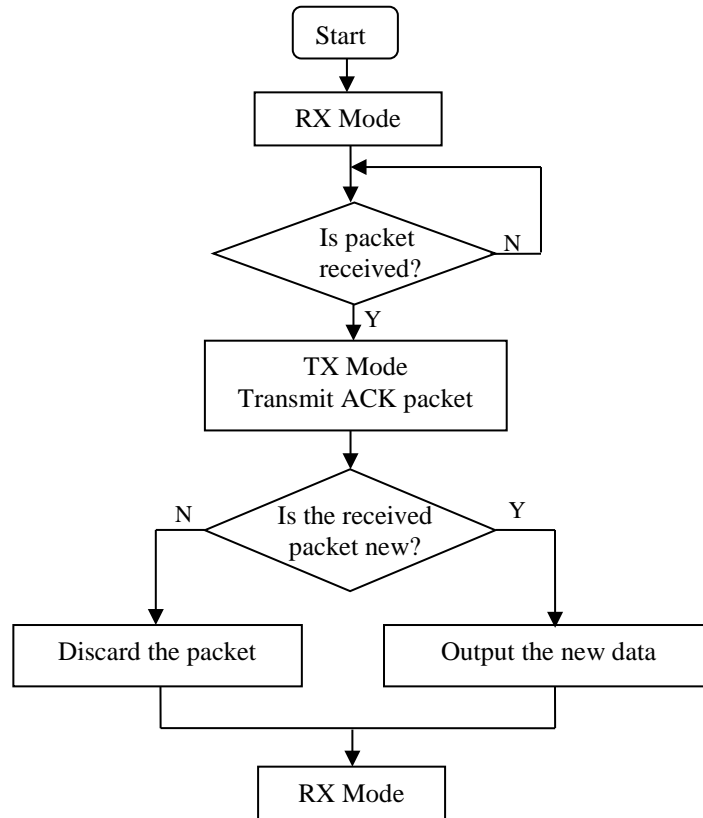


Figure3. 8 Receiving a Packet in Reliable Mode

Figure 3.9 is the wireless sensing unit software flowchart. The wireless sensing unit mainly performs three tasks: waiting for a start and stop sampling command in command channel, sampling the signal in a timer interrupt service routine, transmitting the sampled data to the base station unit in data channel. Indeed, each wireless sensing unit has two operating channels, its own data channel and the common command channel. As shown in Fig. 3.10, the wireless sensing units stay in command channel RX mode waiting for the starting sampling command from the command unit. Once they receive the start command, they turn on a timer designated for ADC. In the timer interrupt service routine, the signal sampling is executed by ADC to acquire the data which are then saved in a data buffer. When the data number in the buffer exceeds a threshold, the wireless sensing unit will pack the data into a data

packet, enter data channel TX mode and then transmit the packet to the corresponding base station unit by the reliable communication mode. Once the

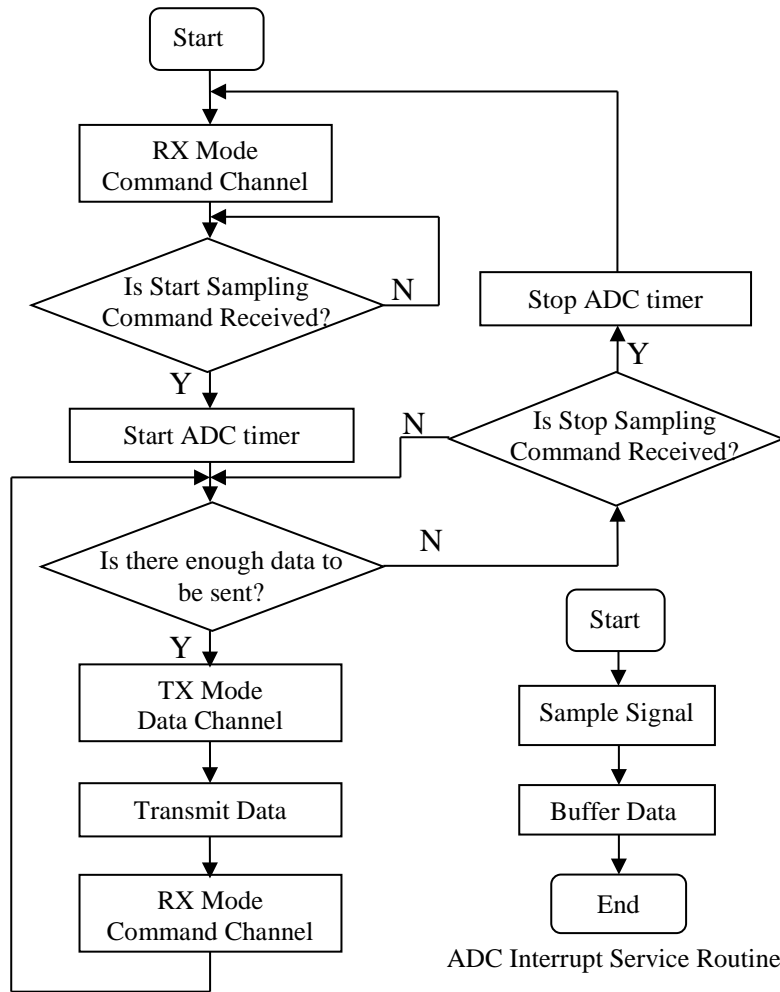


Figure3. 9 Wireless Sensing Unit Software Flowchart

packet is sent out, the wireless sensing units will switch to the command channel waiting for the stop sampling command. When a stop sampling command is received, the wireless sensing unit will turn of the ADC timer and will stay in command channel RX mode waiting for the start sampling

command. The start/stop sampling command is broadcast in command channel through the unreliable mode.

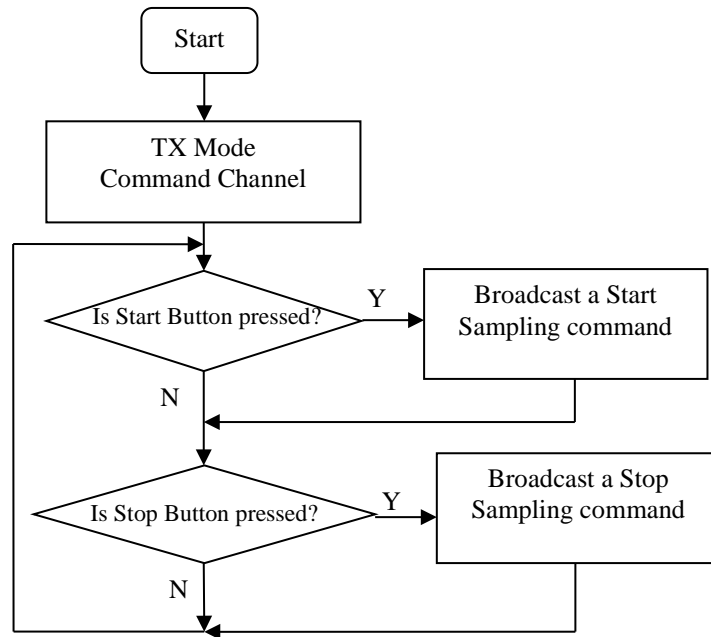


Figure3. 10 Command Unit firmware flowchart

Fig. 3.10 is the flowchart of software of the command unit. The command unit is designed to manually start, stop and synchronize wireless data acquisition from the sensors. It operates in a preset command channel and has two buttons, one is for starting sampling and the other one is for stopping sampling. Each wireless sensor will switch to the command channel right after finishing transmitting a data packet to its base station unit, and will return to its private channel when a new data packet is ready to be sent.

Signal Processing Methods

Comparing with a wired DAQ system, a wireless DAQ system is often regarded as characterized by a larger circuit noise and with lower signal resolution and quality. This further limits the application of a wireless DAQ system. In this

subsection, the cause of circuit noise is analyzed and then several signal processing methods are proposed and are proven to be effective.

3.4.1 The noise in wireless DAQ system

Thermal noise, which is caused by *Brownian* motion of electrons due to the circuit temperature, is present in any passive resistor above absolute zero temperature and represents a major limitation on the performance of most electronic circuits (Robinson 1962; Schreier, Silva et al. 2005). The thermal noise of a resistor R was first observed and explained in the early days of radio age by Johnson and Nyquist. Consider a resistor R in parallel with a capacitor C . As a result of the random thermal agitation of the electrons in the resistor, the capacitor will be charged and discharged at random. The average energy stored in the capacitor will be as Equation (3.1):

$$\frac{1}{2}C\overline{V^2} = \frac{1}{2}k_B T \quad (3.1)$$

Where C is the lead capacitance of the equivalent circuit of the resistor of resistance R (Ω) and $\overline{V^2}$ is the mean-square value of the voltage fluctuation impressed across the capacitor, k_B is the Boltzmann's constant (equal to 1.38×10^{-23} J/K) and T is the temperature of the circuit (K).

According to Nyquist's Theorem (Johnson 1928; Nyquist 1928), the one-sided noise power spectral density, or noise voltage variance (mean square) per hertz of bandwidth $\overline{v_n^2}$, is given by Equation (3.2)

$$\overline{v_n^2} = 4k_B T R \quad (3.2)$$

which means the spectral density is no frequency dependent. Noise with such a spectrum is called white noises. Its' samples are regarded as a sequence of serially uncorrelated random variables with zero mean and finite variance. In addition, according to the central limit theorem (CLT) (Paulauskas and Rackauskas 1989), the amplitude distribution of thermal noise is Gaussian, therefore it is called Gaussian white noise. This thermal noise is uncorrelated with the useful signal and therefore is additive noise. This noise contains equal power within any frequency band with a fixed width, therefore it possesses

relatively high power in the high frequency domain and introduces high frequency disturbance into the useful signal which reduces the resolution of the ADC result. Three methods to suppress this kind of noises and therefore increase the signal-noise-ratio (SNR) are discussed in this subsection: moving average filter, Gaussian filter and spectral subtraction filter.

3.4.2 Moving average filter

As said, the thermal noise is a white noise with zero mean and finite variance. Providing a sequence of independent samples of this noise, the mean will approach to 0 as the number of samples approaches infinite. Therefore, moving average filter can reduce the random noise while retaining a sharp step response. As the name implies, the moving average filter operates by averaging a number of points from the input signal to produce each point in the output signal. In equation form, this is written: (Smith 1997)

$$y[i] = \frac{1}{M} \sum_{j=0}^{M-1} x[i+j] \quad (3.3)$$

Where $x []$ is the input signal, $y []$ is the output signal, and M is the number of points in the average window. The increasing of M will increase the filter performance at the cost of more calculations and more time delay. The moving average filter acts as a low-pass filter whose roll-off is very slow and the stop band attenuation is ghastly. Clearly, the moving average filter cannot separate one band of frequencies from another. Indeed, a good performance in the time domain results in a poor performance in the frequency domain, and vice versa. In short, the moving average is an exceptionally good *smoothing filter* (the action in the time domain), but an exceptionally bad *low-pass filter* (the action in the frequency domain). Its' frequency response is mathematically described as Equation (3.4) and is shown on Figure 3.11(Smith 1997).

$$H[f] = \frac{\sin(\pi f M)}{M \sin(\pi f)} \quad (3.4)$$

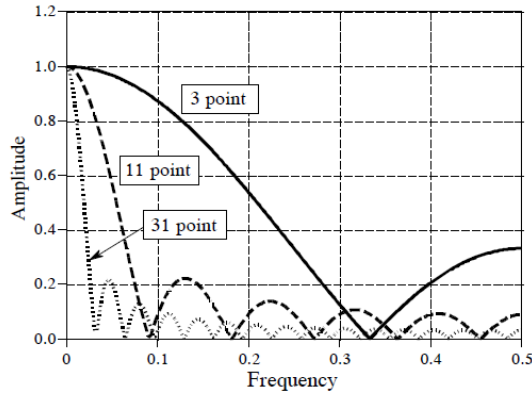


Figure3. 11 Frequency response of the moving average filter

3.4.3 Gaussian filter

As said, the thermal noise is a Gaussian white noise. It has been proven that the additive white Gaussian noise (AWGN) contaminating a signal can be better filtered by using a Gaussian filter with specific characteristics (Kopparapu and Satish 2011).

A Gaussian filter is a filter whose impulse response is a Gaussian function, as described by Equation (3.5).

$$G(x) = \frac{1}{\sqrt{2\pi}\sigma} e^{-\frac{x^2}{2\sigma^2}} \quad (3.5)$$

Where $G(x)$ is the impulse response, σ is the standard deviation of the distribution, while the mean is assumed to be zero.

Gaussian filters have the properties of having no overshoot to a step function input while minimizing the rise and fall time. Mathematically, a Gaussian filter modifies the input signal by convolution with a Gaussian function. Since the digital signal is stored as a collection of discrete samples, one needs to produce a discrete approximation to the Gaussian function before the convolution can be performed. In theory, the Gaussian distribution is non-zero everywhere, which would require an infinitely large convolution kernel, but in practice it is

effectively zero more than about three standard deviations from the mean, and so one can truncate the kernel at this point. Moreover, one can optimize the size of the convolution kernel according to the noise statistics to balance the filter effect and the amount of calculation.

3.4.4 Spectral subtraction methods

The previous two kinds of filter are mainly filtering the signal in the time domain. They work like a low-pass filter and improve the signal to noise ratio (SNR) through filtering out the high-frequency noise but not the low-frequency noise. According to the filtering characteristics, they even slightly magnify the low frequency noise and this brings distortion to the signal. As said, the thermal noise is white noise which is an additive uncorrelated noise to the useful signal. Therefore, the noise and the useful signal can be processed separately. The idea of spectral subtraction is that: one first obtains the estimated power spectrum of the noise and then subtracts it by the contaminating signal to obtain the pure signal. Spectral subtraction is universally applied to suppress the acoustic noise (Boll 1979; MARTIN 1994; Bing-yin, Yan et al. 2009; Waddi, Pandey et al. 2013).

Between 1950s and 1970s, Howells and Applebaum et al. (Howells 1965; Applebaum 1976) designed and built a system for antenna sidelobe cancelling that used a reference input derived from an auxiliary antenna and a simple two-weight adaptive filter (Widrow, Glover et al. 1975). The noise n_i acquired from the auxiliary antenna is filtered to produce an output y that is as close a replica as possible of the noise n_o which is added on to the useful signal s . This output is subtracted from the primary input $s + n_o$ to produce the system output $z = s + n_o - y$. In his case, the characteristics of the transmission paths (between the signal receiver antenna and the auxiliary antenna) are unknown or known only approximately and are seldom of a fixed nature, which will reduce the effective of the subtraction. Moreover, sometimes a secondary channel is not available. Therefore, based on the assumption that the characteristic of the noise is steady during a period of time, modified spectral subtraction based on estimating the noise during period when no useful signal is present in the input signal was proposed (Virag 1999).

Spectral subtraction is employed in the indirect measurement of bridge frequencies through two connected vehicles passing through the bridge, to

eliminate the blurring effect of surface roughness (Yang, Li et al. 2012). From the numerical study, this response-processing algorithm is verified to be feasible. Such direct subtraction of spectrum works since the blurring effect of the bridge surface roughness is a deterministic process.

When the noise is a random process, this subtraction should be executed carefully since subtracting noise from a received signal would seem to be a dangerous procedure. If done improperly it could result in an increase in output noise power (Widrow, Glover et al. 1975). That is because the noise in the finite length signal is approximated white noise and its spectrum cannot be predicted precisely. Direct spectral subtraction can sometimes be helpless to suppress the noise if the absolute value of the residual is larger than the minuend. Nevertheless, even though one cannot predict the actual spectrum of the noise, one can predict the statistics such as the mean and variance of the noise spectrum. Therefore, in this work, a spectrum subtraction method is proposed to improve the resolution of laser sensors based on the statistics of estimated noise: mean and variance.

In this case, a secondary channel of input is easily acquired and one can also assume the thermal noise within the two laser sensor is steady during a relative long period. Therefore, two laser sensors, L1 and L2, are utilized: L1 aims to a static object and works as a reference channel while L2 aims to a dynamic object to measure its movement. One first calculates the mean of the spectrum of L1 plus 5 times of its standard deviations, the values in the spectrum of L2 lower than the values in the spectrum of L1 are replaced by 0.

3.5 Experimental validation

The experiments reported in this section aims to study and find the route to improve the performance of the wireless laser sensor, both static and dynamic.

In the static experiments, the noise floor of the first version of the wireless DAQ system is studied. As said, in order to reduce the noise coupled with the digital module, the analog ground path in the PCB is completely separated from the digital ground path. The performance of the updated version of the wireless DAQ is tested. As one of the primary error sources, the temperature drift, which greatly affects the performance of the laser sensor during long-term monitoring, is also studied.

The dynamic performance of the laser sensor is also studied. Signal processing methods, including moving average filter, Gaussian filter and spectral subtraction, are utilized to improve the dynamic performance of laser sensor.

3.5.1 Static experiments

In this section, some experiments are carried out in order to study the noise floor of the wireless laser sensor and the efficiency of the proposed solution.

The first version of the wireless DAQ is utilized in the first experiment. Figure 3.12 displays the noises of both the wireless DAQ (red) and the wireless laser sensor (blue) and their spectrum. One can find out that the two noises are very close which means that the noise of this wireless laser sensor mainly contributed by the wireless DAQ system. Some regular spurious frequencies can be read from their spectra, which are at 5Hz, 10Hz, 15Hz, 20Hz and 25Hz. Even though the spectrum of these noises are small when compared to the actual signal (as shown in Figure 3.17) when the shaking table is moving with 1mm amplitude. But they dominate the static accuracy of the wireless laser sensor.

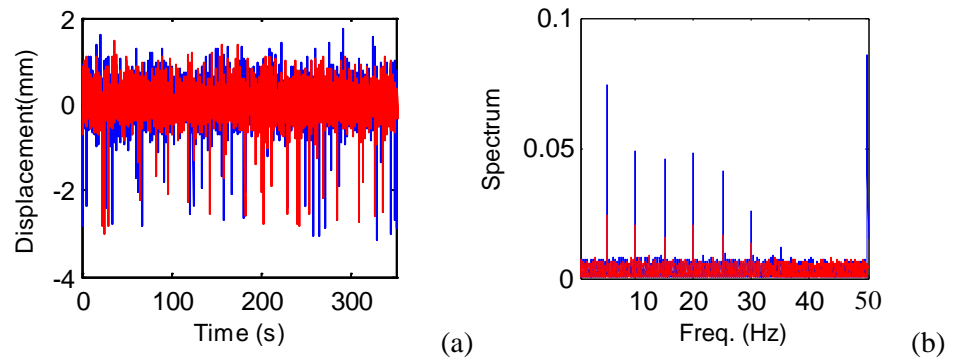


Figure3. 12 The noise of first version of wireless DAQ system (red) and the corresponding wireless laser sensor (blue).

They are mainly caused by the power management unit on the circuit. As known, a majority of the power of the circuit is consumed by the wireless transmitting module (belongs to digital portion of the circuit). In this case, the

wireless module transmits data around every 0.2 seconds which cause a surge of required current every 0.2 seconds. That generates a noise of 5Hz in the supplement of ADC modules (analogue module), and therefore introduce a noise of 5Hz and its harmonic components. The solution is based on separate the power supply of analogue module from the digital module which is one of several majority improvements of the updated version of wireless DAQ.

Figure 3.13 illustrated the noise in the updated version of the wireless DAQ and the updated version of the wireless laser sensor. As one can see, the spurious frequencies are eliminated and the noise of updated wireless DAQ (red) is greatly reduced and is much smaller than the noise of wireless laser sensor (blue). In addition, the noise shows good characteristics of white noise. This confirms the effectiveness of the proposed noise reduction techniques of the new wireless sensing unit.

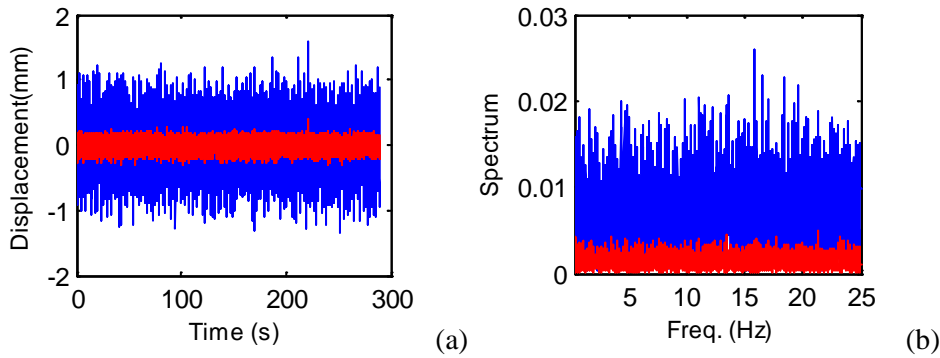


Figure3. 13 The noises of the updated version of Wireless DAQ system (red) and of the updated wireless laser sensor (blue).

As illustrated in Table 3.1, the measurement accuracy of a TOF laser sensor, YT89MGV80 is affected by the temperature blurring. Therefore, an experiment is also performed to investigate the relationship between the temperature drift and the distance of the measurement. The work distances of laser sensor are set to be about 750mm, 1050mm and 1350mm. The distance is measured in voltage and it is converted to distance according to Equation (3.6).

$$D = (2.5 + V) \times \frac{1000}{3.3} + 300 \quad (3.6)$$

Where D is the distance in unit of mm and V is the record signal in unit of V.

The temperature is changed through setting the operation temperature of air conditioning and is measured by a temperature sensor in real time at a frequency of 50Hz. The temperature is also measured in voltage and it is converted to temperature according to Equation (3.7).

$$T = \frac{1}{\frac{1}{298.15} + \frac{1}{3950} \lg \frac{1}{100} (-V + 1.5 - 100)} \quad (3.7)$$

Where T is the temperature Kelvin (K) and V is the recorded signal in unit of V.

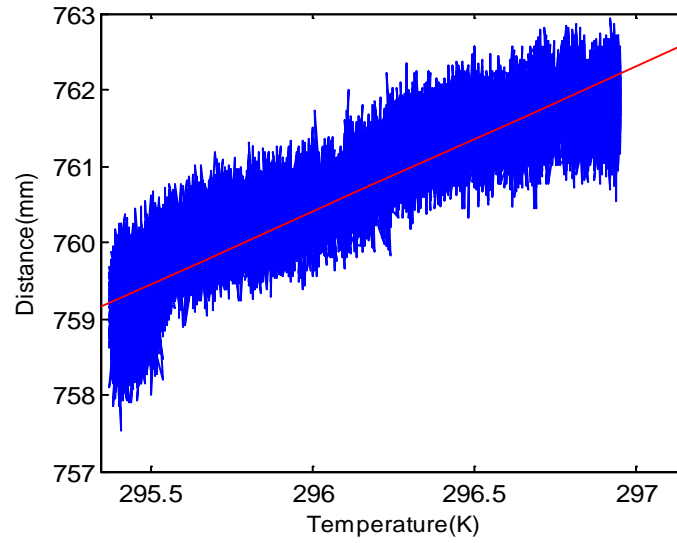


Figure3. 14 Temperature drift of the laser sensor when the working distance is 750mm.

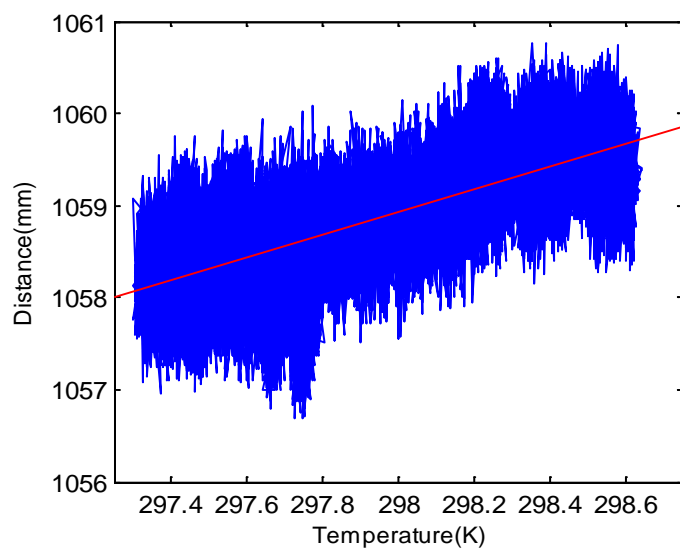


Figure3. 15 Temperature drift of the laser sensor when the working distance is 1060mm

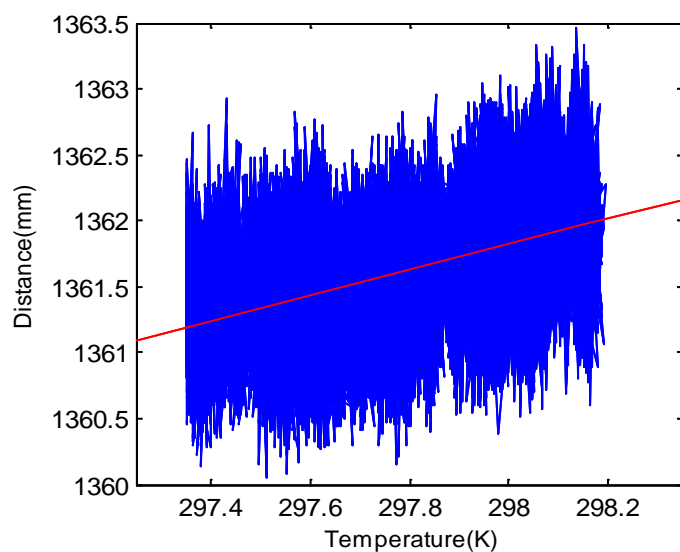


Figure3. 16 Temperature drift of the laser sensor when the working distance is 1350mm

Around 100,000 signal points are recorded for each experiment and the results are shown in the Figures from 3.14 to 3.16. From the figures, one can see that the temperature drift is the major contribution to the errors of the signal during long-term measurement: it is even more serious than the noise. According to the result from polynomial fitting, temperature drift slopes are different at different working distances: 1.9066mm/K for 750mm, 1.2283 mm/K for 1050mm, and .0.9762 for 1350mm. Therefore, in order to eliminate the effect of the temperature drift, the working distance should not be too small: the optimized work distance is about 1500mm. In addition, once calibrated, the accuracy of the laser sensor signal can be improved according to its working distance and the temperature measurement.

3.5.2 Kinematic experiments

In this section, the dynamic performance of the wireless laser sensor is studied through monitoring the motion of shaking table. Inside the shaking table, there is a linear variable differential transformer (LVDT) displacement sensor which can offer the real-time feedback of the shaking table's position. The feature of the LVDT sensor is shown in Table 3.2. As one can see, the conversion rate of the LVDT is 40 times of the one of YT89MGV80, which means the voltage output from LVDT is 40 times of the voltage output from the YT89MGV80 when they measures the same motion, as shown in Table 3.1 and Table 3.2.

Table3. 2 Features of the LVDT sensor

Feature of LVDT	Measurement range (mm)	Voltage range(V)	Conversion rate (mV/mm)
Value	(-75, 75)	(-10,10)	133.3

Table3. 3 Features of the wireless DAQ systems

	Conversion Bit (bits)	Magnify-gain of amplifier	Input voltage range(V)	The step of ADC
Wireless DAQ	16	(1,2 ¹⁴)	(-2.5,2.5)	76.3 μ V

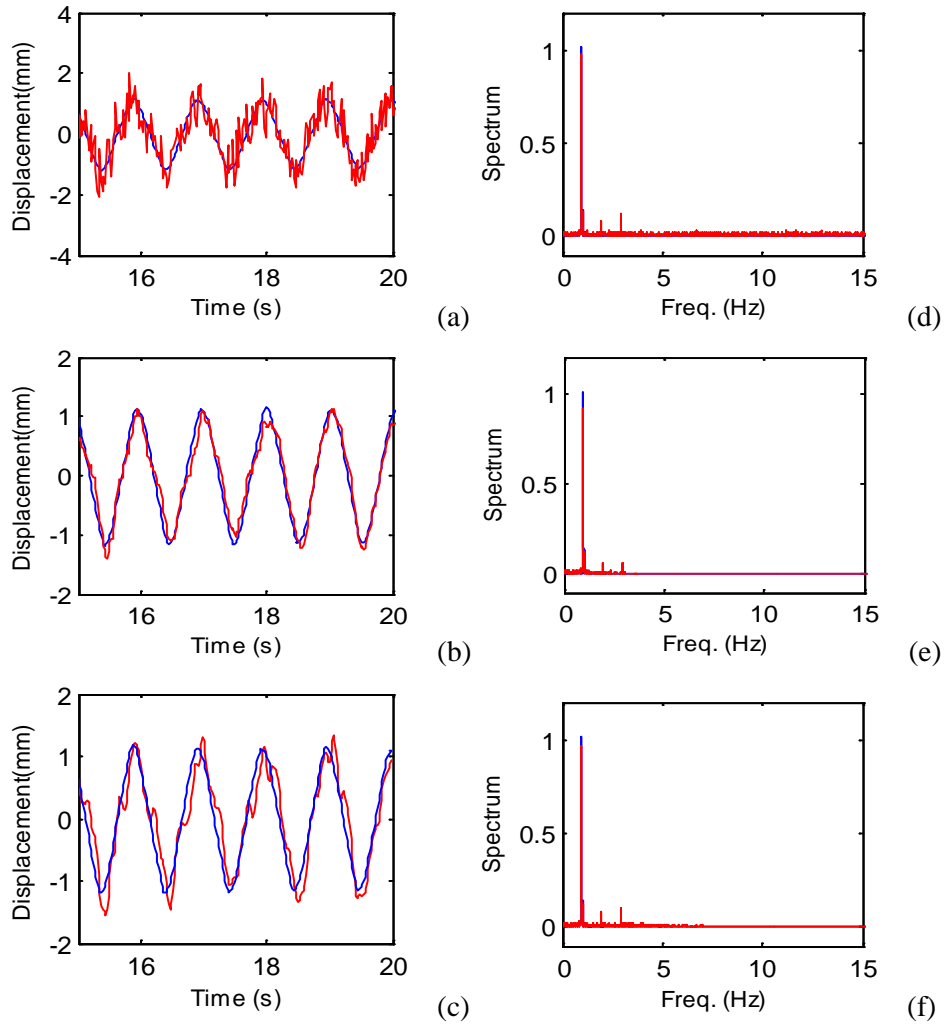


Figure3. 17 The results of laser measurement before and after applying the moving average filter and Gaussian filter to the original signal which is obtained when the shaking table moves at 1Hz with the amplitude 1mm. (a)original signal (b) signal filtered by MAV (c) signal filtered by Gaussian filter. (d)-(f) is the corresponding spectra of (a)-(c). Note: the red signal is recorded by the laser sensor while the blue signal is recorded by the LVDT sensor

First, the experiment is carried out with the shaking table moving sinusoidally with the frequency of 1Hz and the amplitude of 1mm which is the same as the resolution of the laser sensor according to Table 3.1. Since only the kinematic signal is of interest, the mean of each signal is removed in advance. The recorded signals are shown in Figure 3.17(a) and its spectra are shown in Figure 3.17(d): the red one is the signal of the laser sensor and the blue one is the signal of the LVDT sensor. As one can see, the signal from the LVDT is clean, while some noise is superimposed on the record from the laser signal. Therefore, the moving average filter and Gaussian filter are utilized to clean the signal: the results are displayed in Figure 3.17(b)(c)(e)(f): (b) and (e) correspond to the signal and spectra obtained from the average filter while (c) and (f) correspond to the signal and spectra obtained from the Gaussian filter. The spectra shows that the moving average filter and Gaussian filter can filter out the high frequency noise and therefore they work as a low-pass filter. In addition, it is observed that the time history obtained from the moving average filter is better than the one obtained from the Gaussian filter.

In Figure 3.17, the red waveforms denote the signal from the laser sensor and the blue ones denote the signal from the LVDT, as applicable for Figures from 3.18 to 3.21. Then a smaller signal with more complicate frequency components, $U(t)$, is adopted to examine the effect of the moving average filter. The results in Figure 3.19 confirm the effectiveness of this filter.

$$U(t) = 0.4\sin\pi t + 0.2\sin 2\pi t + 0.1\sin 8\pi t \quad (3.8)$$

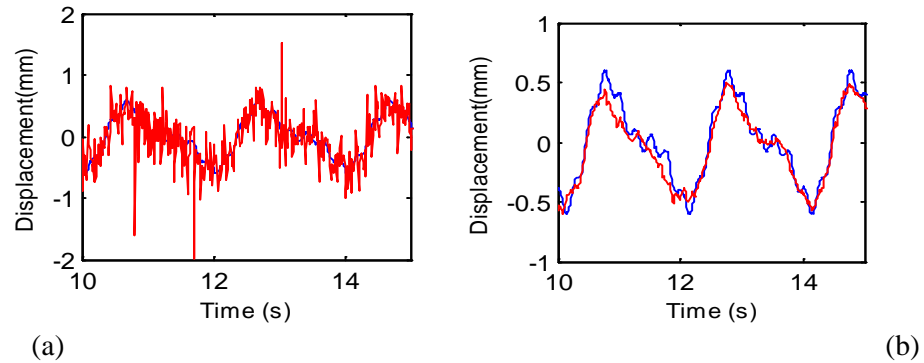


Figure 3.18 Results of applying the moving average filter to the signal obtained when the shaking table moves following the signal $U(t) = 0.4\sin\pi t + 0.2\sin 2\pi t + 0.1\sin 8\pi t$: (a) the recorded signal; (b) the filtered signal
Note: the red signal is recorded by the laser while the blue signal is recorded by LVDT.

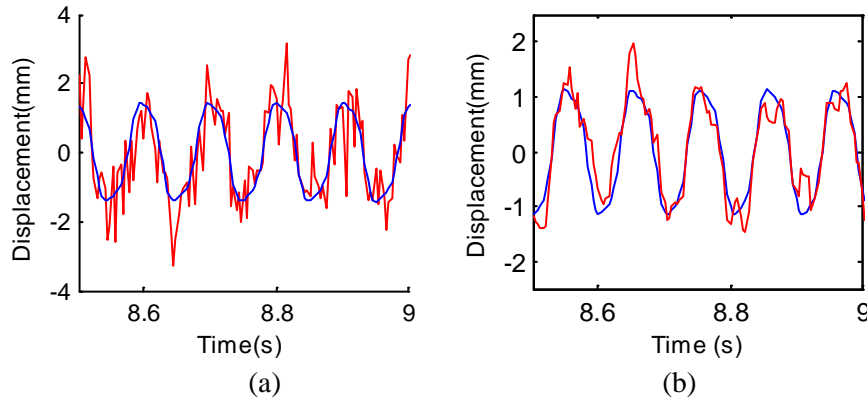


Figure 3.19 Results of the moving average filter when the shaking table moves sinusoidally with an amplitude of 1mm and a frequency of 10Hz; (a) the recorded signal, (b) the filtered signal. Note: the red signal is recorded by the laser while the blue signal is recorded by the LVDT.

Figure 3.19 shows that as the signal frequency increases, the noise is more severe. Figure 3.19 shows the effect of the moving average filter method when the shaking table moves at the frequency of 10Hz and the amplitude of 1mm. As one can see, the filtered signal is not so smooth due to the fact that: as a low-pass filter, the moving average filter can only filter out noise at high frequency and the remaining noise can be still considerable when the pass-band is wide. Therefore, the spectral subtraction methodology is adopted.

When the two laser sensors are installed close each to the other, it is reasonable to assume that they are suffering similar thermal noises. Therefore, it is feasible to clean the signal by working in the frequency domain and having the information on the two devices. The spectral subtraction method is then applied to remove the noise: the signal of the laser sensor 1 (L1), which aims to a static object, is subtracted from the signal of the laser sensor 2 (L2) as a correlative noise. However, instead of directly subtracting L1 signal from L2 signal, the subtraction is performed in frequency domain and the statistical means of both signals are employed in the subtraction since the correlative noise is proven to be a white noise.

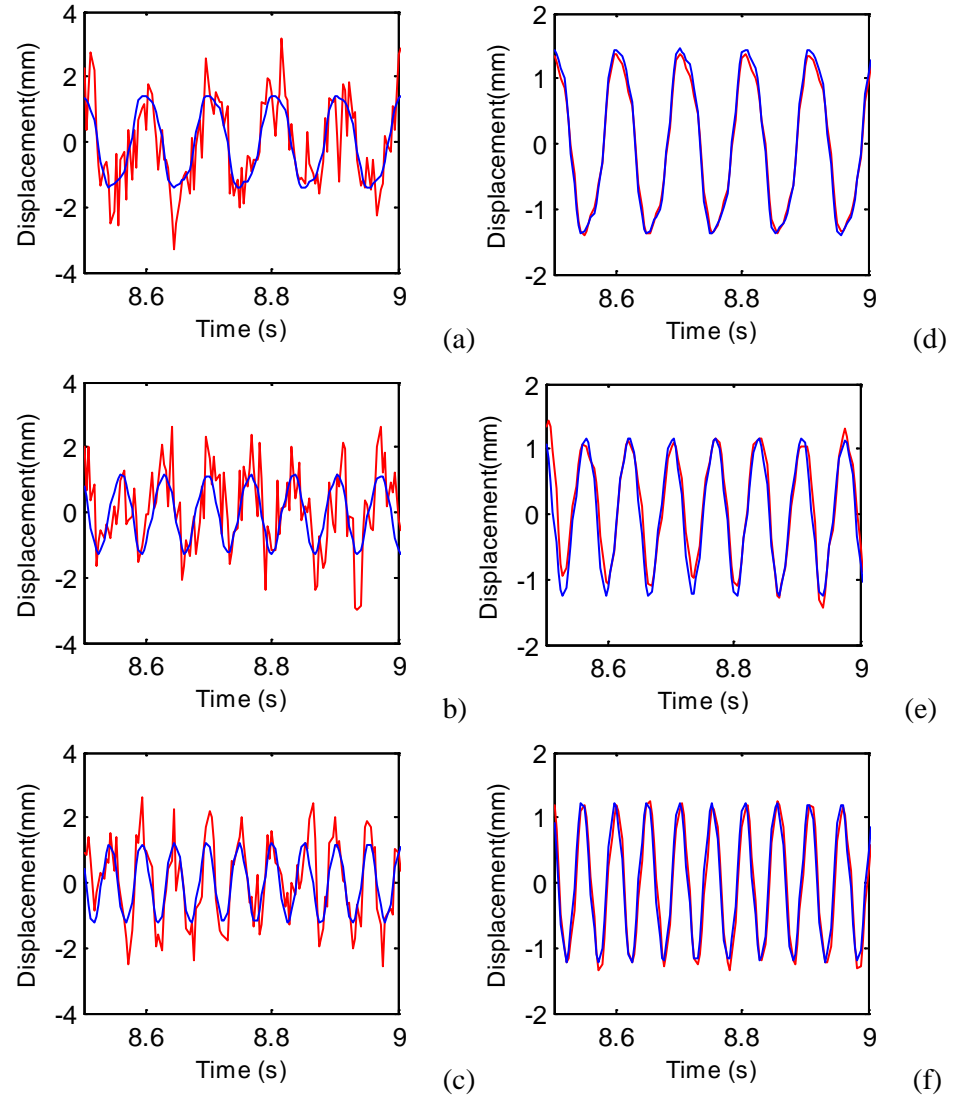


Figure3. 20 Performance of the spectral subtraction method-1.

(a),(b),(c) are the signals recorded when the shaking table moves at (1mm,10Hz), (1mm,15Hz), and (1mm,20Hz). (d)-(f) are the signal after applying the spectral subtraction method to (a)-(c). Note: the red signal is recorded by the laser while the blue signal is recorded by the LVDT.

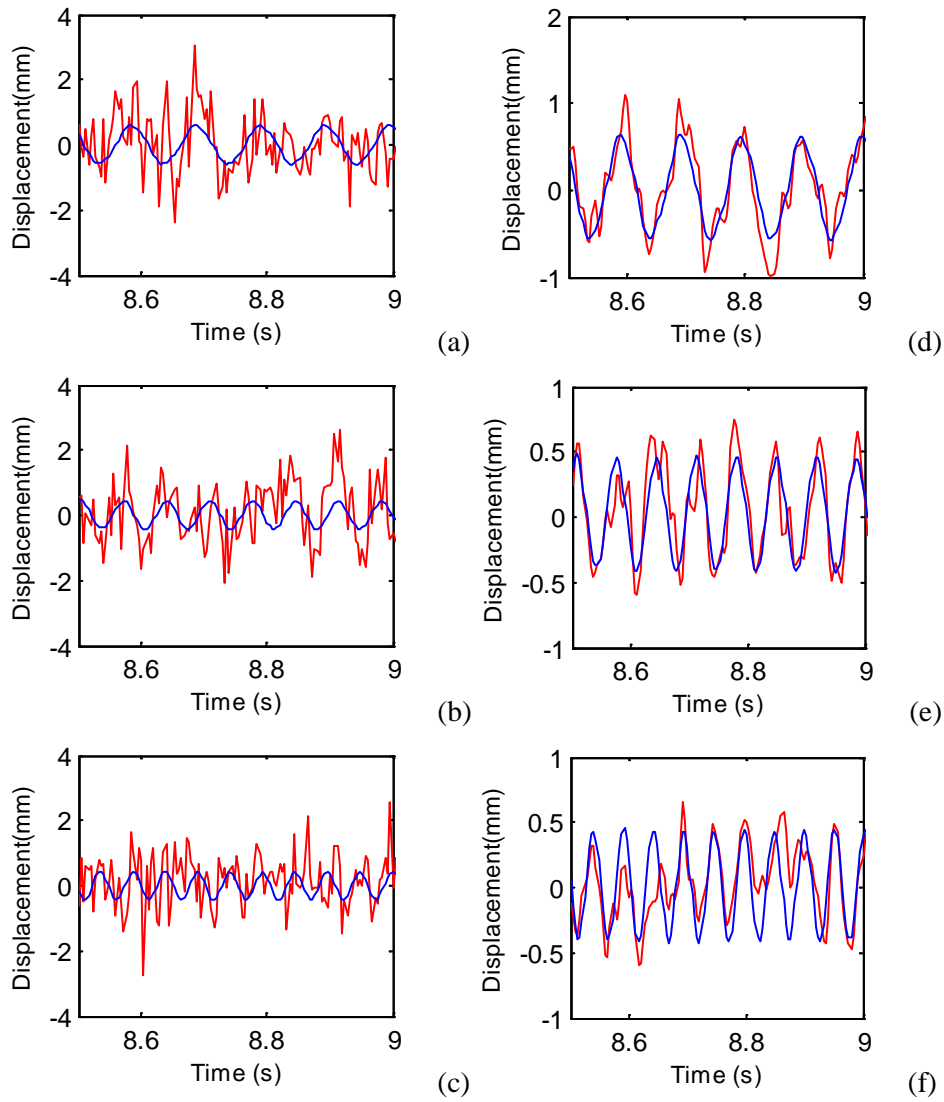


Figure3. 21 Performance of the spectral subtraction method-2.

(a),(b),(c) are the signals recorded when the shaking table moves at (0.5mm,10Hz), (0.5mm,15Hz), and (0.5mm,20Hz). (d)-(f) are the signals after applying the spectral subtraction method to (a)-(c). Note: the red signal is recorded by the laser while the blue signal is recorded by the LVDT.

Figure 3.20 illustrates the original signal when the shaking table moves at an amplitude of 1mm and the frequency of 10Hz, 15Hz, 20Hz ((a)-(c)) and the corresponding results obtained from spectral subtraction((d)-(g)). One can see that the spectral subtraction shows a better performance even when the noise is serious. Then the effectiveness of spectral subtraction is further examined by the signal recorded when the amplitude is reduced to 0.5Hz, as shown in Figure 3.21. The performance of this method is considerable.

Chapter 4 Vision based Local Positioning System

4.1 Introduction

Basically, the work based on the vision displacement measurement system can be categorized into two types according to the adopted camera models: finite camera models or infinite camera models which are discriminated by the position of their camera center: finite or infinite (Hartley and Zisserman 2004). As one can see in Fig. 4.1, when the object is near the camera, the finite camera model can be utilized. As the distance from the object to the camera increases, the focal length is also increased and the camera center is located farther. Therefore, the infinite camera model should be adopted. The representative finite camera model is pinhole model while the one for the infinite camera model is affine model which represents parallel projection.

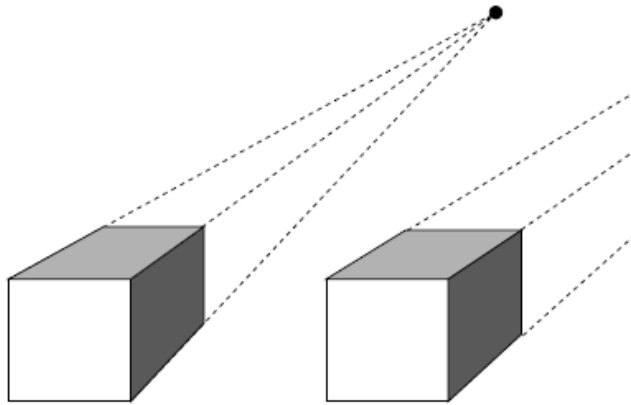


Figure 4. 1 the finite camera center (left) and the infinite camera center (right)

In the work of Lee (Lee and Shinozuka 2006; Lee, Cho et al. 2006), a tele-lens is utilized in the camera system in order to monitor the markers far away from the camera. The field of view in this system is close to the optical axis of the camera and the camera center is far from the object which could be denoted by the affine model. This system is tested in a field experiment and the result shows that its performance is comparable to a high resolution laser vibrometer.

Then the number of cameras in this system is extended through a time synchronization mean in order to monitor several targets simultaneously (Fukuda, Feng et al. 2010). For monitoring high rise flexible structures, a partition approach is proposed to extend the cover the range of this system (Park, Lee et al. 2010). Similarly, the affine camera model can be applied to the system constructed by Olaszek (Olaszek 1999). In this system, two channels are mounted on a camera: one aims to the target and the other aims to a reference target in order to reduce the error introduced by the change of camera position. In the study of Uhl (Uhl, Kohut et al. 2009), the working distance of the camera is several meters and the finite camera model can be applied. The reference image, which is taken when the optical axis is perpendicular to the interested plane, is assumed to be perspective distortion-free and is utilized to register images taken from other orientations by homographic mapping. A circular intensity pattern with a known diameter is used to obtain the scale factor (Uhl, Kohut et al. 2011). Indeed, the accuracy of measurement suffers from the optical distortions, such as radial distortion, decentering distorting or the prism distortion (due to the flawed radial curvature curve of the lens elements, the optical centers of lens elements are not strictly collinear) and imperfection in lens design and manufacturing as well as camera assembly. Those distortions greatly reduce the precision of the measurement result especially when the target of interest is located far away from the optical axis of the camera. In the study of Jurjo (Jurjo 2010; Jurjo, Magluta et al. 2010), the direct linear transformation is adopted to calibrate the projective distortion and this system is employed to monitor the dynamic characteristic of a slender structure model. In the work of Wieger (Wieger 2009), in order to eliminate the error introduced by the experiment condition, the motion of structure is projected by laser beams to two fix surfaces inside the a Displacement Recording Station (DRS), where the illumination condition is configurable. The motions of laser beams are recorded by the camera inside the DRS through which the motion of the structure can be calculated according to geometry. Since the lighting condition inside the DRS is configurable, the change of lighting conditions in the environment has minimal effects on this method and the size of the bridge is not a factor in the displacement calculation.

The vision-based displacement measurement is currently made available by ongoing technology developments. On one hand, the fast development of processors, such as PC, ARM, DSP, GPU or FPGA (Li 2011), provides the designer the flexibility to develop their image acquisition and processing system according to their application scene thanks to a great increase of the image

processing ability of the hardware. On the other hand, the image processing algorithm and the theory for computer vision have been well-developed in the last several decades (Gonzalez and Woods 2002; Hartley and Zisserman 2004). It is worth mentioning that Intel has developed three cross-platform libraries to support real time computer vision: Intel® Integrated Performance Primitives (Intel® IPP), Open Source Computer Vision (OpenCV) and Image Processing Library (IPL) (Intel 2012). For example, the OpenCV has C++, C, Python and Java interfaces for Windows, Linux, Android and Mac. Besides, there are some off-the-shelf image processing software tools available to realize a quick and comprehensive image processing, such as Image Pro Plus 6.0 (mediaCybernetics 2012) and Image gear (Accusoft 2012). In addition, Matlab also provides abundant functions for image processing and computer vision applications.

In this chapter, vision-based techniques are utilized to monitor the 2D motion of structures. The finite camera model, pinhole model, is first introduced and the full camera model is discussed when taking the optical distortion of lens into consideration. The calibration algorithms, direct linear transform (DLT) and registration, will then be elaborated. The parameters of the adopted camera are detailed after which the software, which includes the software for the image acquisition module and the image processing module, are elaborated. Several experiments are executed to examine the performance of the developed system both when the angle between the optical axis of the camera and the normal of the plane of interest is zero and when this angle is nonzero. The limitation of markers' density and the influence of different exposure periods to the measurement error will be discussed as well.

4.2 Theory and methodologies

4.2.1 2D projective geometry and camera model

In this work, the focal length of the utilized lens is 6-60mm while the working distance is around 3 meters. Hence, the 2-dimension distortion-free finite camera model, pinhole model, is adopted. One considers the projection of points in space $\mathbf{X}=(X, Y, Z)^T$ onto points on a plane $\mathbf{x}=(x, y)^T$. According to the projection geometry (Hartley and Zisserman 2004), the projection from a 3D space to a 2D space can be obtained by the Equation (4.1):

$$\begin{pmatrix} x_1 \\ x_2 \\ x_3 \end{pmatrix} = \begin{bmatrix} T_{11} & T_{12} & T_{13} & T_{14} \\ T_{21} & T_{22} & T_{23} & T_{24} \\ T_{31} & T_{32} & T_{33} & T_{34} \end{bmatrix} \begin{pmatrix} X_1 \\ X_2 \\ X_3 \\ X_4 \end{pmatrix} = \mathbf{T}_P \begin{pmatrix} X_1 \\ X_2 \\ X_3 \\ X_4 \end{pmatrix} \quad (4.1)$$

Where $(x_1, x_2, x_3)^T$ and $(X_1, X_2, X_3, X_4)^T$ are homogeneous coordinates related to \mathbf{x} and \mathbf{X} by Equation (4.2) and (4.3). Homogeneous coordinates are utilized in a projective geometry since it makes the projection, which includes scaling, rotation, translation and shear, be expressed in a linear transform (Hartley and Zisserman 2004).

$$(x, y) = \left(\frac{x_1}{x_3}, \frac{x_2}{x_3} \right) \quad (4.2)$$

$$(X, Y, Z) = \left(\frac{X_1}{X_4}, \frac{X_2}{X_4}, \frac{X_3}{X_4} \right) \quad (4.3)$$

Let the center of the projection, \mathbf{c} , be the origin of a Euclidean coordinate system, and consider the image plane as a plane $Z = f$. For the pinhole camera model, a point in space with coordinates \mathbf{X} is mapped to the point \mathbf{x} on the image plane where a line \mathbf{l} joining the point \mathbf{X} to \mathbf{c} meets the image plane. This is shown in Figure 4.2. The \mathbf{c} is called the camera center and the line from the camera center perpendicular to the image plane is called the principal axis, and the point where the principal axis meets the image plane is called the principal point. The plane through the camera center parallel to the image plane is called the principal plane of the camera. By similar triangles, one computes that the point $(X, Y, Z)^T$ is mapped to the point $(fX/Z, fY/Z, f)^T$ on the image plane.

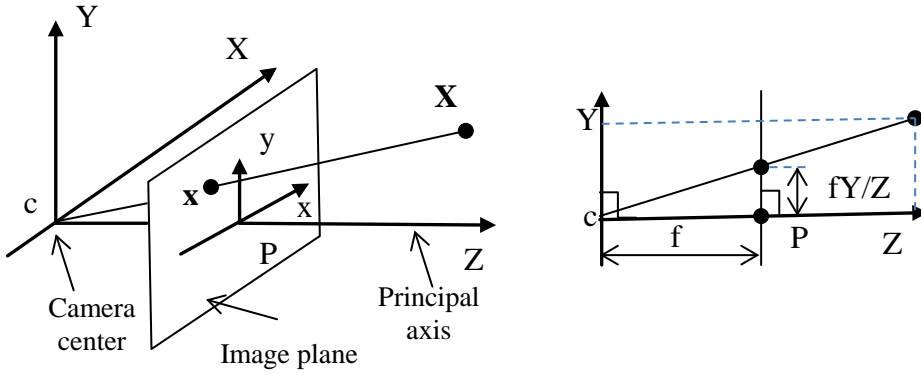


Figure 4. 2 The pinhole camera model and the projective geometry

This gives the familiar equation which describes the central projection mapping from the world to the image coordinates:

$$\begin{pmatrix} x \\ y \end{pmatrix} = \frac{f}{Z} \begin{pmatrix} X \\ Y \end{pmatrix} \quad (4.4)$$

Each point is scaled by its individual depth, and all projection rays converge to the optic center. If images are taken when the plane of interest is not parallel to the image plane, the depth-of-fields for different points are different, which means projective distortion will be introduced. According to Equation (4.4), one can obtain the transformation matrix of the pinhole camera model, as shown on Equation (4.5)

$$\mathbf{T}_p = \begin{bmatrix} 1 & 0 & 0 & 0 \\ 0 & 1 & 0 & 0 \\ 0 & 0 & 1/f & 0 \end{bmatrix} \quad (4.5)$$

Where the leftmost 3×3 sub-matrix of \mathbf{T}_p is a rotation matrix with its third row scaled by the inverse of the focal length $1/f$. Hereon, one can assume the X_4 in Equation (4.3) is equal to one since it works just as a scale factor. Equation (4.5) is obtained by assuming that the origin of coordinates in the image plane is at the principal point which may not be true in practice since one is apt to choose the left-down/ left-up point as the origin. So, in general there is a mapping

$$(X, Y, Z)^T \rightarrow \left(\frac{f}{Z}X + p_x, \frac{f}{Z}Y + p_y\right)^T \quad (4.6)$$

Where $(p_x, p_y)^T$ is the image coordinate of the principal point. Hence, the transformation matrix becomes:

$$\mathbf{T}_p = \begin{bmatrix} 1 & 0 & p_x/f & 0 \\ 0 & 1 & p_y/f & 0 \\ 0 & 0 & 1/f & 0 \end{bmatrix} \quad (4.7)$$

□

In general, points in a space will be expressed in terms of the world coordinate frame which is different to the projective coordinate frame. These two coordinate frames are related via a rotation and a translation (linear transformation and translation). If $\mathbf{x}' = (X, Y, Z)^T$ is an inhomogeneous 3-vector representing the coordinate of a point in the world coordinate frame, and \mathbf{x}_{cam} represents the same point in the camera coordinate frame, then one may write

$$\mathbf{x}_{cam} = \begin{bmatrix} r_{11} & r_{12} & r_{13} \\ r_{21} & r_{22} & r_{23} \\ r_{31} & r_{32} & r_{33} \end{bmatrix} \begin{pmatrix} X - X_0 \\ Y - Y_0 \\ Z - Z_0 \end{pmatrix} = \mathbf{R}(\mathbf{x}' - \mathbf{C}) \quad (4.8)$$

where $\mathbf{C} = (X_0, Y_0, Z_0)^T$ represents the coordinates of the camera center in the world coordinate frame, and \mathbf{R} is a 3×3 rotation matrix representing the orientation of the camera coordinate frame. Let \mathbf{X}_{cam} and \mathbf{X}' be the homogeneous coordinates of \mathbf{x}_{cam} and \mathbf{x}' , this equation may be written in homogeneous coordinates as

$$\mathbf{X}_{cam} = \begin{bmatrix} \mathbf{R} & -\mathbf{RC} \\ 0 & 1 \end{bmatrix} \begin{pmatrix} X \\ Y \\ Z \\ 1 \end{pmatrix} = \begin{bmatrix} \mathbf{R} & -\mathbf{RC} \\ 0 & 1 \end{bmatrix} \mathbf{X}' \quad (4.9)$$

Putting this together with Equation (4.7) and (4.1) leads to the general pinhole camera model

$$\mathbf{x} = \mathbf{T}_p \mathbf{R} [\mathbf{I} \mid -\mathbf{C}] \mathbf{X}' \quad (4.10)$$

where \mathbf{X}' is now the homogenous coordinates in a world coordinate frame. One

sees that a general pinhole camera has 9 degrees of freedom: 3 for \mathbf{T}_p (the elements f, p_x, p_y), 3 for \mathbf{R} (one for scale, one for rotation angle and the last for the shear), and 3 for \mathbf{C} . The parameters contained in \mathbf{T}_p are called the intrinsic camera parameters of the camera. The parameters of \mathbf{R} and \mathbf{C} which relate the camera orientation and position to a world coordinate system are called the extrinsic parameters. In image coordinates, the image is measured in pixels, supposing the number of pixels per unit distance in image coordinates are m_x and m_y in the x and y directions, the transformation from world coordinates to pixel coordinates can be obtained by multiplying Equation (4.10) on the left by an extra factor **diag** ($m_x, m_y, 1$). Thus, the general form of the transformation matrix of a CCD camera is

$$T_p = \begin{bmatrix} fm_x & 0 & m_x p_x \\ 0 & fm_y & m_y p_y \\ 0 & 0 & 1 \end{bmatrix} = \begin{bmatrix} \alpha_x & 0 & x_0 \\ 0 & \alpha_y & y_0 \\ 0 & 0 & 1 \end{bmatrix} \quad (4.11)$$

where $\alpha_x = fm_x$ and $\alpha_y = fm_y$ represent the focal length of the camera in terms of pixel dimensions in the x and y direction respectively. Similarly, $\mathbf{x}_0 = (x_0, y_0)$ is the principal point in terms of pixel dimensions, with coordinates $x_0 = m_x p_x$ and $y_0 = m_y p_y$.

As said, Equation (4.10) is the distortion-free pinhole camera model. In reality, there are also some geometrical distortions which are introduced by the camera optical characteristic (Weng, Cohen et al. 1992). These geometrical distortions are related to the position of image points in the image plane and it should be added into the ideal image position:

$$\begin{aligned} x' &= x + \delta_x(x, y) \\ y' &= y + \delta_y(x, y) \end{aligned} \quad (4.12)$$

Where (x', y') is the coordinates with distortion. As one can see from Equation (4.12), the distortion along each coordinate usually depends on the point position and it can be contributed by three kinds of distortions (Weng, Cohen et al. 1992):

- (1) Radial distortion, which is caused by an imperfect lens shape and manifests (e.g. flawed radial curvature curve of the lens elements), causes an inward or outward displacement of a given image point from its ideal

coordinates along the radial direction, as shown in Figure 4.3 and Figure 4.4. The radial distortion of a perfectly centered lens is governed by an expression of the following form:

$$\delta_{\rho r} = k_1 \rho^3 + k_2 \rho^5 + k_3 \rho^7 + \dots \quad (4.13)$$

Where, ρ is the radial distance from the measured point to the principal point of the image plane and $k_1, k_2, k_3 \dots$ are the coefficients of the radial distortion.

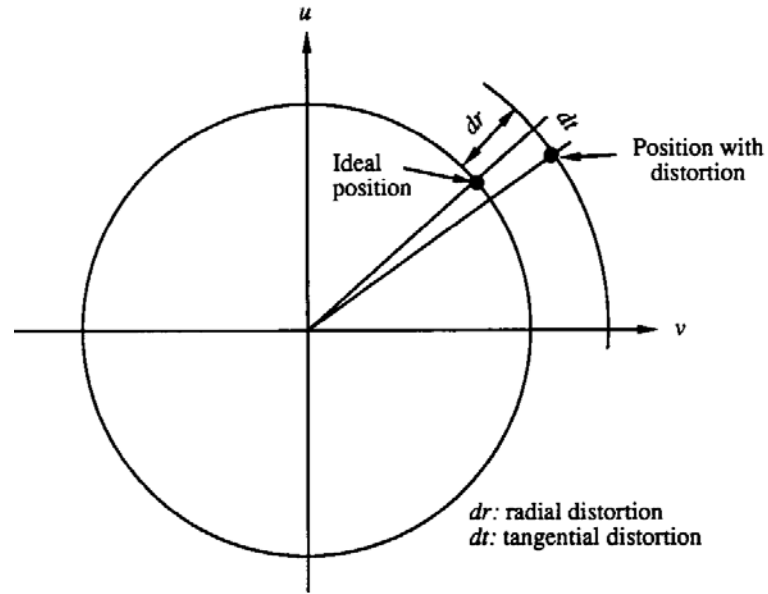


Figure 4. 3 Radial and tangential distortions

(2) Decentering distortion. Actual optical systems are subject to various degrees of decentering since the optical centers of lens elements are not strictly collinear. Decentering distortion has both radial and tangential components, which can be described analytically by the following expressions:

$$\begin{aligned} \delta_{\rho d} &= 3(j_1 \rho^2 + j_2 \rho^4 + \dots) \sin(\varphi - \varphi_0) \\ \delta_{td} &= (j_1 \rho^2 + j_2 \rho^4 + \dots) \cos(\varphi - \varphi_0) \end{aligned} \quad (4.14)$$

Where the (ρ, φ) is the polar coordinate of the image point, and the quantity φ_0 is the angle between the positive μ axis and a line of a reference known as the axis of the maximum tangential distortion as shown in Figure 4.5.

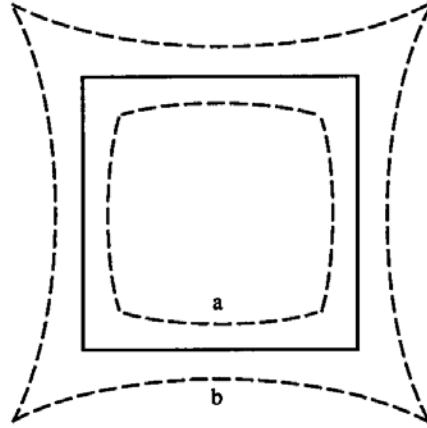


Figure 4. 4 effect of the radial distortion: solid lines, no distortion; dashed line, distortion

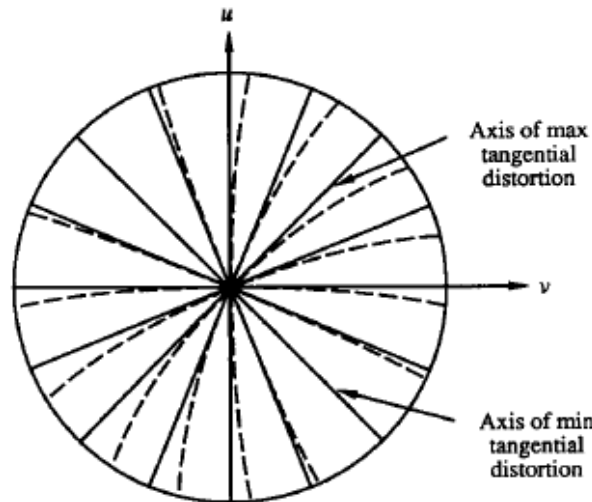


Figure 4. 5 Effect of the tangential distortion. Solid lines: no distortion; dashed lines: with tangential distortion

(3) Thin prism distortion, which is arisen from the imperfection in lens design and manufacturing as well as camera assembly. This type of distortion can be adequately modeled by the adjunction of a thin prism to the optical system, causing additional amounts of radial and tangential distortions. Such distortions can be expressed as

$$\begin{aligned}\delta_{\rho\rho} &= (i_1\rho^2 + i_2\rho^4 + \cdots) \sin(\varphi - \varphi_1) \\ \delta_{td} &= (i_1\rho^2 + i_2\rho^4 + \cdots) \cos(\varphi - \varphi_2)\end{aligned}\quad (4.14)$$

It is worth to note that, although both decentering distortion and thin prism distortion cause radial and tangential distortions, their axes of maximum tangential distortion are different.

Figure 4.6 shows the distortions obtained in one experiment executed by Feng et al. (Feng, Li et al. 2004) who use a camera to monitor a control plane on which 150 control points are evenly distributed. In order to reduce the camera production error, adequate calibrations are essential. Among several proposed distortion calibration algorithms, the most common one is direct linear transformation (DLT) (Walton 1981). The 2-D DLT will be introduced in next section.

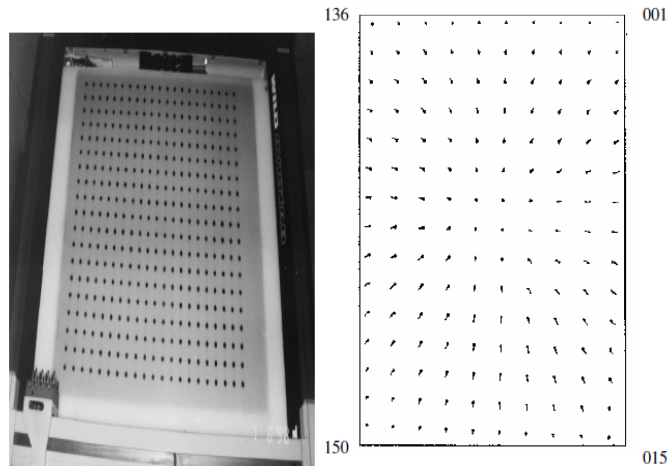


Figure 4. 6 Distortion distribution chart. Left: control plane, right: distortion distribution

4.2.2 2D direct linear transformation (DLT)

4.2.2.1 Camera calibration

As referred in last section, the projection from points on 3D space to 2D image plane can be expressed by the linear transform in Equation (4.15). Herein, the last item of inhomogeneous coordinates is normalized to 1, so as to simplify the following analysis. When 2D-2D projection is considered, one can simply suppose $Z=0$. Hence, Equation (4.16) is obtained. One can acquire the world coordinates of any point from its image coordinates if the transformation matrix \mathbf{H} is obtained.

$$\begin{pmatrix} x \\ y \\ 1 \end{pmatrix} = \begin{bmatrix} r_{11} & r_{12} & r_{13} & t_1 \\ r_{21} & r_{22} & r_{23} & t_2 \\ r_{31} & r_{32} & r_{33} & t_3 \end{bmatrix} \begin{pmatrix} X \\ Y \\ Z \\ 1 \end{pmatrix} \quad (4.15)$$

$$\mathbf{x} = \begin{pmatrix} x \\ y \\ 1 \end{pmatrix} = \begin{bmatrix} r_{11} & r_{12} & t_1 \\ r_{21} & r_{22} & t_2 \\ r_{31} & r_{32} & t_3 \end{bmatrix} \begin{pmatrix} X \\ Y \\ 1 \end{pmatrix} = \mathbf{H}\mathbf{X} \quad (4.16)$$

DLT is utilized to determine \mathbf{H} , with a set of four 2D to 2D point correspondences, $\mathbf{X}_i \leftrightarrow \mathbf{x}_i$. The transformation is given by the equation $\mathbf{x}_i = \mathbf{H}\mathbf{X}_i$. Note that this is an equation involving homogeneous vectors. In homogeneous coordinates, two vectors are equal to each other as long as their directions are the same even though their magnitudes are different (Hartley and Zisserman 2004). Thus the 3-vectors \mathbf{x}_i and $\mathbf{H}\mathbf{X}_i$ are not equal in magnitude, i.e. they have the same direction but may differ in magnitude by a nonzero scale factor. The equation may be expressed in terms of the vector cross product as $\mathbf{x}_i \times \mathbf{H}\mathbf{X}_i = \mathbf{0}$. This form will enable a simple linear solution for \mathbf{H} to be derived.

If the j -th row of the matrix \mathbf{H} is denoted by \mathbf{h}^{jT} , then we may write

$$\mathbf{H}\mathbf{X}_i = \begin{pmatrix} \mathbf{h}^{1T}\mathbf{X}_i \\ \mathbf{h}^{2T}\mathbf{X}_i \\ \mathbf{h}^{3T}\mathbf{X}_i \end{pmatrix} \quad (4.17)$$

The cross product may then be given explicitly as

$$\mathbf{x}_i \times \mathbf{H}\mathbf{x}_i = \begin{pmatrix} y_i \mathbf{h}^{3T} \mathbf{x}_i - \mathbf{h}^{2T} \mathbf{x}_i \\ \mathbf{h}^{1T} \mathbf{x}_i - x_i \mathbf{h}^{3T} \mathbf{x}_i \\ x_i \mathbf{h}^{2T} \mathbf{x}_i - y_i \mathbf{h}^{1T} \mathbf{x}_i \end{pmatrix} = 0 \quad (4.18)$$

Since $\mathbf{h}^{iT} \mathbf{x}_i$ is equal to $\mathbf{x}_i^T \mathbf{h}^j$ for $j = 1, 2, 3$, Equation (4.18) can be written into Equation (4.19)

$$\begin{bmatrix} 0^T & -\mathbf{x}_i^T & y_i \mathbf{x}_i^T \\ \mathbf{x}_i^T & 0^T & -x_i \mathbf{x}_i^T \\ -y_i \mathbf{x}_i^T & x_i \mathbf{x}_i^T & 0^T \end{bmatrix} \begin{pmatrix} \mathbf{h}^1 \\ \mathbf{h}^2 \\ \mathbf{h}^3 \end{pmatrix} = 0 \quad (4.19)$$

These equations have the form $\mathbf{A}_i \mathbf{h} = \mathbf{0}$, where \mathbf{A}_i is a 3×9 matrix, and \mathbf{h} is a 9-vector made up of the entries of the matrix \mathbf{H} where \mathbf{h}^{iT} is the i^{th} row of the matrix \mathbf{H} .

$$\mathbf{h} = \begin{pmatrix} \mathbf{h}^1 \\ \mathbf{h}^2 \\ \mathbf{h}^3 \end{pmatrix}, \quad \mathbf{H} = \begin{bmatrix} r_{11} & r_{12} & t_1 \\ r_{21} & r_{22} & t_2 \\ r_{31} & r_{32} & t_3 \end{bmatrix} \quad (4.20)$$

Although there are three equations in (4.19), only two of them are linearly independent. Thus each pair of coordinates (image coordinates and world coordinates) for a point gives two equations in the entries of \mathbf{H} . It is usual to write the set of equations as

$$\begin{bmatrix} 0^T & -\mathbf{x}_i^T & y_i \mathbf{x}_i^T \\ \mathbf{x}_i^T & 0^T & -x_i \mathbf{x}_i^T \end{bmatrix} \begin{pmatrix} \mathbf{h}^1 \\ \mathbf{h}^2 \\ \mathbf{h}^3 \end{pmatrix} = 0 \quad (4.21)$$

This will be written

$$\mathbf{A}_i \mathbf{h} = \mathbf{0} \quad (4.22)$$

where \mathbf{A}_i is now the 2×9 matrix of (4.21).

As said, each pair of coordinates for one point gives two independent equations in the entries of \mathbf{H} . Given four points, one obtains a set of equations $\mathbf{A} \mathbf{h} = \mathbf{0}$, where \mathbf{A} is the matrix of equation coefficients built from the matrix rows \mathbf{A}_i

contributed from each pair of points, and \mathbf{h} is the vector of unknown entries of \mathbf{H} . According to (4.21), \mathbf{A} has dimension 8×9 and thus \mathbf{A} has a 1-dimensional null-space which provides a solution for \mathbf{h} through which one can calibrate the coordinate of any point.

A better solution of \mathbf{h} can be acquired as more pairs of calibration points are utilized. Since there is unavoidable measurement noise in the value of \mathbf{x}_i and \mathbf{X}_i , more than four pairs of calibration points will compose an over-determined equation set. Therefore, the optimal \mathbf{h} should be estimated. That can be achieved through Singular Value Decomposition (SVD) method. Supposing six pairs of points are adopted, \mathbf{A} will be a 12×9 matrix. It can be decomposed into:

$$\mathbf{A} = \mathbf{U}\mathbf{D}\mathbf{V}^* \quad (4.23)$$

where \mathbf{U} is a 12×12 unitary matrix, \mathbf{D} is a 12×9 rectangular diagonal matrix with nonnegative real numbers on the diagonal, and \mathbf{V}^* (the conjugate transpose of \mathbf{V}) is a 9×9 unitary matrix. The diagonal entries of \mathbf{D} are known as the singular values of \mathbf{A} . The 12 columns of \mathbf{U} and the 9 columns of \mathbf{V} are called the left-singular vectors and right-singular vectors of \mathbf{A} , respectively. Since \mathbf{h} belongs to the null-space vector of \mathbf{A} , the optimal estimation of \mathbf{h} is the last right-singular vectors providing that the diagonal entries are arranged in descending order down the diagonal. The \mathbf{H} can be acquired according to Equation (4.20), and therefore the space coordinates of points can be reconstructed from its image coordinates according to Equation (4.16).

According to the positions of the four selected points, the calibration method can be performed in one of two ways: (i) extrapolation and (ii) interpolation, as illustrated in Fig. 4.7(a) and (b) (Jurjo 2010). In the first approach, the calibration can be performed based on the known dimensions of the structure or through the application of markers with pre-established distances in the structure itself. The advantage of this procedure is that it facilitates the acquisition of the actual data. However, extrapolating the measurements outside the region used for the calibration can result in a bigger error. In the second way, the calibration is performed through markers defining the borders of the region where the movement of the structure occurs. Therefore, any configuration of the structure will always be within the calibration region. Thus, the results obtained through this method are supposed to be more precise than those obtained by simple extrapolation. The disadvantage of this second method is that it is necessary to impose markers outside the structure, which in some cases can be

difficult (Jurjo, et.al, 2010). In our case, since the experiment is carried out in the laboratory, the interpolation calibration method is adopted.

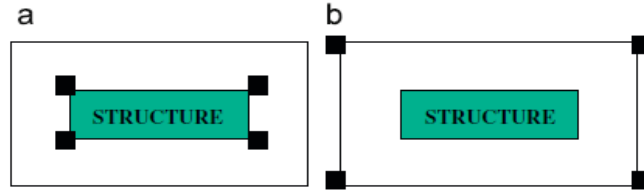


Figure 4. 7 Forms of calibration: (a) extrapolation and (b) interpolation

4.2.3 Registration

Image registration includes 1D intensity transformation and 2D spatial transformation (Zitová and Flusser 2003). The last one, which is considered in our work, is the process of spatially overlaying two or more images of the same object taken in different times or from different viewpoints or by different imaging machineries. When two images are taken as input, one of them is called reference image which is kept unchanged and used as the reference, whereas the other is called template image and is employed to register the reference image. Image registration seeks for the optimal transformation from the template image to the reference image which ensures the template one is close to the other as much as possible. This transformation then can be used to map points from the template image into the reference image. In this work, the 2D affine transformation is employed to remove the distortions introduced by rotation, translation, scale and shear. As shown in Figure 4.8 (Ashburner 2012).

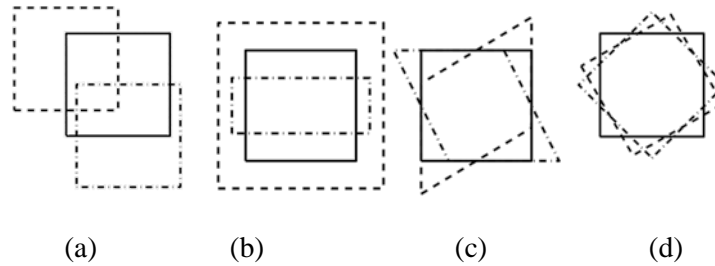


Figure 4. 8 Distortions calibrated by the registration (a) translation (b) scale
(c) shear (d) rotation

Supposing that $(x', y')^T$ and $(x, y)^T$ are the coordinates of the same point on the template image and the reference image, the homogeneous coordinates of $(x, y)^T$ is written as $\mathbf{X} = (x, y, 1)^T$. The transformation matrix is derived according to the potential distortions between two images. First, the translation is considered and it can be expressed as $\mathbf{T} = [t_1 \ t_2]^T$, then one obtains the following relational expression:

$$\begin{pmatrix} x' \\ y' \end{pmatrix} = \begin{bmatrix} 1 & 0 & t_1 \\ 0 & 1 & t_2 \end{bmatrix} \begin{pmatrix} x \\ y \\ 1 \end{pmatrix} = [\mathbf{I} \mid \mathbf{T}] \mathbf{X} \quad (4.24)$$

If the scale, which can be denoted by $\mathbf{S} = \begin{bmatrix} s_x & 0 \\ 0 & s_y \end{bmatrix}$, is taken into account, one obtains:

$$\begin{pmatrix} x' \\ y' \end{pmatrix} = \mathbf{S}[\mathbf{I} \mid \mathbf{T}] \mathbf{X} = \begin{bmatrix} s_x & 0 & t_1 \\ 0 & s_y & t_2 \end{bmatrix} \begin{pmatrix} x \\ y \\ 1 \end{pmatrix} \quad (4.25)$$

Then, the horizontal shear $\mathbf{H} = \begin{bmatrix} 1 & h \\ 0 & 1 \end{bmatrix}$ is considered,

$$\begin{pmatrix} x' \\ y' \end{pmatrix} = \mathbf{H}\mathbf{S}[\mathbf{I} \mid \mathbf{T}] \mathbf{X} = \begin{bmatrix} s_x & hs_y & t_1 \\ 0 & s_y & t_2 \end{bmatrix} \begin{pmatrix} x \\ y \\ 1 \end{pmatrix} \quad (4.26)$$

At last, the rotation $\mathbf{R} = \begin{bmatrix} \cos \theta & \sin \theta \\ -\sin \theta & \cos \theta \end{bmatrix}$ is included,

$$\begin{pmatrix} x' \\ y' \end{pmatrix} = \mathbf{R}\mathbf{H}\mathbf{S}[\mathbf{I} \mid \mathbf{T}] \mathbf{X} = \begin{bmatrix} s_x \cos \theta & hs_y \cos \theta + s_y \sin \theta & t_1 \\ -s_x \sin \theta & -hs_y \sin \theta + s_y \cos \theta & t_2 \end{bmatrix} \begin{pmatrix} x \\ y \\ 1 \end{pmatrix} \quad (4.27)$$

Equation (4.27) becomes (4.28),

$$\begin{pmatrix} x' \\ y' \end{pmatrix} = \begin{bmatrix} a_{11} & a_{12} \\ a_{21} & a_{22} \end{bmatrix} \begin{pmatrix} x \\ y \end{pmatrix} + \begin{pmatrix} t_1 \\ t_2 \end{pmatrix} \quad (4.28)$$

Where

$$\begin{aligned} a_{11} &= s_x \cos \theta & a_{12} &= h s_y \cos \theta + s_y \sin \theta \\ a_{21} &= -s_x \sin \theta & a_{22} &= -h s_y \sin \theta + s_y \cos \theta \end{aligned}$$

One can see there are six unknowns in Equation (4.28). Given coordinates of three or more than three pairs of points in both the reference image and the template image, one can obtain the transformation matrix and then perform the registration for any point.

4.2.4 Image processing routine

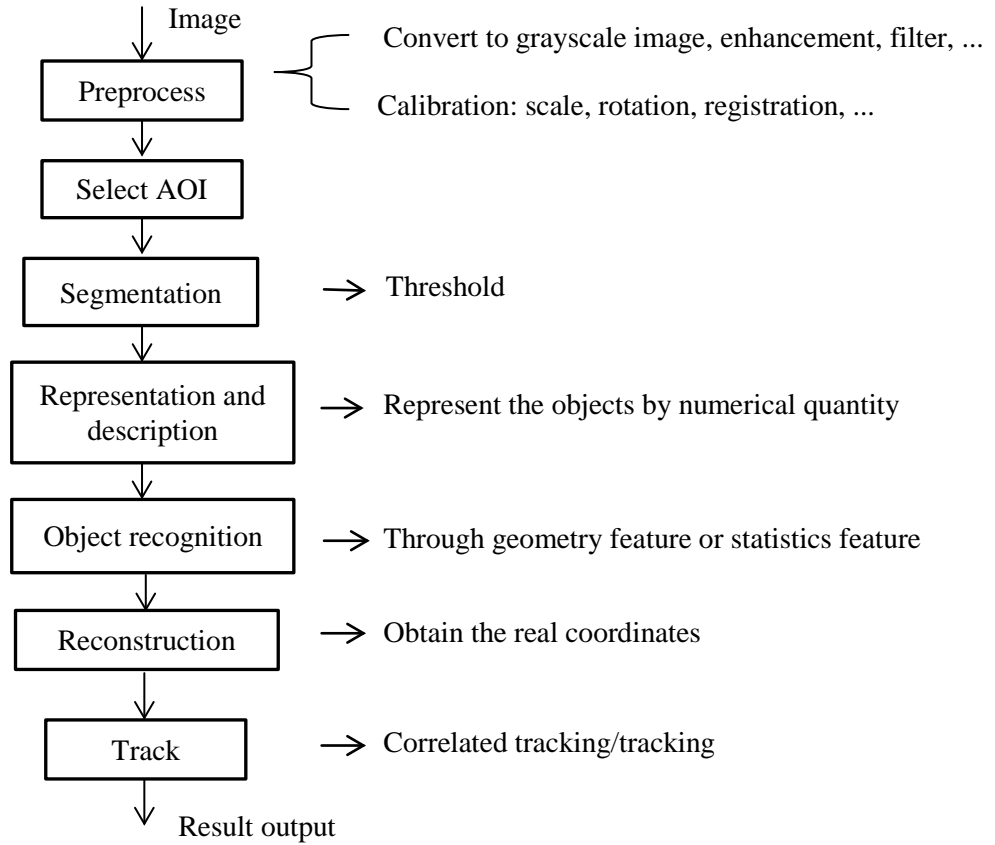


Figure 4. 9 Flow chart of the image processing procedure

This subsection is focused on the image processing procedure. After the images are digitalized and stored into the memory, image processing is carried out by the Image Pro Plus 6.0 software. The image processing procedure consists of seven steps, as summarized in Figure 4.9:

- (i) **Preprocessing:** the captured image is preprocessed before one focuses on the interested objects, i.e. markers. The preprocessing includes image enhancement, such as contrast enhancement or filter, and camera calibration, such as scale, rotation, registration or Direct Linear Transformation (DLT) etc. The captured images are true color images and they are first converted to grayscale images. To obtain an image that contains objects that are clearly distinguishable from the background, and have an intensity range/color different from other elements in the image, one first enhances the image quality by contrast enhancement or filtering. The purpose of camera calibration is to determine the transformation matrix that correlates the image coordinates and their respective actual coordinates. It can be done by simply obtaining the scale factor of the image through measuring the known dimension object. Or it can also be done by acquiring the transformation matrix through four pairs of corresponding points on both reference image and to-be-registered image. This process is the so called registration by which one can calibrate the projective distortion. Moreover, several calibration algorithms have been proposed to obtain the transformation matrix in order to calibrate the optical/electronic distortion introduced by camera/lens, such as DLT.
- (ii) **Select Area of Interest (AOI):** According to the tests of Olaszek, errors appear during direct observation of the structure and they might increase from 1 to 5 pixels (with no markers) (Olaszek 1999). Normally, proper markers are placed on the structure to specify the points of interest. That is reasonable since only few positions of the whole structure have to be followed. To reduce the computing load, AOIs are selected to limit the area to which the following processing is applied. Normally, the AOI can be selected based on the current position of the object and the prediction of its movement.
- (iii) **Segmentation:** segmentation subdivides an image into its constituent regions or objects and reaches its end when the objects or regions of

interest in an application have been detected. The accuracy of segmentation determines the eventual success or failure of computerized analysis procedures. Most of the segmentation algorithms are based on one of two basic properties of intensity values: discontinuity and similarity (Gonzalez and Woods 2002). In the first category, the approach consists in partitioning an image by detecting abrupt changes in intensity, such as edges. The principal approaches in the second category are based on partitioning an image into regions that are similar according to a set of predefined criteria. Thresholding is an example of method in this category. In the following applications, threshold is used to segment the markers from the background. Several algorithms were proposed to better determine the threshold adopted according to the feature of image, such as Otsu (Otsu 1979).

- (iv) Image representation and description. After an image has been segmented into regions, the resulting aggregate of segmented pixels usually is represented and described in a form suitable for further computer processing. Basically, representing a region involves two choices: (1) in terms of its external characteristics, i.e. its boundary; (2) in terms of its internal characteristics, i.e. the pixels within the region (Gonzalez and Woods 2002). After choosing a representation scheme, the region should be described in order to make the data useful to a computer. For example, if a region is represented by its internal characteristics, its internal characteristics can be described by features such as its area, texture, moment, etc.
- (v) Object recognition, also called pattern recognition: A pattern class is a family of patterns that share some common properties. After the imaged region is described by mathematic values, it can be assigned into the respective class through pattern recognition (Gonzalez and Woods 2002). Objects can be screened out by properly defining the classes. Once the object is recognized, its image coordinates can be obtained.
- (vi) Reconstruction: during this step, the actual world coordinates of recognized markers will be reconstructed by applying the transformation matrix acquired in step (i) to the image coordinates obtained in step (v).
- (vii) Repeat step (i)-(vi) to all images in this way, one can track the markers and obtain their displacements.

The measurement results can be exported to the Matlab or other software for further processing.

4.3 Operating Principle of a Digital Camera

A Charge Coupled Device (CCD) digital camera is adopted in this study. In this subsection, the operating principles of a CCD digital camera are first introduced as well as some technical terms. Then parameters of the adopted camera are given in detail.

4.3.1 CCD digital camera

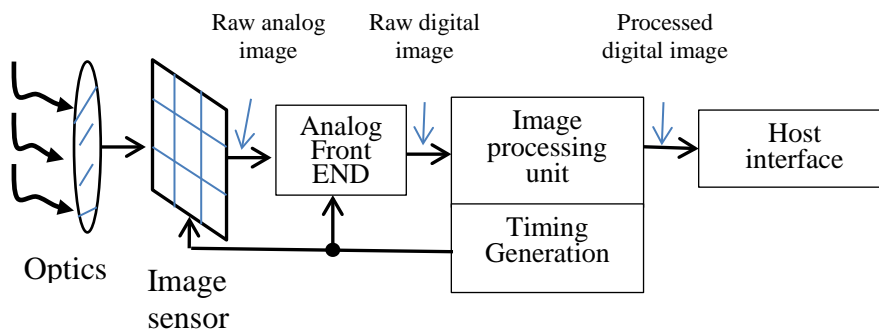


Figure 4. 10 Block diagram of typical image application

Similar to an analogue camera, a digital camera still needs all the physical parts, such as lens, shutter and focusing mechanism. But rather than simply having film to react to the light that makes up the image, a digital camera must have internally all the electronics necessary to capture the light and change it into a digital image file. Figure 4.10 shows a block diagram of a typical imaging system. The first component is made by the lens. All but the simplest cameras contain lenses which are actually comprised of several "lens elements." Each of these elements directs the path of light rays to recreate the image as accurately as possible on the digital sensor. The goal is to minimize aberrations (Cambridge in colour 2013). The remaining components involve three chips: an image sensor, an analog front-end (AFE), and a digital Application-Specific

Integrated Circuit (ASIC). The light passing through the lens is converted to an electronic signal by the sensor. The AFE conditions the analog signal received from the image sensor and performs the analog-to-digital (A/D) conversion. The digital ASIC contains image-processing, timing-generation circuitry, user interface driver and encoder (optional).

Before choosing a camera, there are several technical terms to be understood, such as lens focal length, sensor type, shutter speed, aperture, capture technology or field of view (FOV), which are explained below.

Lens Focal length: The quality of any image is as good as the quality of the lens which captures the light and bends it back towards the light receptor (CCD or film). A proper lens ensures the successful measurement. The lens focal length determines its angle of view, as shown in Figure 4.11. Wide angle lenses have short focal length, while telephoto lenses have longer corresponding focal lengths. Table 4.1 lists the typical uses of different focal length (Cambridge in colour 2013). In this study, the monitored object is a medium size building or a scale-reduced model in laboratory. Hence, a lens with adjustable focal length from 6 to 60mm is adopted.

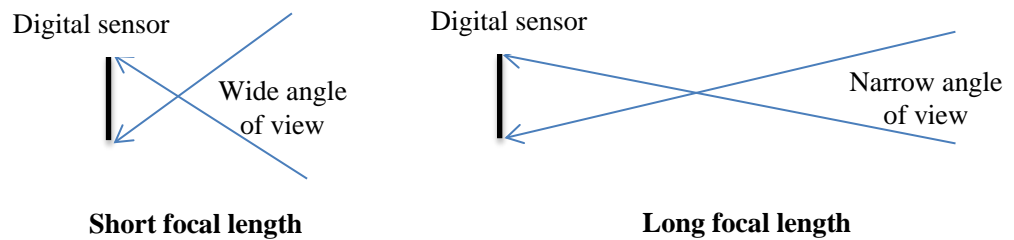


Figure 4. 11 The influence of the lens focal length

Shutter speed/Exposure time: Shutters work by revealing a light receptor (CCD sensor) to the light and then closing it again after the correct time has elapsed. The most important consideration when picking the right shutter speed is the movement you expect to capture. The slower the shutter speed is, the more motion is captured during that time period; a faster shutter speeds ‘freezes’ movements out of time.

Table 4. 1 Typical uses of different focal lengths

Lens focal length	Terminology	Typical photography
Less than 21mm	Extreme wide angle	Architecture
21-35mm	Wide angle	Landscape
35-70mm	Normal	Street& documentary
70-135mm	Medium telephoto	Portraiture
135-300+mm	Telephoto	Sports, bird & wildlife

Aperture: The aperture controls the area over which the light can enter the camera. Normally, it is listed in terms of $f/$ numbers, which quantitatively describe the relative light-gathering area, as illustrated in Figure 4.12 (Cambridge in colour 2013). The smaller the number, the larger the aperture area. If the illumination condition is low, a higher aperture is required.



Figure 4. 12 The relative light-gathering area for different apertures

CCD Sensor: CCD is a description of the technology used to move and store the electron charge. Within a CCD imager, all image processing is done off-chip, providing the maximum amount of space within each pixel to be used for capturing image information.

Capture technologies: There are a variety of different capture technologies that can be used to present the photo-receptor (imager) to the light patterns that make up the image within the camera (Jisc Digital Media 2012). The single matrix one-shot is the most common technology presently used within digital cameras. A matrix or grid of CCD elements is used to capture the whole image in one go, which provides instantaneous capture. The CCD only detect luminance (but not color) so the color information must be built up by having alternating colored coatings on each pixel, normally in a Red-Green-Blue-Green pattern. Every pixel can detect the intensity of the light that falls onto it, but the color of each pixel must be interpolated from the color-values of the surrounding pixels. One side effect of this type of capture system is that this interpolation requires lots of processing, which takes both time and power to

accomplish. This can slow the camera down, i.e., increase the time before it is ready for the next shot.

Field of view (FOV): FOV means the area one intends to capture. The FOV of each camera (vertical V and horizontal H) of view can be calculated according to the focal length f , the work distance W and the sensor sizes (v and h) (Equation (4.30)).

$$\frac{f}{W} = \frac{h}{H} = \frac{v}{V} \quad (4.30)$$

One can also estimate the image resolution which can be obtained by replacing the h and v by the corresponding sensor size of a single pixel.

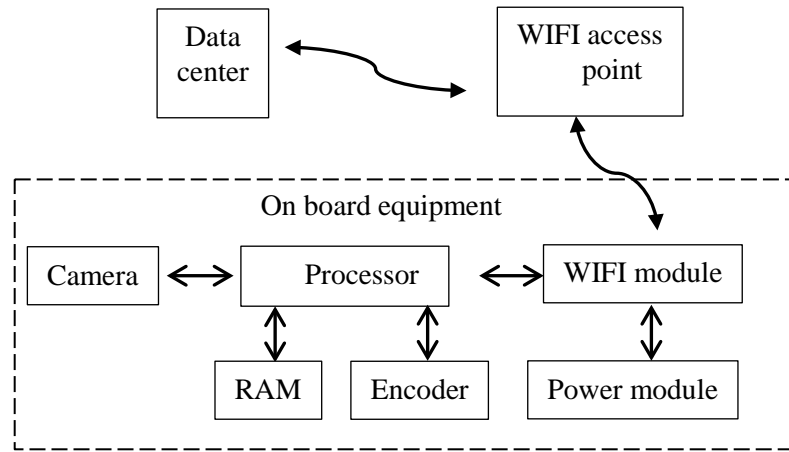


Figure 4. 13 Diagram of wireless camera

In some cases, real time image processing and wireless transmission are required, such as when applying the vision system in the field experiment. Figure 4.13 illustrates the mechanism of a wireless camera. The image collected by camera will be sent to the processor (GPU/ARM/DSP) to be processed by various image processing algorithms. Then, media encoder, such as Cypher7108 (Micronas 2006) can be used to compress the images to reduce the

data to be transmitted by WIFI module. A random access memory (RAM) is also essential to cache the image before it is sent out.

4.3.2 The camera

Two kinds of cameras are utilized in this work. One is the digital camera SunTime FX30VC. It is used to capture the motion of a single-story frame which is mounted on a shaking table. It provides 640 by 480 resolutions at 60 frames per second (fps), as one can read from Table 4.2. The parameters of the adopted lens are shown in Table 4.3.

Table 4. 2 The parameters of the SunTime FX30VC camera

Sensor	Pixel	Pixel Size	Frame rate	ADC	SDK	Inter-face	Shutter Speed	While balance
1/4" CCD color	640H × 480V	5.6 × 5.6 μm	60fps @ 640 × 480	8/12 bit	VC ++	USB	32μs-30min (global)	auto/manual

Table 4. 3 The parameters of the lens for the SunTime FX30VC

Focal length	field angle	close-up distance
6-60mm	53°- 5°	0.1m

The other camera, the monochrome camera SV642, is employed to capture the movement of a three- stories frame which is mounted on the shaking table. It provides 640 by 480 resolutions at 204 frames per second (fps). The captured image sequences of SV642 are sent to the PC for being processed through a PIXCI digital frame grabber for the PCI bus. Table 4.4 is the parameters of the SV642 camera.

Table 4. 4 The parameters of the SV642 camera

Pixel	Pixel size	Frame rate	ADC	Interface
640H × 480V	9.9 × 9.9 μm	204fps @ 640 × 480	8bits	ShieldedCAT-5 with RJ45 Plugs

4.4 Software implementation

The software consists of two parts: (1) image acquisition, which is programmed using Visual C++, provides the camera parameters configuration interface, captures the images and saves them into the memory; (2) image processing procedure, which is based on the Image Pro Plus 6.0 (IPP6.0) software and the Matlab environment.

4.4.1 Image acquisition

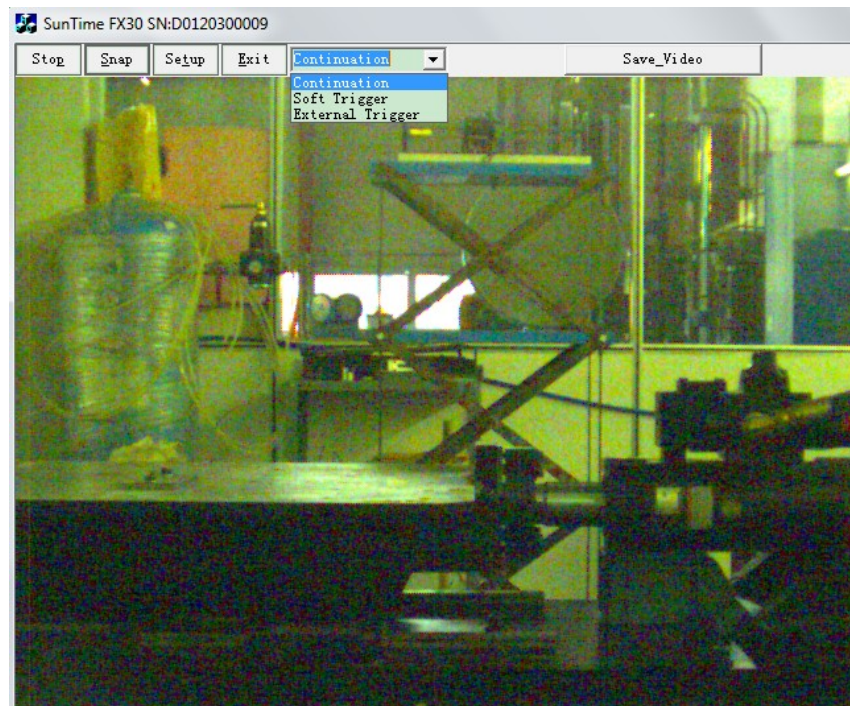


Figure 4. 14 The displaying dialog

The image acquisition software is programmed using Visual C++ and Microsoft Foundation Class Library (MFC). As an object-oriented program (OOP), Visual C++ may be viewed as a collection of cooperating objects, as opposed to the conventional model, in which a program is seen as a list of tasks (subroutines) to be performed (logicchild 2009). In OOP, each object is capable of receiving messages, processing data, and sending messages to other objects, and can be viewed as an independent 'machine' with a distinct role or responsibility. The actions (or 'operators ') on these objects are closely associated with the object.

For example, the data structures tend to carry their own operators around with them. The Microsoft Foundation Class Library (also Microsoft Foundation Classes or MFC) is a library that wraps portions of the Windows API in C++ classes, including functionality that enables them to use a default application framework. Classes are defined for many of the handle-managed Windows objects and also for predefined Windows and common controls.

Figure 4.14 shows the user interface of the image acquisition software. One can choose just save one image by “snap” or save the video. Several parameters of the camera can also be configured by “setup” sub-interface, as shown in Figure 4.15. The parameters mainly include the exposure method, white balance control, gamma filter and the frame rate of the camera.

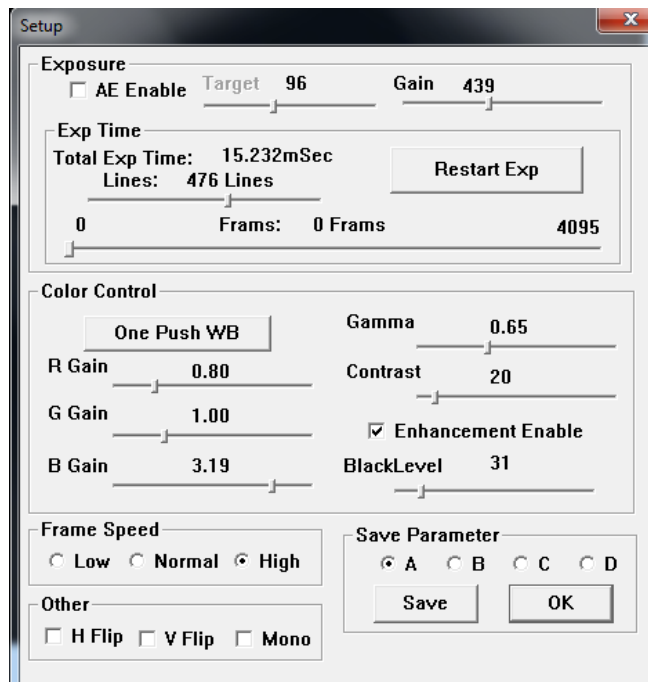


Figure 4. 15 The setup dialog

There are four classes in the image acquisition program: CAboutDlg, CDSCADEMOApp, CDSCAMDEMODlg and CSetup. CAboutDlg takes care of the software version information. CDSCADEMOApp is an application class which creates the application. Both CDSCAMDEMODlg and CSetup are

inherited from CDialog, the first one takes care of the main window of the graphic user interface (GUI) which is shown in Figure 4.14 while the CSetup dialog provides user to configure the parameters of the camera which is displayed in Figure 4.15. Figure 4.16 shows the construction process of the image acquisition program. The indentations indicate that the function in current line is called by the one of the previous one. First, CDSCAMDEMOApp class create a new application object, called 'theApp'. This is the unique application object in this program and this application will exist among all the runtime. Then CDSCAMDEMOApp::InitInstance() is called to initialize an instance for 'theApp'. Inside CDSCAMDEMOApp::InitInstance(), CDSCAMDEMOMDlg class is used creates a new dialog object 'dlg' to take care of the GUI in Figure 4.14. When one click "Setup" button in this GUI, CDSCAMDEMOMDlg::OnSetup() will be called. Inside this function, Csetup class will be used to allocates a class pointer for CDSCAMDEMOMDlg::m_SetupDlg and thus an Csetup object is created dynamically. Then one is able to configure the Setup window.

The last second line means that if one click "Close" button of the Setup window, one message will be produced and the function CSetup::OnClose() will react to this message. The last line means that function CDSCAMDEMOMDlg::OnExit() will react to the message produced when on click the 'Exit' button of the dlg window.

```

CDSCAMDEMOApp class create a new application object 'theApp'
  CDSCAMDEMOApp::InitInstance() to initialize an instance for 'theApp'
    CDSCAMDEMOMDlg class creates a new dialog object 'dlg'
      CDSCAMDEMOMDlg::OnSetup()
        Csetup class allocates a class pointer for CDSCAMDEMOMDlg::m_SetupDlg
      CSetup::OnClose() to react to the 'Close' message
      CDSCAMDEMOMDlg::OnExit() to react to the 'Exit' message

```

Figure 4. 16 Construction process of the image acquisition program

In the program, there are three threads: a user interface thread and two worker threads. Figure 4.17 illustrates the interaction of three threads of the software. The user interface thread is the main thread in the software which is active from the very beginning and ends when the software exits. The first worker thread, snapThreadCallback(), is created by main thread in CameraInit() to receive images from the camera driver and call the Imag_Process() function. Inside the

Image_Process(), the second worker thread: ImageProcThread, which is created by AfxBeginThread(), will be informed to save image and video.

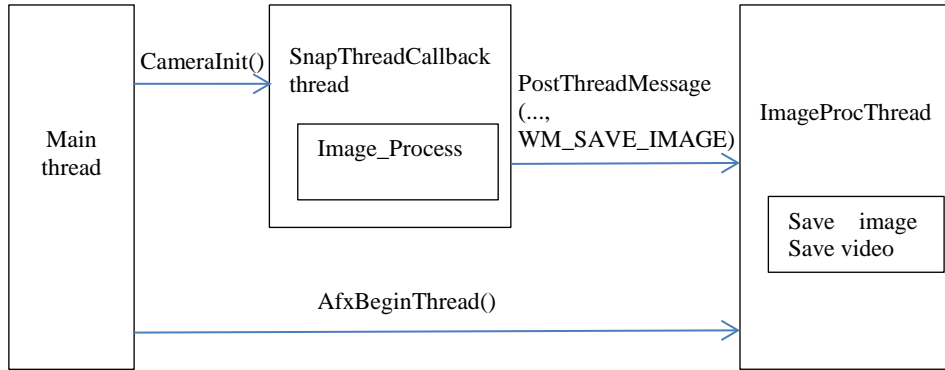


Figure 4. 17 The interaction of the three threads in the software

4.4.2 Image processing

The Image-Pro Plus 6.0 and Matlab are used to verify the feasibility of a vision-based displacement system. The IPP6.0 is used to obtain the displacement of markers from the captured image while the Matlab is used to analyze the displacement data or to execute the direct linear transformation (DLT) calibration algorithm. In addition to manual operation, IPP6.0 provides automate repetitive tasks and customize Image-Pro by the powerful macro language, IPBasic. It also supports high-level languages like Visual Basic and Visual C++. One can create his own programs to create custom user-interface, processing and I/O routines. The processing routine adopted in the experiment is illustrated below.

1. Preprocessing:

The preprocessing procedures of images are greatly variable in order to better identify the object and reduce the noise: they can be different combinations of

several enhancement algorithms and several filter algorithms as illustrated in Fig. 4.18.

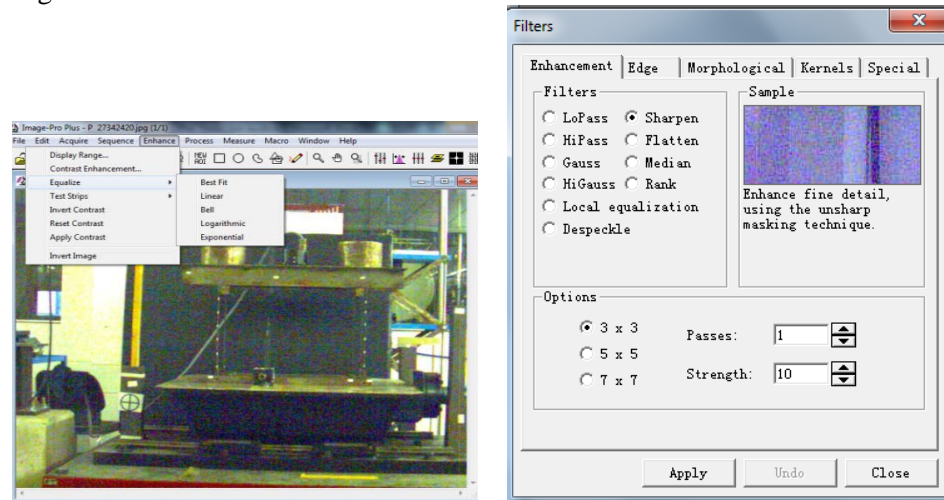


Figure 4. 18 Preprocessing of the image to refine the image quality

The calibration is another important part of the preprocessing in order to obtain correct coordinates for the markers. When one measures the displacement based on a vision system, the unit of displacement of the object is the pixel, which should be multiplied by scaling factors in order to obtain the real displacement. Assuming the size of the target is (L_x, L_y) which corresponds to $(x$ pixels, y pixels) on the image, the scaling factors (SF_x, SF_y) are calculated as:

$$SF_x = L_x / x, \quad SF_y = L_y / y \quad (4.31)$$

The scale factor for X/Y coordinates as well as the rotation angle and the aspect ratio of the image can be obtained by IPP6.0 (Figure 4.19). The calibrated unit will be applied to the followed measurement. Some advanced calibration algorithms, such as DLT, can be realized in Matlab.

For image/video taken from the skew direction, it is necessary to register the image to the reference image and to calibrate the projective distortion. It can be implemented by IPBasic code.

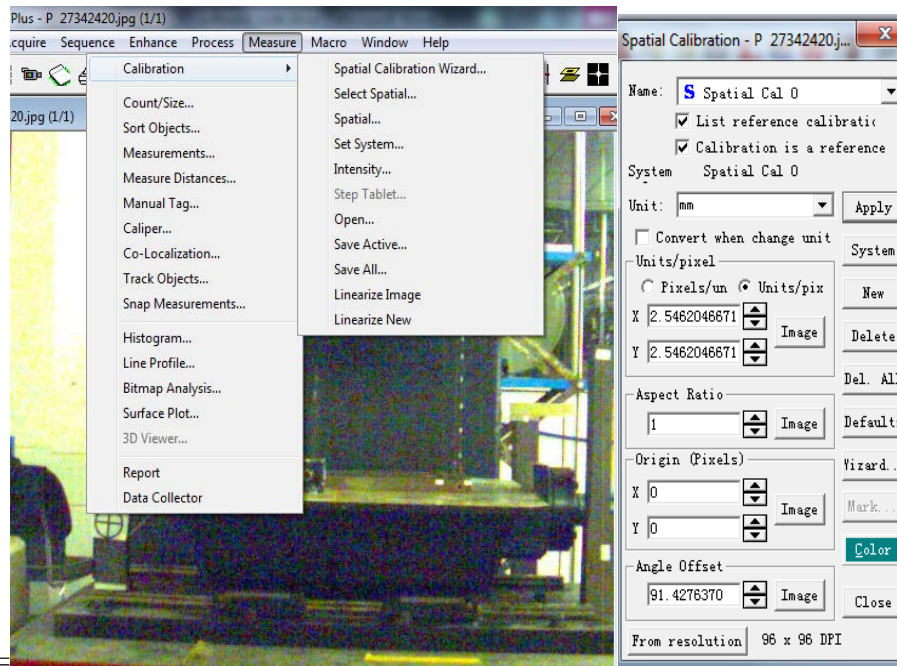


Figure 4. 19 Image calibration through IPP6.0

2. AOI selection and Object Segmentation

After having being preprocessed, some AOIs, which include the potential positions of the markers, are selected from the image to focus the next processing on the AOIs. The objects are then segmented from the image background by spatial tools: area, x coordinates, y coordinates or perimeter; or by segmentation tools that extract features by color/intensity value, as shown on Figure 4.20.

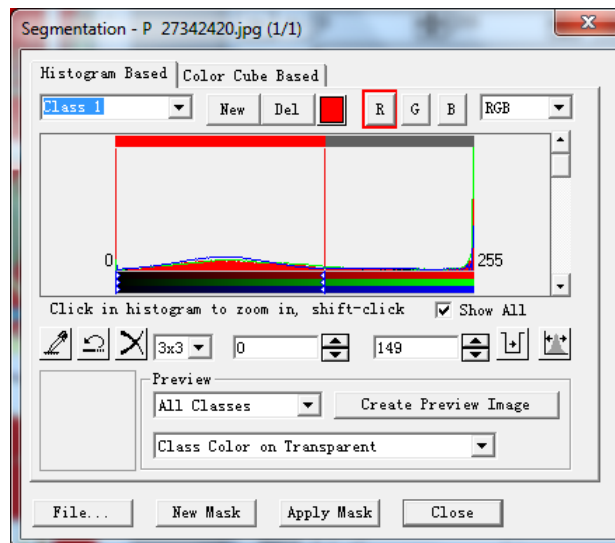


Figure 4. 20 Segmentation through a color intensity feature

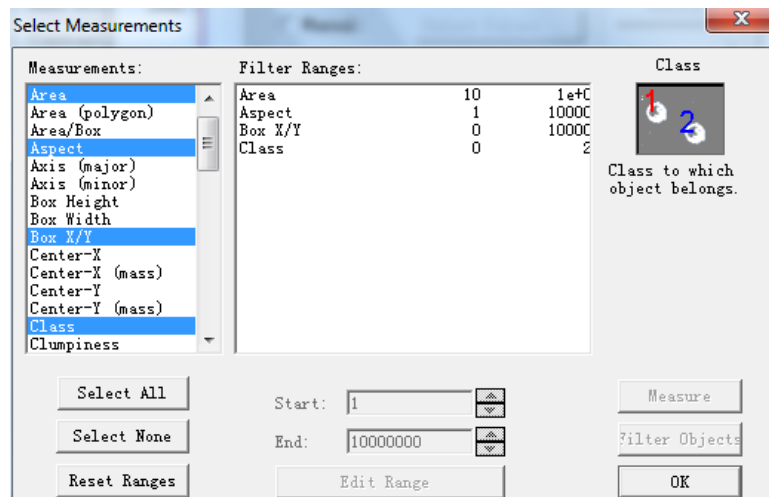
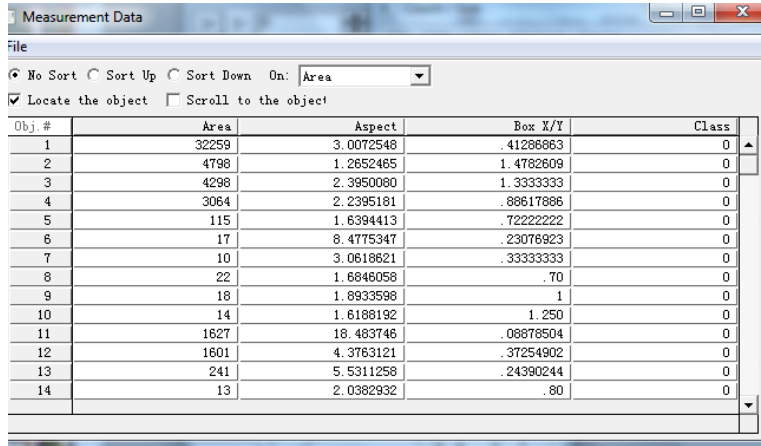


Figure 4. 21 Representation of potential objects

3. Representation and description

Apart from the objects of interest, there can be some other objects segmented from the background. Especially when one segments the image

through pixel intensity. Further effort should be addressed to better identify the object. Some attributes of potential objects are chosen to represent the object, such as area, angle, perimeter, diameter, roundness and aspect ratio. Objects are described according to the chosen representation (See Figure 4.21 and Figure 4.22).



Obj. #	Area	Aspect	Box X/Y	Class
1	32259	3.0072548	.41286883	0
2	4798	1.2652465	1.4782609	0
3	4298	2.3950080	1.3333333	0
4	3064	2.2395181	.88617886	0
5	115	1.6394413	.72222222	0
6	17	8.4775347	.23076923	0
7	10	3.0618621	.33333333	0
8	22	1.6846058	.70	0
9	18	1.6933598	1	0
10	14	1.6188192	1.250	0
11	1627	18.483746	.08878504	0
12	1601	4.3763121	.37254902	0
13	241	5.5311258	.24390244	0
14	13	2.0382932	.80	0

Figure 4. 22 Description of potential objects

4. Object recognition

After the potential objects have been described by the chosen representation attributes, some criteria can be applied to them to distinguish/classify the objects toward their recognition.

5. Reconstruction

The coordinates of recognized object are expressed in the unit of pixels, which also suffers from the distortion. Hence, the scale factor one obtains in the calibration step can be used to convert the unit. The DLT matrix obtained in calibration step can also be used to rectify the coordinates of objects.

6. Track object:

Applying the aforementioned steps to all the images in the video, one can track the motion of objects. Apart from this kind of tracking, IPP6.0 provides correlation tracking which can be used to track objects when

image segmentation is difficult or not possible. Correlation tracking uses Fourier cross-correlation to find the position of the object outlined by an AOI on the next frame of the sequence. (IPP6.0 help)

7. Export the results and analyze them.

The measurement results of IPP6.0, which include displacement and velocity, can be exported to an excel file for further analysis according to the pursued application.

4.5 Experimental validation

In this section, the results of some experiments carried out to assess the performance of the vision system are reported. In the first experiment, a camera, called SV642, is utilized to record the motion of a 3-stories frame which is mounted on a shaking table on the Lab. The obtained image sequence is processed by IPP6.0 to extract the motion of paper markers pasted on the frame. The results confirm the utility and the resolution of this system. Then another camera, SunTime FX30VC, is used to record the static and dynamic motion of a single-story frame, on which several paper markers and LED markers are placed. As before, this frame is mounted on the shaking table. The image sequence is also processed by IPP6.0 to obtain the static and dynamic performance of the vision system. Different exposure times and different camera orientations are utilized during the experiments. The density of markers will also be discussed.

4.5.1 Feasibility of a vision-based system for displacement measurement

The first experiment is carried out using the camera SV642 to assess the feasibility of a displacement measurement vision-based system. A three-stories frame is mounted on a shaking table which moves at the frequency of 2.4Hz, with the amplitude of 4mm. The dimension of each story is 60cm×30cm×3cm (Balzi, 2011). The first and third stories are braced. The optical axis of the SV642 camera is perpendicular to the front plane of the frame. During the experiment, 1242 frames are recorded (i.e., 10.3 sec.) at a sample rate 120 frames/second. Two white markers T1 and T2 are installed on the second story, while further two markers T3 and T4 are installed on the first story, as shown in Figure 4.23. The size of each story is 60cm×30cm×3cm. The horizontal coordinates of the left point of the first floor is 169 (pixel) while the one of the

right point is 525 (pixel). Hence, the horizontal scaled factor is 60cm /356 pixels, i.e., 1.685mm/ pixel.

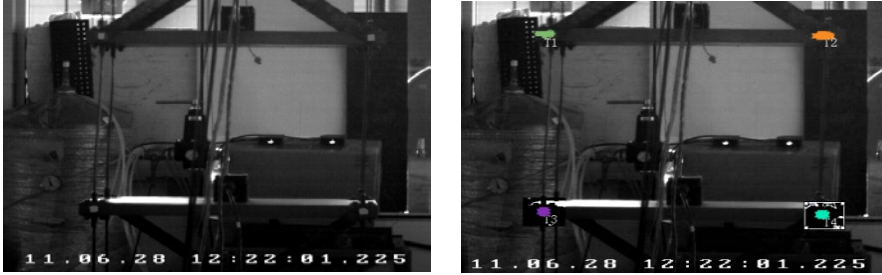


Figure 4. 23 Photographs accounting for the initial position at rest. On the right side 4 markers are outlined.

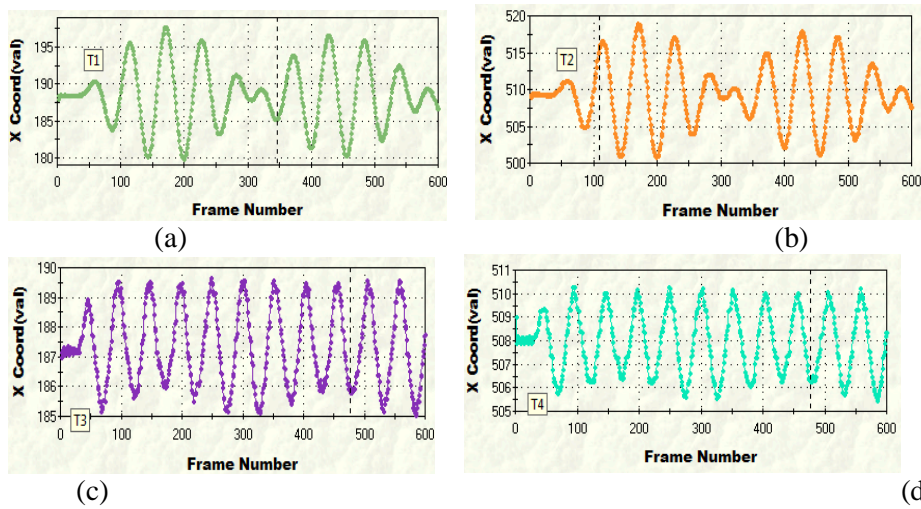


Figure 4. 24 The track of: (a) T1 (left-top); (b) T2 (right-top); (c) T3 (left-bottom); (d) T4 (Right-bottom); (The unit of x coordinate is the pixel)

The obtained horizontal displacements are shown in Figure 4.24. The resolution turns out to be 0.16mm (0.1 pixels). The movements of T1 and T2 are consistent each with the other, while the movements of T3 and T4 are consistent each with the other. They are quite similar to the shaking table sine wave since the stiffness of the first story is largely increased by the presence of the cross-brace. On the movement of T1 and T2, two mode frequencies can be distinguished: one is 2.4Hz (the excitation), the other is 0.41Hz (the system). If

one compares the movement between T2 and T4, a 180 degree phase difference can be discovered, as one can see from Figure 4.23. Focus now the attention on the movement of T1 (Figure 4.25): one obtains for the maximum displacement of T1 the value 16.85mm (10 pixels) and the instant when the maximum shift occurred: it corresponds to the digital image n°175 which is shown in Figure 4.26.

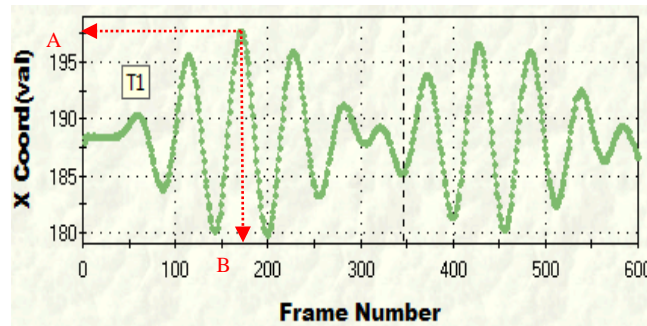


Figure 4. 25 The maximum displacement of T1

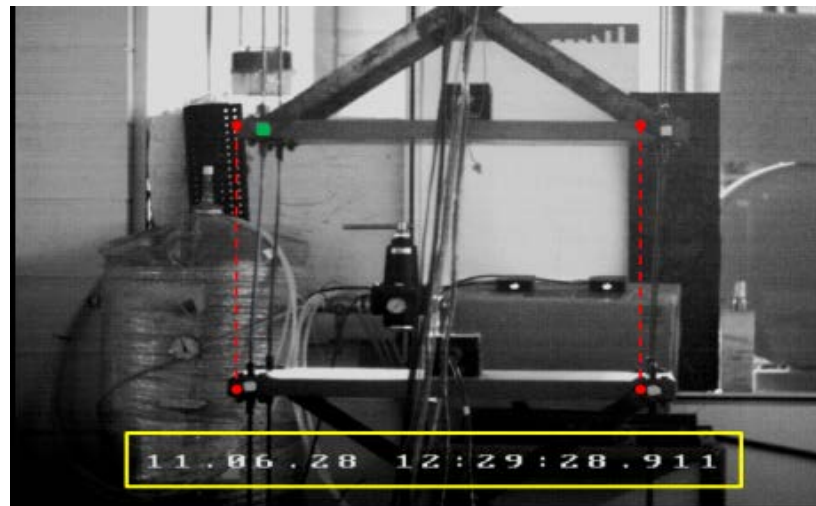


Figure 4. 26 The instant when maximum shift occurred

The vertical direction displacements are shown on Figure 4.27 and Figure 4.28. The vertical displacement of T3 and T4 is similar and is nearly 0 due to the fixing cross-brace. But the vertical displacement of T1 and T2 cannot be

ignored. Its peak-peak amplitude is around 0.7 pixels and corresponds to 1.18mm. One can also distinguish two frequencies from Figure 4.27: 4.8Hz and 0.41Hz. The first vertical frequency is twice the first horizontal frequency which confirms it is caused by the translation motion. This can also be corroborated by that the vertical displacements of T1 and T2 are in phase.

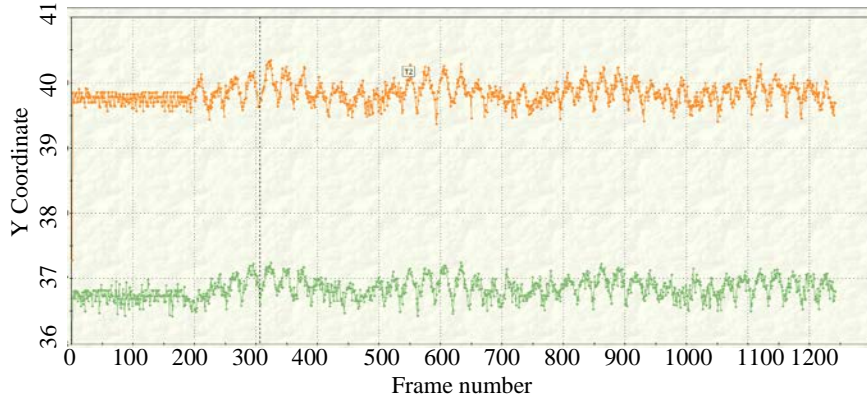


Figure 4. 27 The vertical displacements of T1 and T2

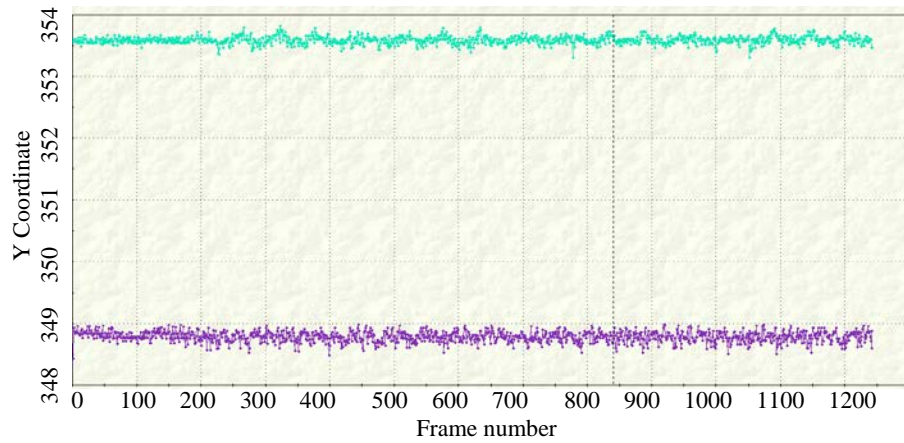


Figure 4. 28 The vertical displacements of T3 and T4

4.5.2 Performance of a vision-based displacement measurement system

4.5.2.1 Static experiments

As introduced in section 4.2, there are projective distortion and optical distortions in the images captured by a camera. However, generally these distortions are not taken into account and an equal scale factor, which is calculated according to a known size object, is normally applied to convert the image coordinates to space coordinates. In this work, the performance of improved methodology, the DLT, is examined. A sheet of paper with 110 evenly distributed points on it is utilized as the calibration board, as shown in Figure 4.29. Let the coordinates of the up-left point be $(0, 0)$ and the row distance is 14.83mm while the column distance is 22mm. Two groups of points are utilized as reference points: the four markers of circle are utilized for interpolation calibration while the four markers of rectangle are for extrapolation calibration.

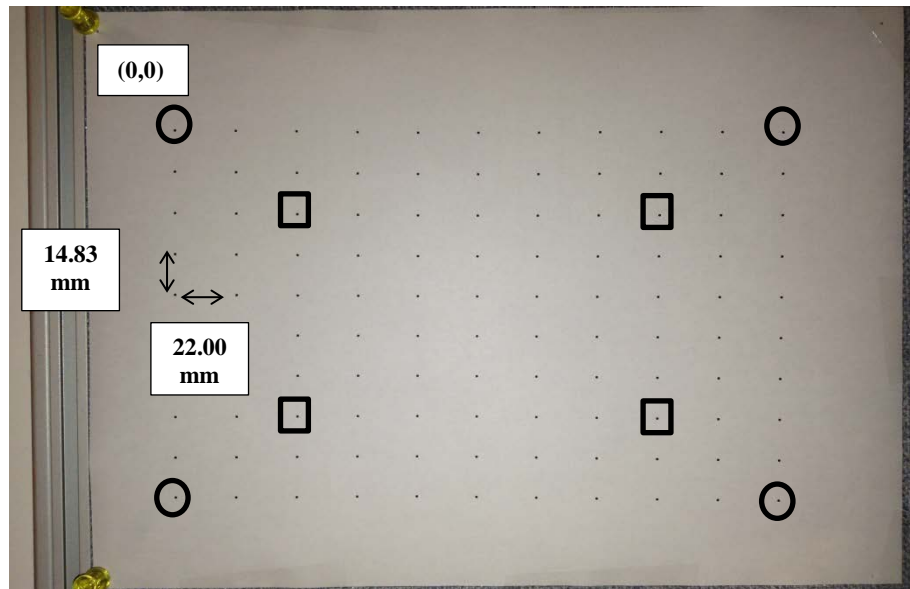


Figure 4. 29 the calibration board

The performance of the two calibration methodologies are first examined when the optical of camera is approximately perpendicular to the image. In Figure 4.30, the two groups of points are utilized for interpolation scale factor calibration and extrapolation scale factor calibration. After having acquired the scale factors of both horizontal and vertical directions, the space coordinates of the 110 points are recalculated. The distance between the calculated coordinates and the original coordinates is denoted as the calibration error of a point. One can see that the performance of interpolation is better since it cover all the area of interested.

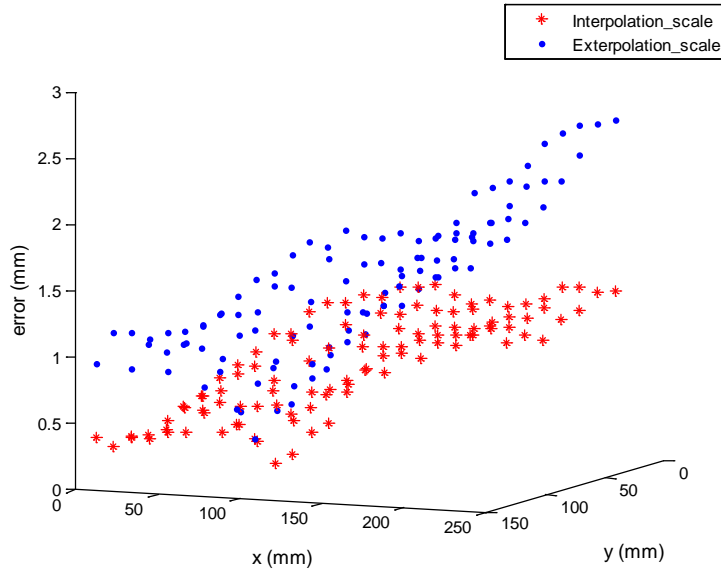


Figure 4. 30 The calibration of interpolation and extrapolation calibration based on the scale factor approach when the optical of camera is perpendicular to the image

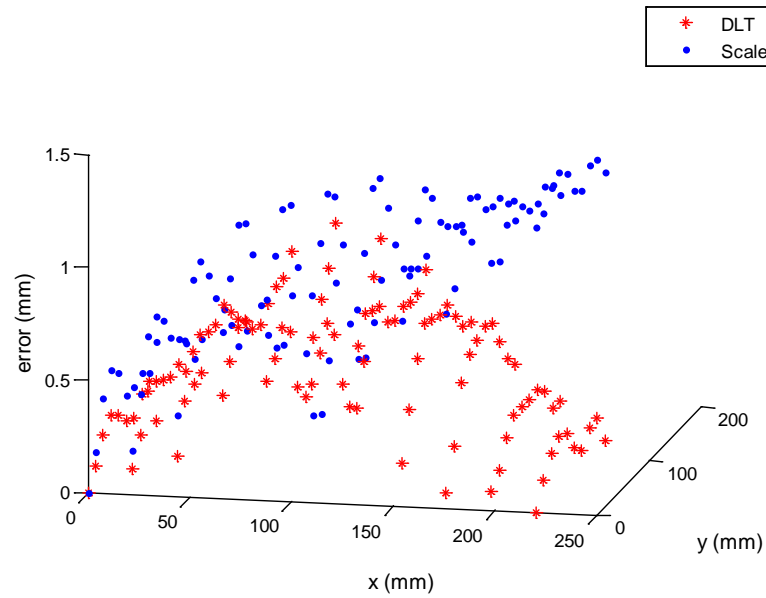


Figure 4. 31 The calibration error of interpolation scale factor and interpolation DLT calibration when the optical of camera is perpendicular to the image

Figure 4.31 shows the performance of the interpolation scale factor approach and the DLT approach when the optical of camera is perpendicular to the image. One can see that the DLT shows a better performance than the one of the former approach. This better accuracy becomes obvious when the optical axis of the camera is skewed with the image at a small angle and a larger angle, as illustrated in Figure 4.32 and Figure 4.33. In each figure, (a) is the captured image; (b) is the comparison between the performance of the interpolation and extrapolation calibrations based on the scale factor approaches; (c) is the comparison between the performance of the interpolation calibration based on the scale factor approach and the DLT approach. One can see from those two figures that as the skewed angle increases, the advantage of DLT method is more obvious while the accuracy of the scale factor method decreases aggressively. Another interesting result which can be observed is that, differently from the result shown on Figure 4.30, the performance of the extrapolation scale factor method is better than interpolation scale factor method in the skewed situation. This can be explained by the fact that the image coordinates of four outmost points are greatly distorted since their depth of fields are greatly different.

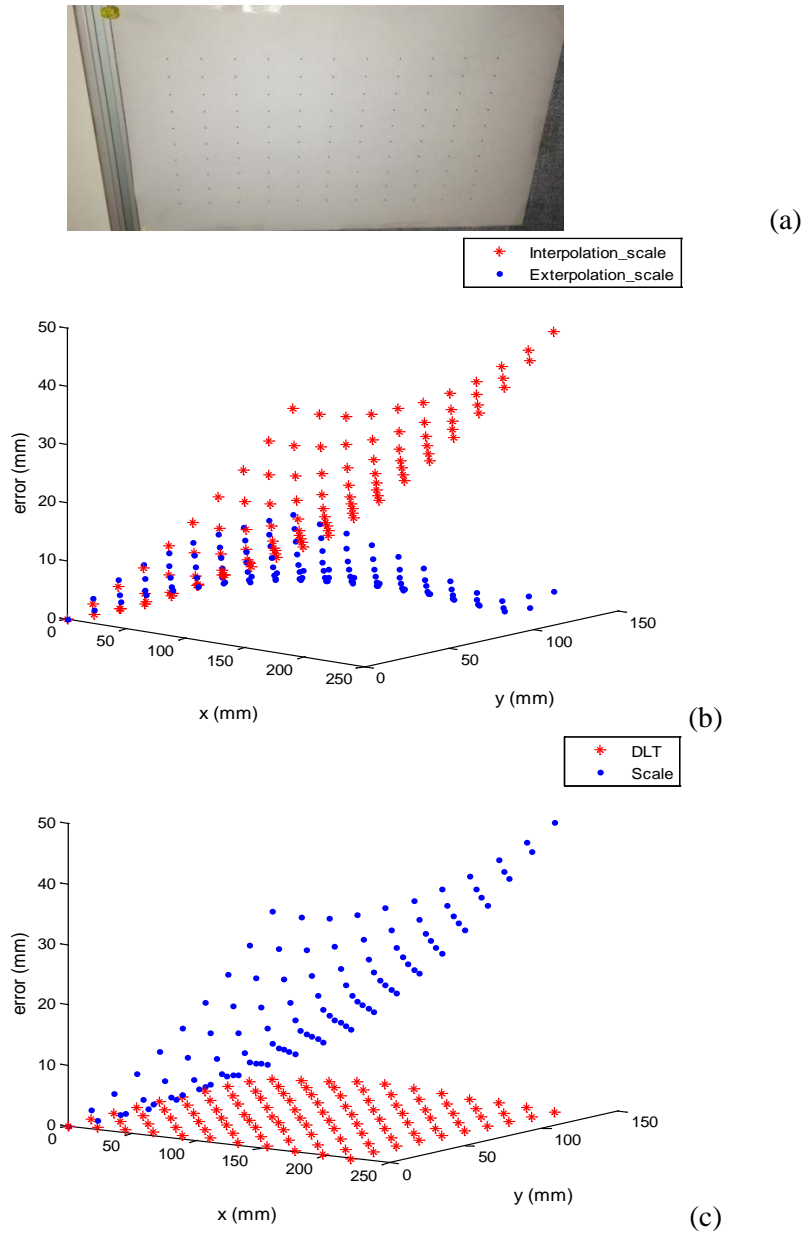


Figure 4. 32 Calibration results when the optical axis of camera is skewed with the image at a small angle

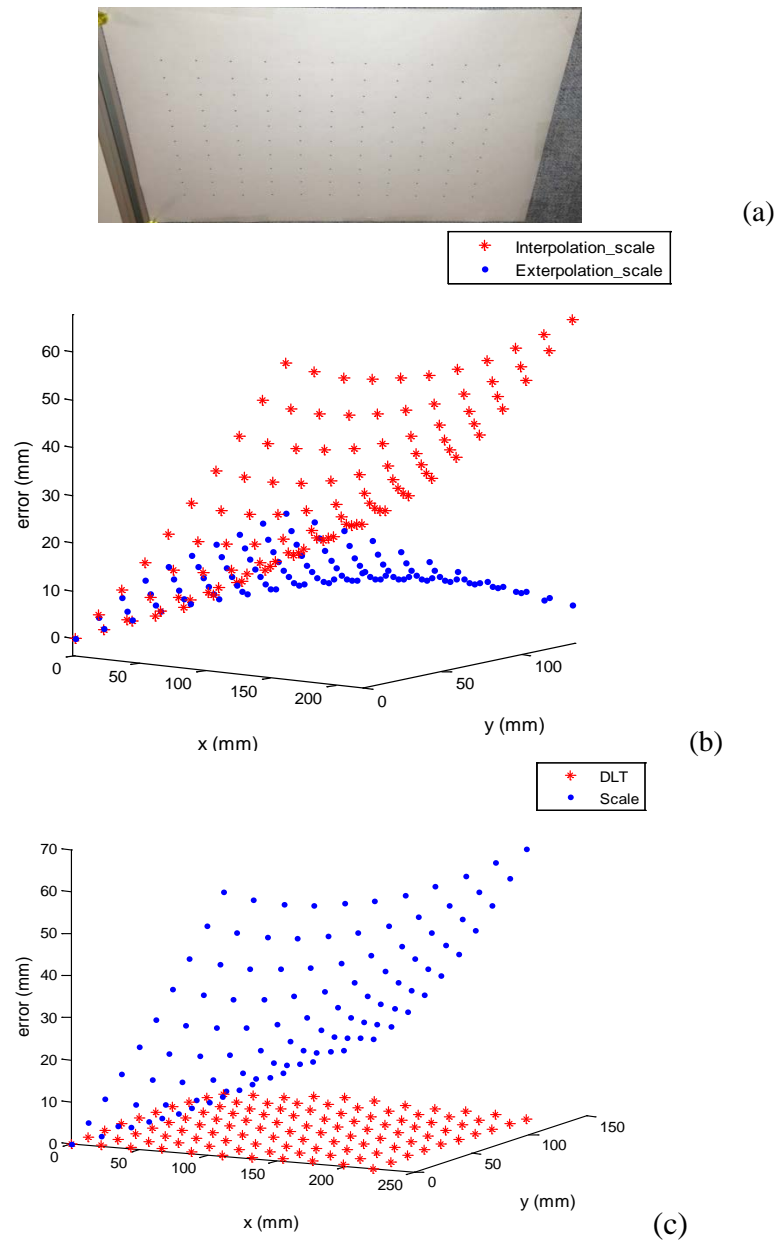


Figure 4. 33 Calibration results when the optical axis of the camera is skewed with the image at a large angle

To make clear the performance of DLT for different skewed angle, the performance of DLT under both situations are plotted in Figure 4.34. Comparing with the performance of the scale factor method, only a slightly deterioration is observed which shows that DLT provides a good accuracy for different skew angles.

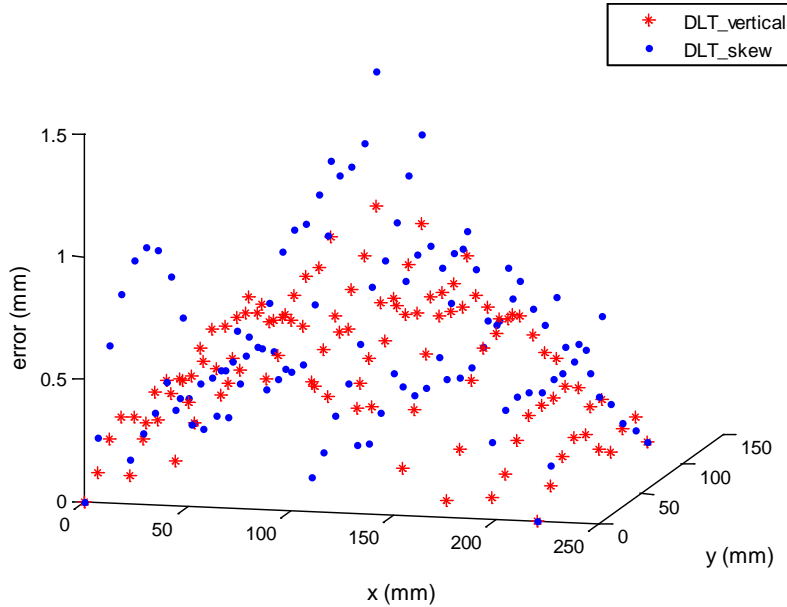


Figure 4. 34 Performance of DLT under two skewed situations

4.5.2.2 Dynamic experiment

In this part, another camera, the Suntime FX30, is employed to monitor the in-plane motion of a single-story frame on which dense markers are placed. This frame is mounted on a shaking table. The size of the bottom plate of the frame is 60cm×30cm×3cm, the size of the column is 38cm×3cm×0.3cm. Two 21kg masses are put on the girder. Several experiments are executed to access the static and dynamic performance of this vision system.

4.5.2.2.1 Markers density and exposure period

The limitation on marker density and the influence of different exposure periods are discussed below.

A vision-based system allows one to place dense markers on the monitored structure. The motion of each marker is tracked by finding the position of the object in all images. It will be highly time-consuming if the marker is searched inside the whole image. An alternative way is to assign an area of interest (AOI) for each marker to be searched in a new image according to its current position and adopted motion prediction model. The new AOI of a marker (T1) must be able to cover its potential position at next frame and if there is another marker (T2) coming into the AOI of T1, misjudgment will be introduced: this limits the density of the markers.

In IPP6.0, the new AOI of an object is configured through a macro, *IpTrackMeasSet*, which sets various tracking parameters. One can use this macro command according to syntax:

IpTrackMeasSet(*sCommand*, *lOpt*, *dParam*)

Table 4. 5 Portion of the commands of the macro *IpTrackMeasSet*

Command	IOpt	dParam	Description
TM_TRACK_PREDICTION	Not used, should be 0	Value	Sets the tracking prediction depth
TM_MOTION_TYPE	Not used, should be 0	Value 0 = Chaotic 1 = Directional 2 = Straight	Sets the predominant motion type for the objects
TM_SEARCH_RADIUS	Not used, should be 0	Value in pixels	Sets the search radius (velocity limit) for automatic tracking
TM_ACCEL_LIMIT	Not used, should be 0	Value in pixels	Sets the acceleration limit for automatic tracking

The parameters of macro *IpTrackMeasSet* are illustrated in Table 4.5. As one can see, tracking prediction depth, the predominant motion type for the objects (Chaotic, Directional or Straight), search radius (velocity limit) and acceleration

limit can be set through this macro. In IPP6.0, this parameters can also been configured through a Graph User Interface (GUI) illustrated in Figure 4.35.

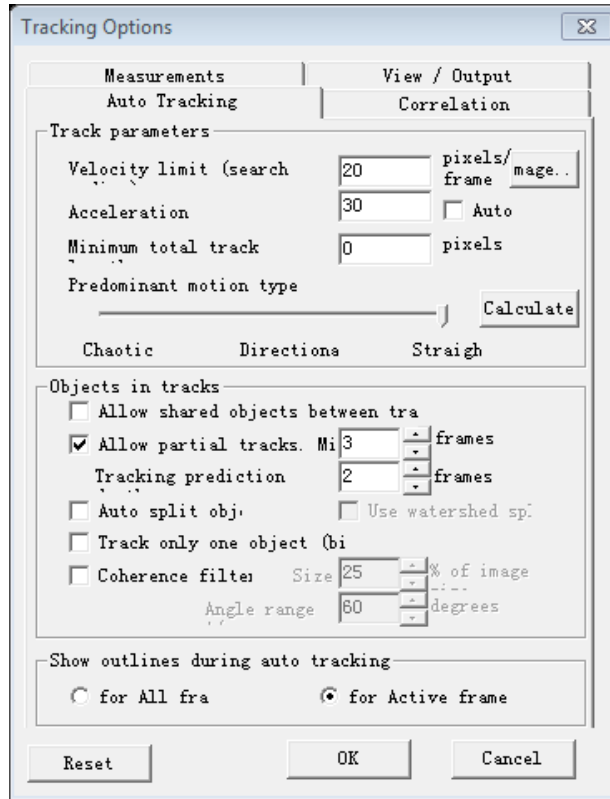


Figure 4. 35 The GUI for configuring the tracking options

Hence, the directional density of markers is constrained by the corresponding directional motion. In this experiment, the structure moves mainly on the horizontal direction. Hence, along the vertical direction, the density of markers can be relatively high provided that the light intensity contrast between the markers and the background is good enough. However, in the horizontal direction, if the horizontal distance between two markers is smaller than the predicted horizontal displacement, it is possible to misjudge the markers. As illustrated in Figure 4.36, the motions of two markers, T1 and T2, between whom the distance is about 4cm, are tracked. But the displacement of the

horizontal motion is around 10cm. Hence, the markers are placed too densely and this causes misjudgment, as Figure 4.37 illustrates.

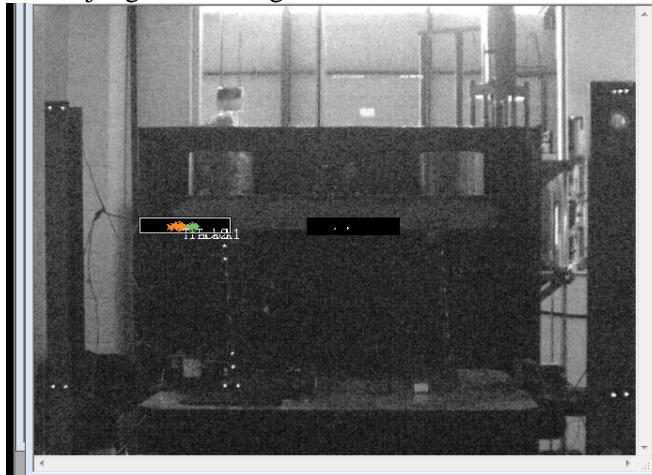


Figure 4. 36 Two markers too close each to the other

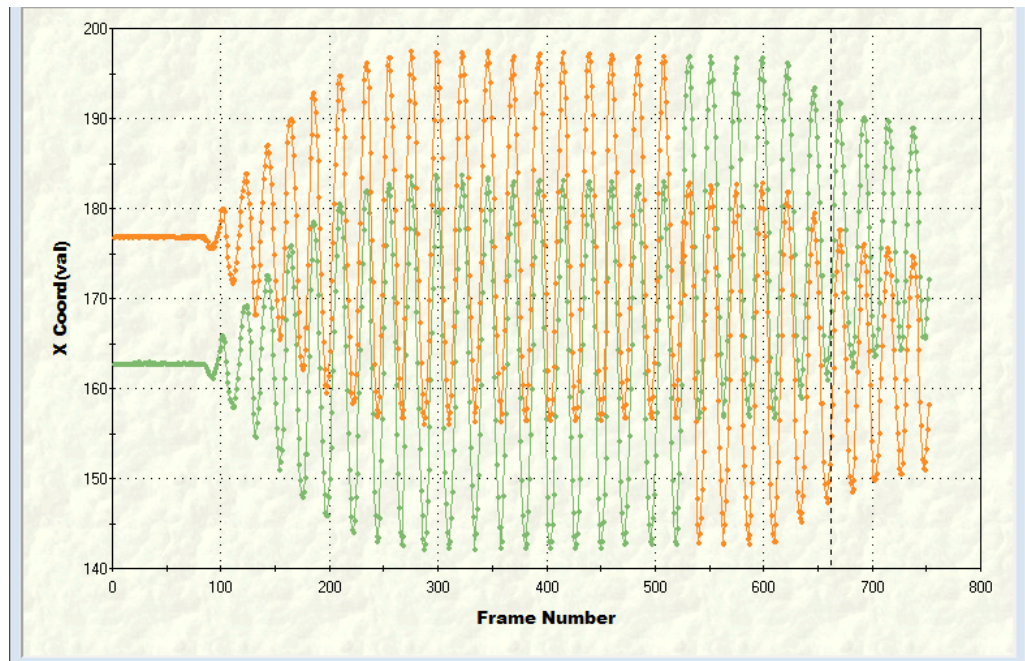


Figure 4. 37 Misjudgment for the two markers in Fig.4.36

The effect of different exposure periods is now discussed. Different exposure periods are used to record the motion of markers when the input of the shaking table is a sinusoid signal with 3mm amplitude at 2.6Hz, which is close to the natural frequency of the frame and therefore the resonance occurs. The motions of two markers are considered: one is fixed on the top of the left column and the other one is glued on the bottom of the frame, as shown in Figure 4.38. The scale factor is about 2.33mm/pixel. The experiment is carried out when the exposure period is 15ms. From Figure 4.39, one can see that the fuzziness of target when the frame is at the middle position is larger than the one when the frame is at the leftmost position.

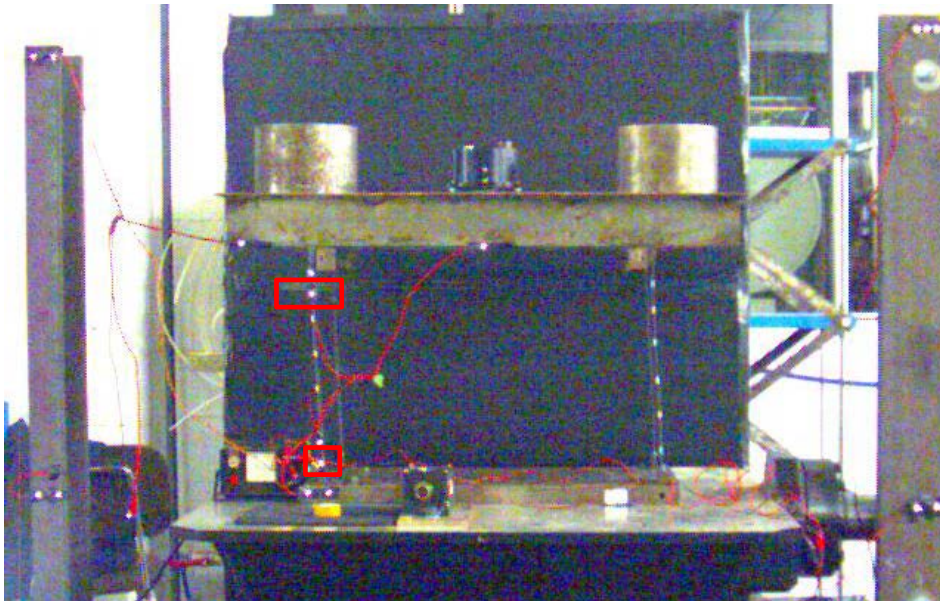


Figure 4. 38 The markers tracked to examine the affection of different exposure times

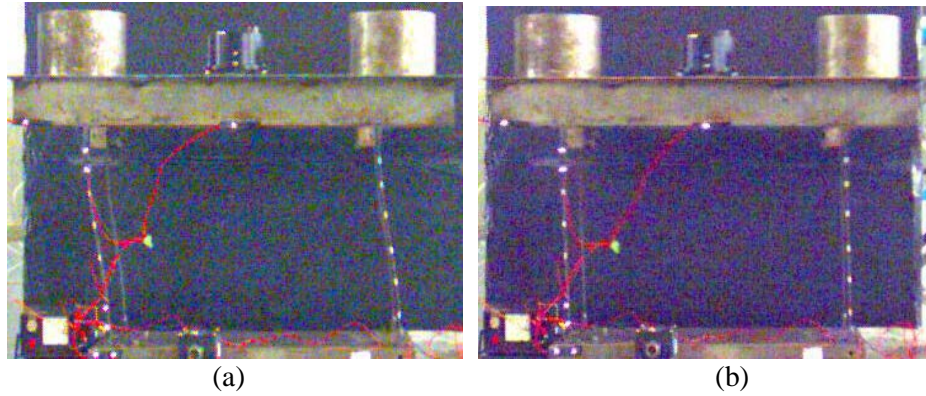


Figure 4. 39 The observed fuzziness of the uppermost marker on the left column
(a) the minimum fuzziness whose area is 15 pixels; (b) the maximum fuzziness
whose area is 21 pixels

Assuming the motion of a marker is as in Equation (4.31), where D is the displacement, A is the amplitude of the marker and f is the vibration frequency:

$$D = A \sin(2\pi f t) \quad (4.31)$$

The maximum velocity V_{\max} is written as in Equation (4.32):

$$V_{\max} = 2\pi f A \cos(2\pi f t) \quad (4.32)$$

Hence, the maximum fuzziness F_{\max} , which will be introduced, is approximated by Equation (4.33)

$$F_{\max} = T_{\exp} \times V_{\max} = 2\pi f A T_{\exp} \quad (4.33)$$

Where T_{\exp} is the camera exposure period. This is illustrated in Figure 4.40.

Hence, the exposure period causes the size of the markers to change from frame to frame and this introduces errors which will become significant when the exposure period is large. In addition, it is important to have a criterion to define the region of the markers, as addressed in the work of Wahbeh (Wahbeh, Caffrey et al. 2004).

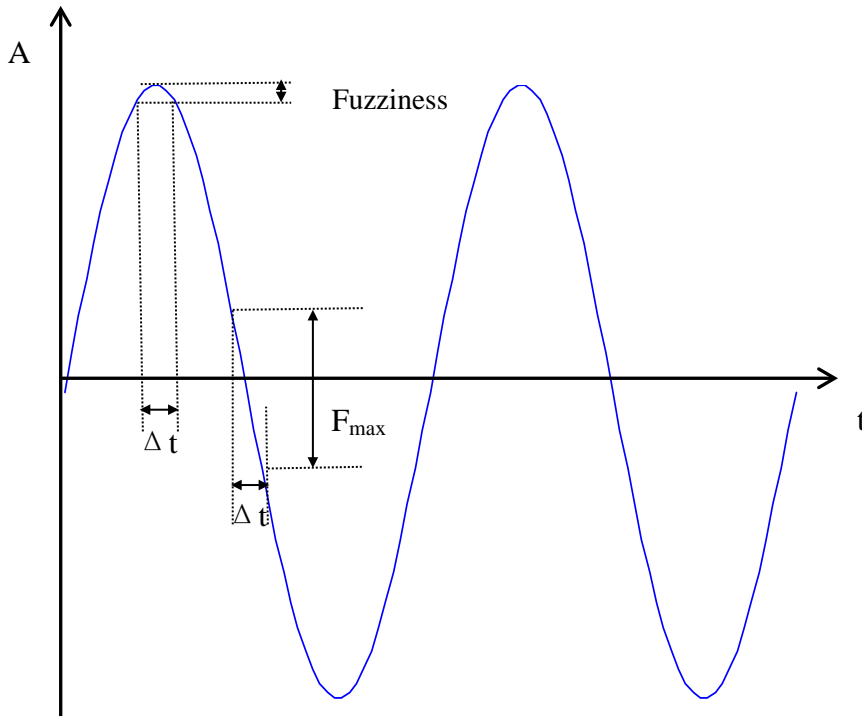


Figure 4. 40 The fuzziness introduced during exposure period when recording the motion

4.5.2.2.2 Registration

The registration is now focused on. As one can see from Figure 4.41, three white markers, T4-T6, are evenly placed on the top floor while another three markers, T1-T3, are placed on the bottom floor on which one markers is far away from the other two. Six markers are glued to each column: T7-T12 on the left one while T13-T18 on the right one. Other markers, as reference markers, are fixed on the coplanar stationary objects around the frame. The camera is located at a distance of 3.1m from the plane of interest and the video is recorded at a frequency of 60Hz. The shaking table moves at an amplitude of 10mm at the frequency of 0.5Hz, 0.75Hz, 1.25Hz and 1.5Hz. Each experiment lasts about 10s. Videos are taken from different orientations in order to verify the effect of image registration. The true color RGB models (True color RGB

means to represent and store graphical-image information in a 24-bit color space: (Red, Green, Blue)) are used to capture images/videos. According to the scale factor equation, the scale factor is calculated to be about 2.54mm/pixels.

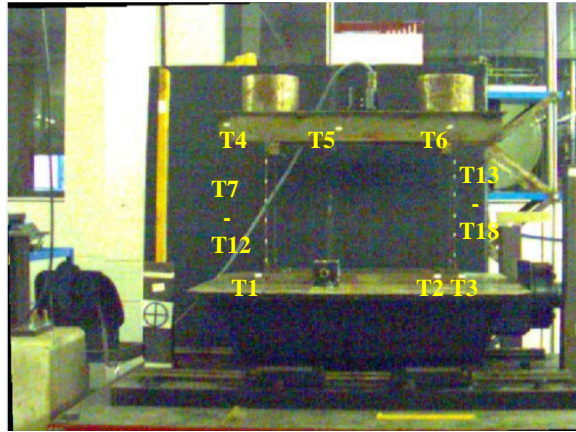


Figure 4.41 The markers adhered on the frame

On the first experiment, the frequency of the shaking table is 0.5Hz. The displacements of T1-T3, which are supposed to be sinusoid signals, are shown in Figure 4.42. Their spectra are shown in Figure 4.43. As one can see, the amplitude is slightly larger as a result of the following factors: 1) The intensity contrast between the markers and the background is not large enough which could be improved by adopting LED lights as markers. 2) To imitate the illumination condition of an in situ experiment, the fluorescent lamp in the lab, whose frequency is at 50Hz, is used. This oscillatory illumination condition deteriorates the performance of camera which captures images at a frequency of 60Hz. 3) The true color RGB image will be converted to grayscale intensity image before being processed by eliminating the hue and saturation information while retaining the luminance. The automatic white balance employed during the video capture will decrease the contrast between the markers and the background. 4) In this case, the scale factor is calculated by the length of the plate on the first floor, and its pixel coordinates which is judged by manual operation. Errors introduced since the fuzziness of the edge of the plate due to the aforementioned reasons, and the error is aggravated by the low-contrast between the frame and the background. This error can be decreased by using the size of an object which has a good contrast edge to calculate the scale factor. 5)

The error introduced by scale factor approach. Figure 4.44 and Figure 4.45 provides the displacements and the spectra of T4-T6, respectively. One can see that there are two frequencies on the displacement from T4-T6 and the waveforms from these markers are consistent.

Figure 4.46 and Figure 4.47 are the displacements (and their spectra) of the markers glued to the left column while Figure 4.48 and Figure 4.49 are the displacements (and their spectra) of the markers on the right column. One can see that all these displacements have the 0.5Hz signal component while only some of them have the harmonic frequency component: The closer to the upper floor, the harmonic component becomes more evident. This is consistent with the expected response and confirms the successful tracking of the markers.

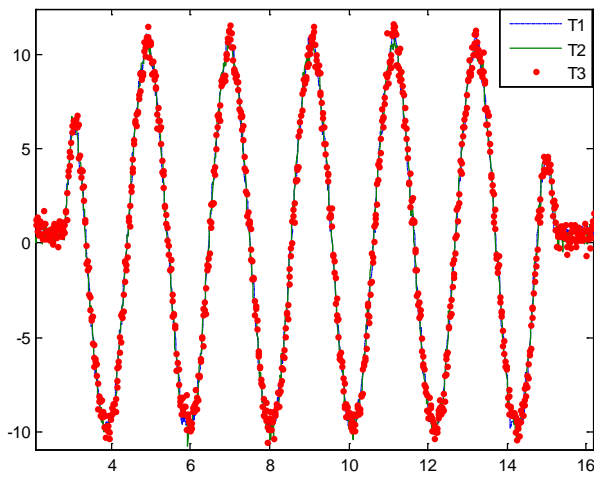


Figure 4. 42 Displacement of the markers on the bottom floor (perpendicular)

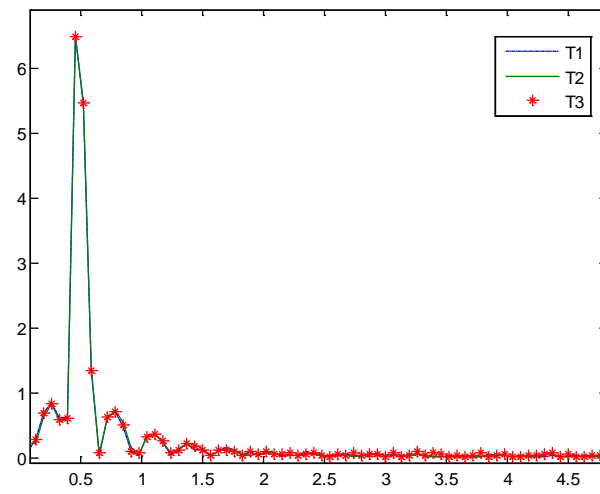


Figure 4. 43 Spectra of the signal recorded for the markers on the bottom floor (perpendicular)

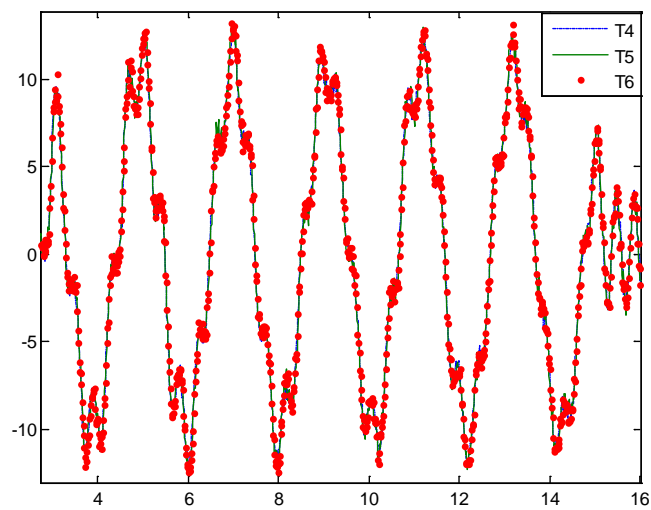


Figure 4. 44 Displacement of the markers on the top floor (unit: mm VS Seconds) (perpendicular)

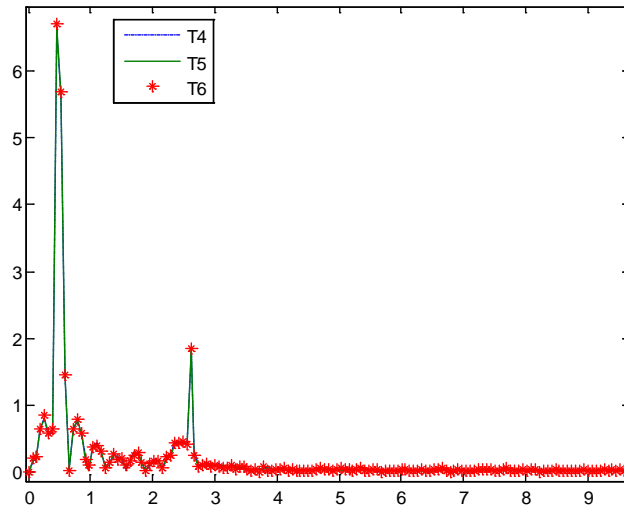


Figure 4. 45 Spectra of the signal recorded for the markers on the top floor (perpendicular)

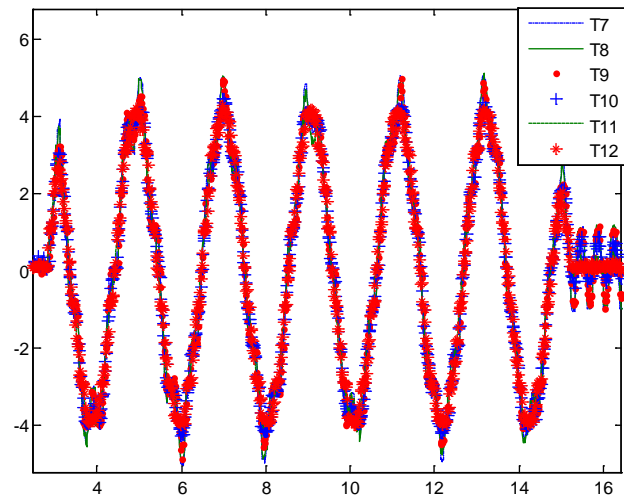


Figure 4. 46 Displacements of the markers on the left column (perpendicular)

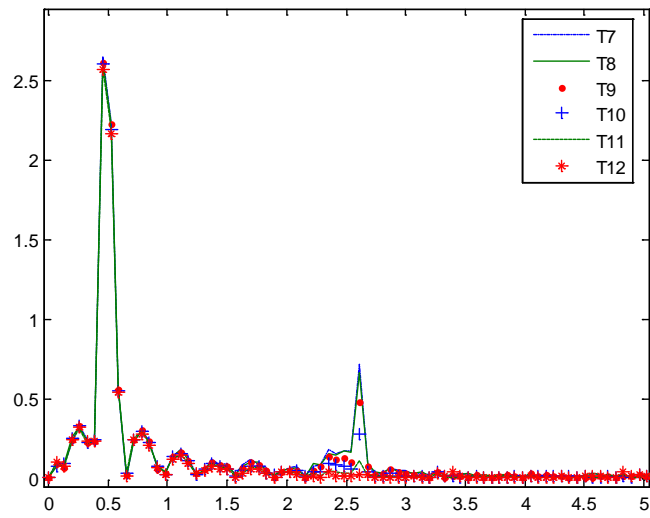


Figure 4. 47 Spectra of the signal recorded for the markers on the left column (perpendicular)

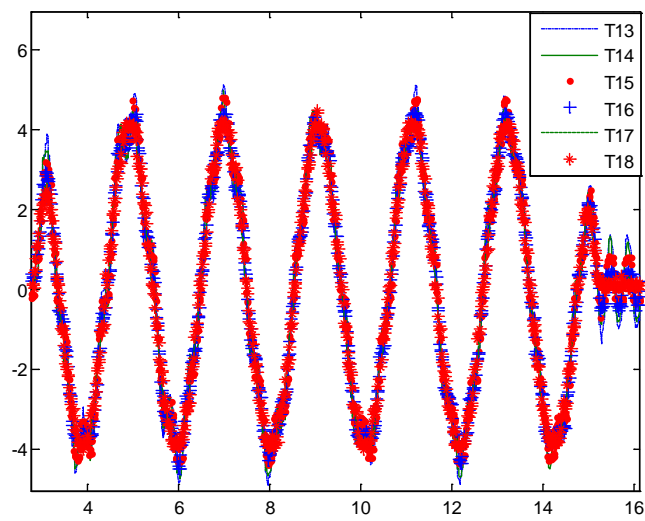


Figure 4. 48 Displacement of the markers on the left column (perpendicular)

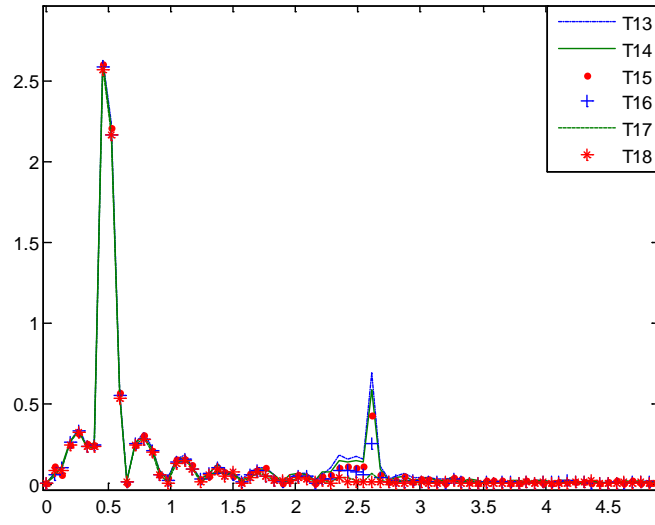


Figure 4. 49 Spectra of the signal recorded for markers on the left column (perpendicular)

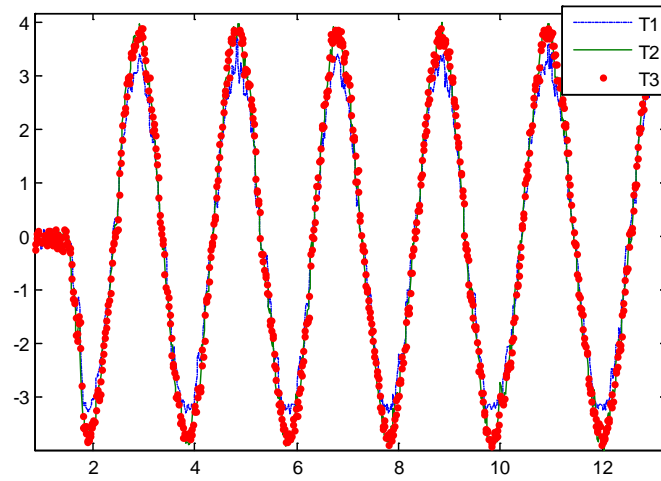


Figure 4. 50 The displacement of markers on the bottom (skewed)

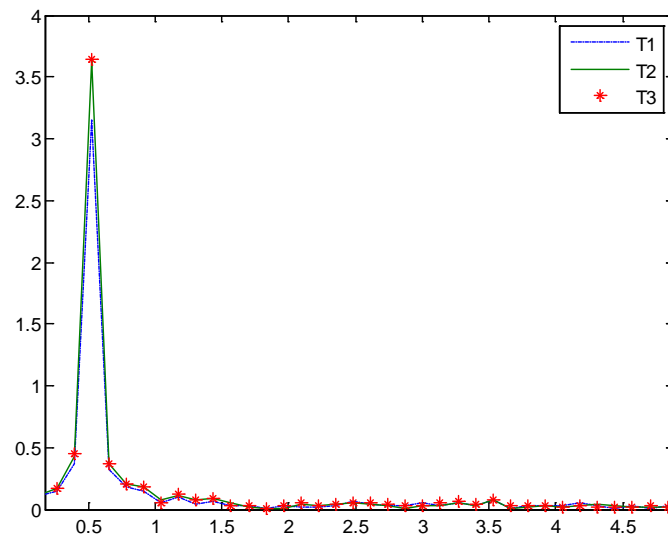


Figure 4. 51 Spectra of the signals recorded for the markers on the bottom (skewed)

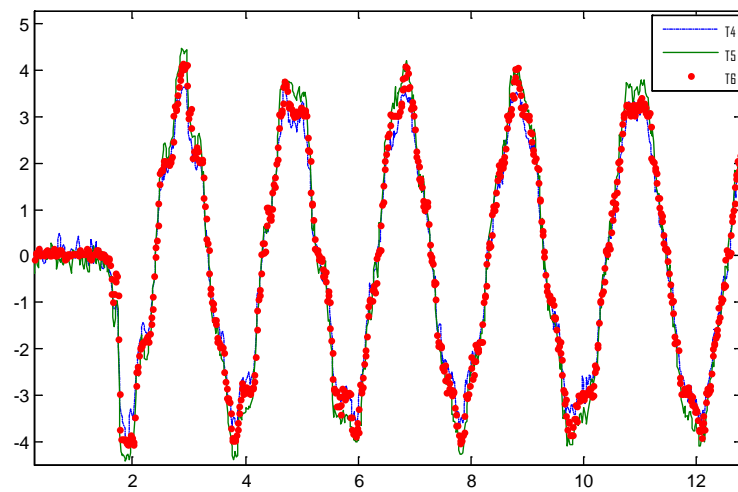


Figure 4. 52 The displacement of markers on the top (skewed)

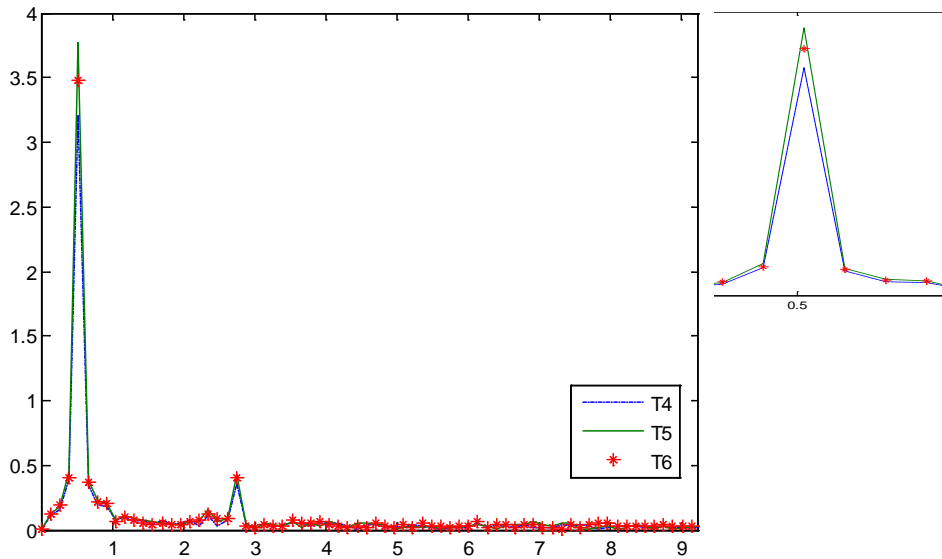


Figure 4.53 Spectra of the signals recorded for the markers on the top (skewed)

The second video is taken when the orientation of the camera optical axis is about 22 degree skew from the normal of the interested plane. In this case, the markers are not of the same depth of field and different scale factors apply. Four reference markers are utilized to register the skewed image with the reference image. Figure from 4.50 to 4.55 show the results obtained before registration. From the displacement of T1-T3, one can see that the waveforms of T2 and T3 are very close since they are placed closely, while the waveform of T3 is much smaller since it is placed far away from the camera. This is confirmed by the waveform of T4-T6 which is placed on the top floor and the amplitude differences of their displacement waveform are more equal. The waveforms of markers glued to the left column are shown on Figure 4.42 and Figure 4.43. Since these markers are almost at the same depth of field, not obvious difference can be seen from their waveforms.

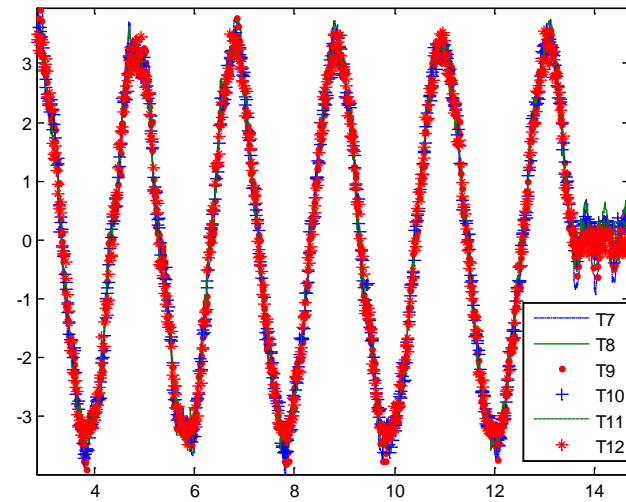


Figure 4. 54 The displacement of markers on the left column (skewed)

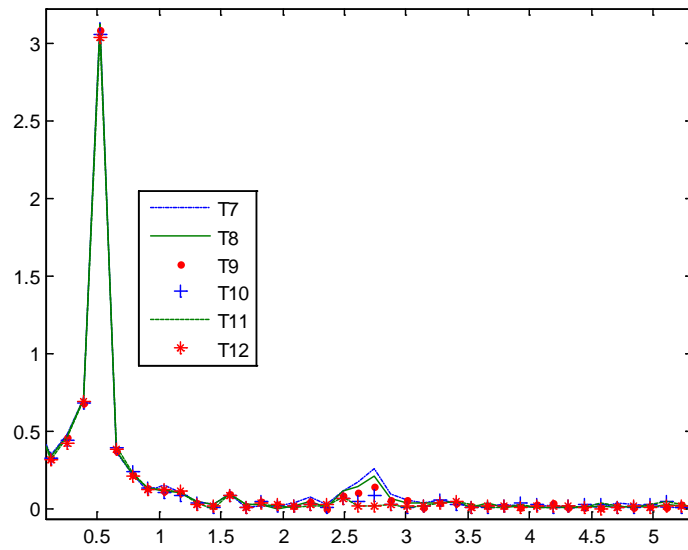


Figure 4. 55 The spectra of signals of markers on the left column (skewed)

Four reference markers are now used to register the skewed video to the reference video by using a projective affine transformation. Figure 4.56 shows the image before and after registration. Figure 4.57 and Figure 4.58 illustrate the waveform of T4-T6 obtained after registration. One can see that the amplitudes of those three markers are equal after registration. This confirms the good performance of registration. According to the spectra, the amplitude of the harmonic component is slightly distorted after registration which could be caused by the fuzziness introduced by the registration procedure which is equivalent to a filter in the frequency domain. At the same time, the positions of the reference markers are not optimal since both the right markers are located at a level lower than the top floor.

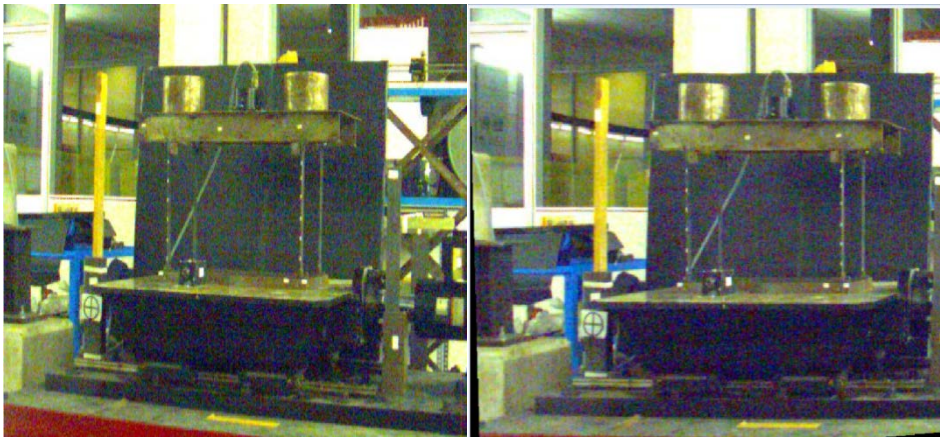


Figure 4. 56 Image before and after registration

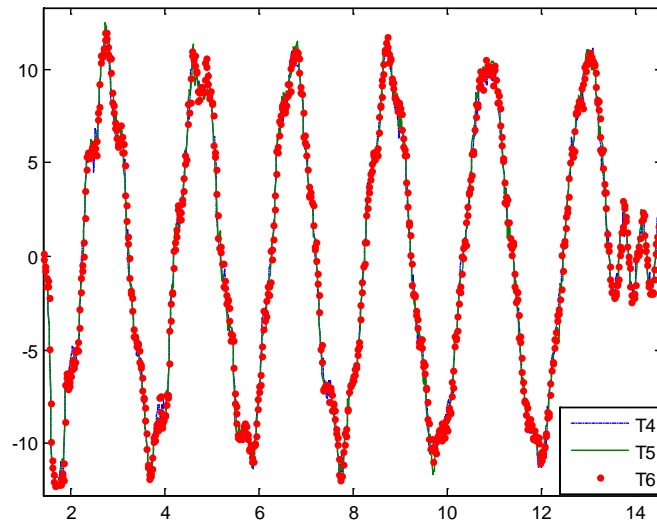


Figure 4. 57 The displacement of markers on the top floor (After registration)

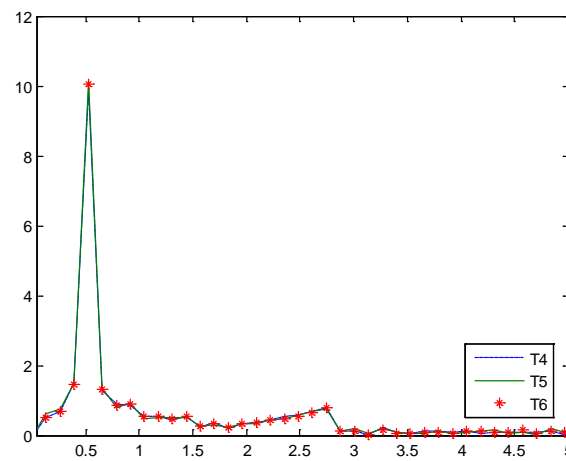


Figure 4. 58 Spectra of the displacement signal of the markers on the top floor
(After registration)

4.5.2.2.3 2D DLT

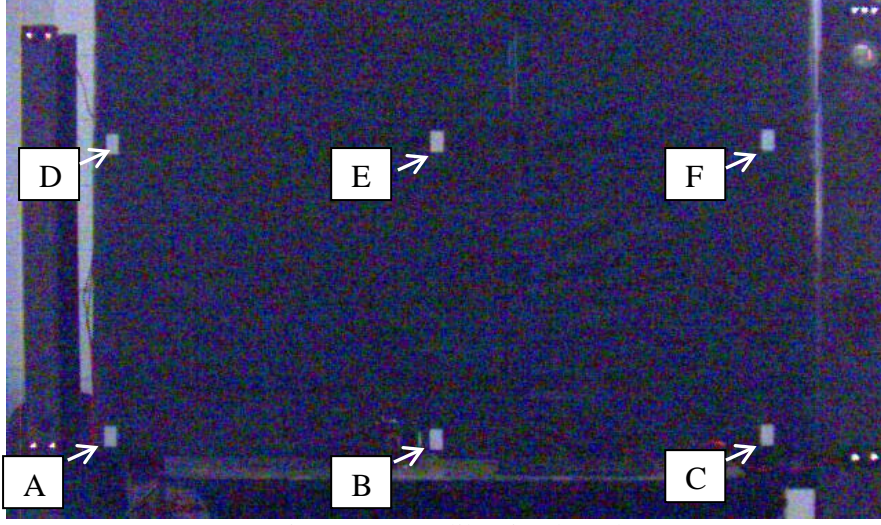


Figure 4.59 calibration board

As introduced in section 4.2, an alternative methodology to eliminate the projective and optical distortions is DLT. According to the result from subsection 4.5.2.1, due to DLT method, the optical axis of the camera have not to be perpendicular to the motion plane supposing the space coordinates of at least four points is known. Through those four known-position points, one can obtain the DLT transformation matrix and then reconstruct the space coordinates of any image points from its image coordinates.

Before carrying out the dynamic experiment, a calibration board with six known positions markers, as illustrated in Figure 4.59, is adopted. The coordinates of points A-F are stated Table 4.6. The scale factor is about 2.34mm/ pixel. Since the points are coplane, their homogeneous coordinates are written as $(X, Y, 1)$ and $(x, y, 1)$. Then

$$\begin{pmatrix} X \\ Y \\ 1 \end{pmatrix} = \mathbf{H} \begin{pmatrix} x \\ y \\ 1 \end{pmatrix} \quad (4.34)$$

Table 4. 6 Coordinates of the points A-F

	A	B	C	D	E	F
Space X coordinates (mm)	20	570	1120	20	570	1120
Space Y coordinates (mm)	20	20	20	510	510	510
Image x coordinates (pixels)	71	307	547	73	307	548
Image y coordinates (pixels)	407	409	406	195	193	192

DLT is performed and the transformation matrix \mathbf{H} is obtained as below:

$$\mathbf{H} = \begin{bmatrix} 0.0024 & 0.0000 & -0.1586 \\ 0.0000 & -0.0024 & 0.9873 \\ 0.0000 & 0.0000 & 0.0010 \end{bmatrix} \quad (4.35)$$

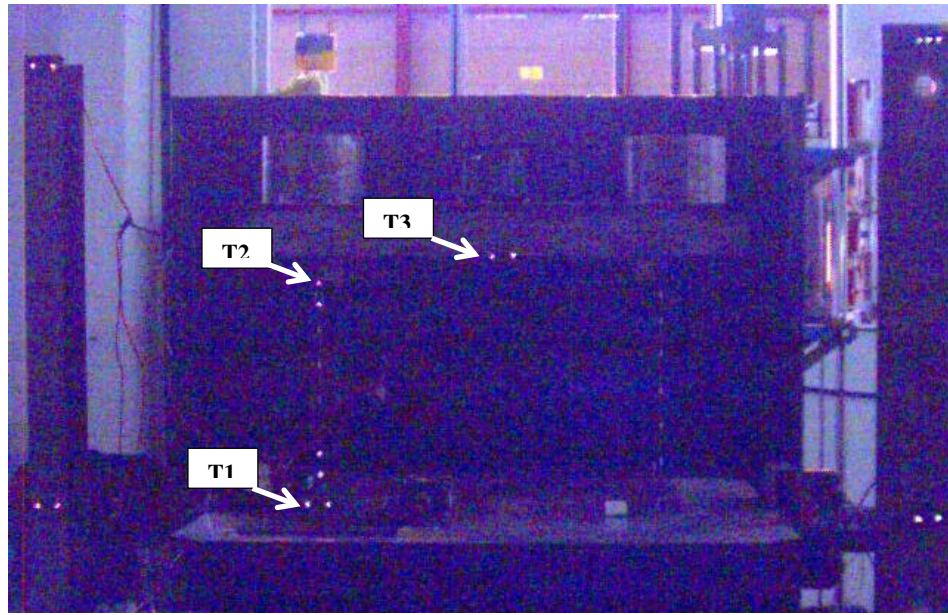


Figure 4. 60 Markers distribution

Then the dynamic experiments are carried out when the shaking table moves with an amplitude of 3mm at frequencies of 2.6Hz, 5Hz, 10Hz, 20Hz. The targets are placed according to Figure 4.60. The results are illustrated in Figure 4.61. In figure 4.61(a), the motion of T2 instead of T3 is given since that the frame is resonated when the input is at 2.6 Hz and therefore the motion of T3 is not able to be correctly tracked due to a too dense distribution of markers. The

results show that there are some noises in the signal, especially when the frequency of motion is high. This can be improved by adopting a higher resolution camera. Nevertheless, according to the achieved results, one can say the implemented system can successfully track the motion of the target markers.

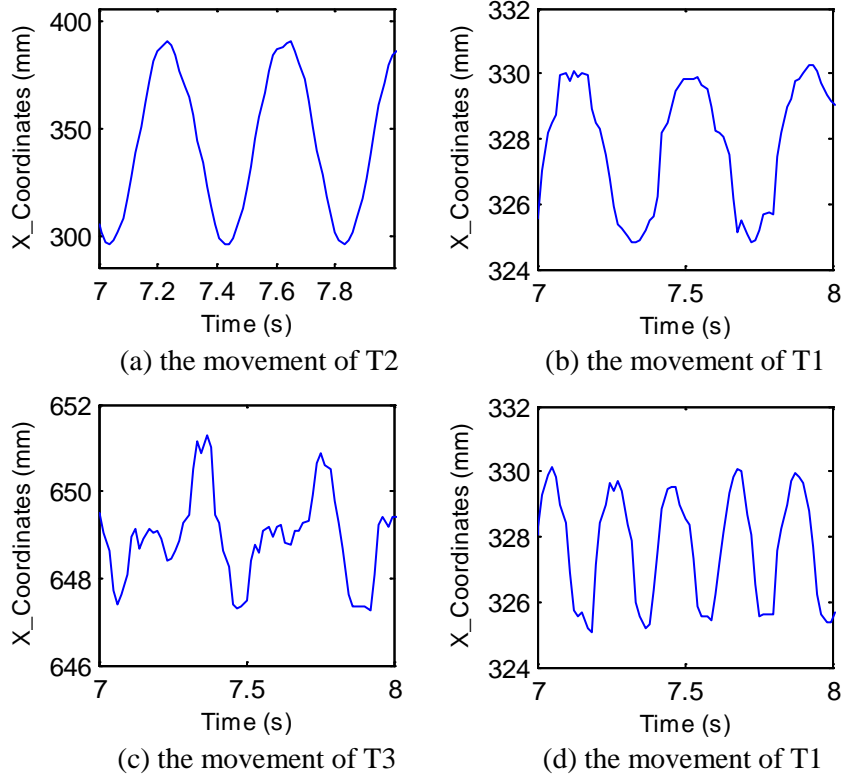
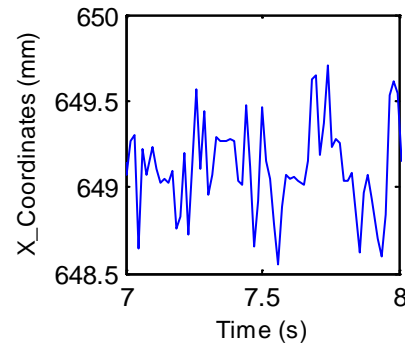
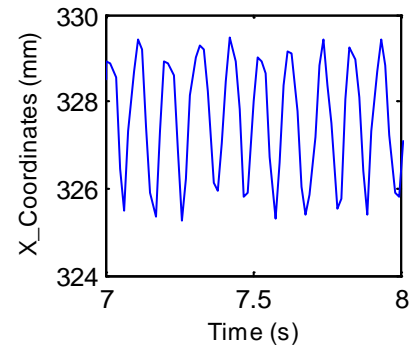


Figure 4.61 Track results (to be continued)

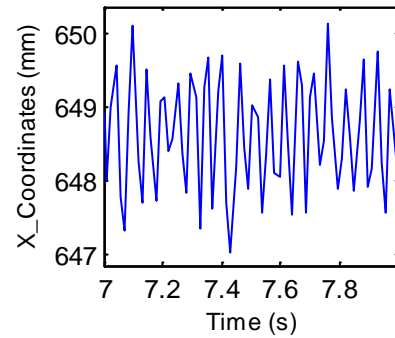
(a), (b) results at 2.6Hz excitation signal; (c), (d) results at 5Hz excitation signal;



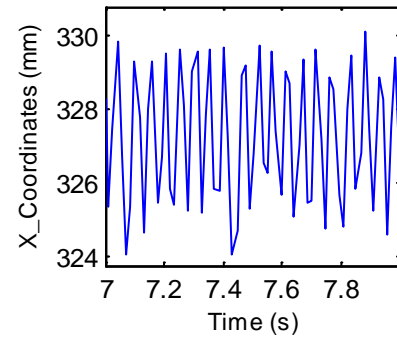
(e) the movement of T3



(f) the movement of T1



(g) the movement of T3

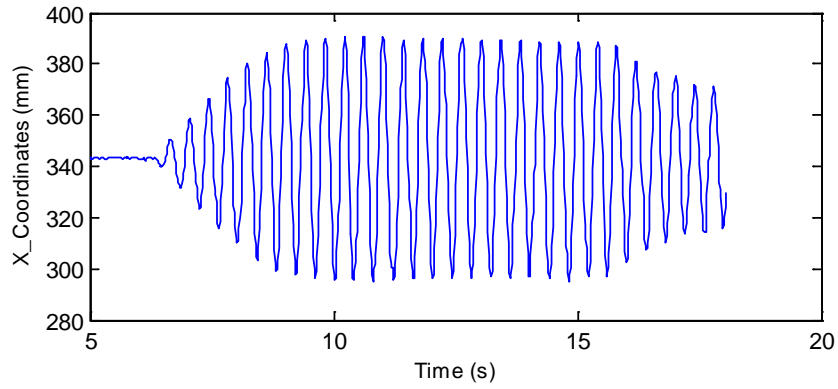


(h) the movement of T1

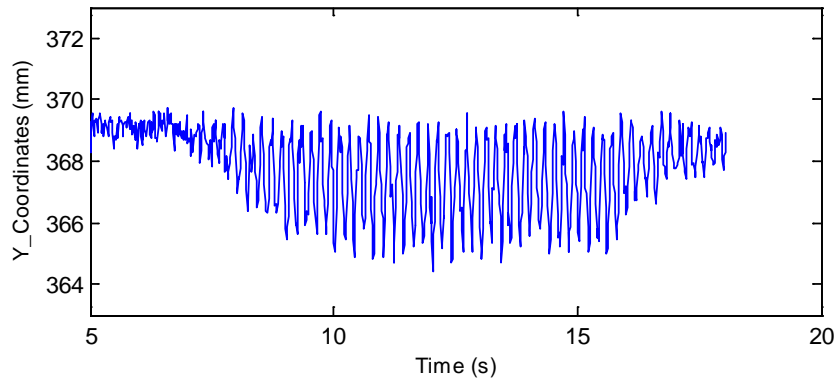
Figure 4. 61 Track results (continued)

(e), (f) results at 10Hz excitation signal; (g), (h) results at 20Hz excitation signal

When the excitation signal is at 2.6Hz, the frame resonates. Figure 4.62 shows the movement of T2. One can read that the displacement in vertical direction is about 4.5mm and its frequency is twice of the one of the movement in horizontal direction.



(a) movements of T2 in the horizontal direction



(b) movements of T2 in the vertical direction

Figure 4. 62 The movements of T2 (a) the horizontal direction (b) the vertical direction.

Chapter 5 Conclusions and Future Directions

In this thesis, three non-contact displacement measurement systems for structural health monitoring are studied.

The first system is the global positioning system, which is broadly selected as the optimal solution of displacement measurement technology in view of a long-term SHM system. The problem is that GPS is only effective in open area and therefore it requires a visible sky position to place its antenna but a roofed position to place its receiver and the power supply. Presently, the connection between the receiver and the control display unit available on the market is of the wired type. But sometimes, it is difficult to route cables due to the building architectural constraints. Therefore, a wireless data logger would greatly facilitate the setup and using of GPS receivers. The power cable is also disturbing the installation. Therefore, a wireless link based on the low power consumption transceiver, CC1110, was developed at the University of Pavia specifically as cable-replacement. Experiment results show a successful cable-replacement solution which supports the GPS sample rate up to 5Hz. That sample frequency is high enough, since normally the GPS is utilized for monitoring high-rise buildings or large-span bridges which behaves as low-pass filters. According to the analysis of power consumption of the different components, the wireless unit possesses the feature of low power consumption. Possibility of recharging the battery through power harvesting technologies ensures the feasibility of this wire-replacement solution.

Since the GPS system requires an open sky for the antenna in order to receive signals from an adequate number of satellites, it cannot be used for displacement measurement inside a covered space. Laser-based and vision-based local positioning systems are potential alternatives for these applications and they were chosen as subjects for further studies.

The second system is based on a laser sensor, YT89MGV80. Elaborations were designed and implemented to construct a high performance wireless laser sensor. It is first constructed utilizing the laboratory-designed wireless data acquisition system based on CC1110 transceiver. Despite this system works properly when the motion of monitored object is significant, there are noises at spurious

frequencies which affect the successful measurement of small motion (Casciati and Wu 2013). Experiment results shows that those spurious frequencies noises are introduced mainly by the wireless data acquisition system. Therefore, an updated version of wireless data acquisition system was designed with the separation of analogue and digital ground. Experiment results show that there are no longer spurious-frequencies noises in the new system and the noise floor of the system is greatly reduced compared to the first version. By now, the noise in this wireless laser sensor is mainly contributed by the laser sensor, YT89MGV80. These noises include both temperature-drift noise and electric-circuit-thermal noise. Methodologies are proposed to improve the accuracy of this sensor, including temperature drift compensation, moving average filtering, Gaussian filtering, and spectral subtraction. Experiment results show that those methodologies greatly improve the accuracy of the wireless laser sensor. Compared to the moving average filtering and to the Gaussian filtering, the spectral subtraction methodology seems to provide the better performance.

The last studied system is a two-dimension vision-based displacement sensor. Actually, two vision systems were set up to monitor the motion of a scale-reduced model in the laboratory test. The feasibility of displacement measurements based on vision system is primarily validated by utilizing the system to monitor the movement of a three-story frame which is installed on a shaking table. However, the camera must be calibrated to enable its measurement to represent the actual movement. In general, a rough calibration is performed through estimating the scale factor of the image via a ruler or a known size object. This method does not account for either the projection distortion or the camera distortion. Therefore, two methods, image registration and 2D direct linear transformation, are studied to solve these problems. Experiment results show that the 2D direct linear transformation has a much better performance than the traditional scale factor based methodology especially when the optical of the camera is skewed with the image. To examine the dynamic performance, the vision-based displacement measurement system is employed to capture the high frequencies motions. Experiment results demonstrate a successful capture. Several commonly concerned topics are also discussed, such as the dependence of marker density and the influence of choosing different exposure periods.

There are still a large amount of work to be done in this area in the future, including multi-camera vision system, 3D camera calibration, field experiments, system automation and wireless communication for the camera device.

Bibliography

- Accusoft. (2012). "ImageGear medical DICOM medical imaging SDK." Retrieved 14, September, 2012 from <http://www.accusoft.com/ig-medicalfeatures.htm>.
- Ampeliotis, D., N. Bogdanović, et al. (2012). "Power-efficient wireless sensor reachback for SHM." Bridge Maintenance, Safety, Management, Resilience and Sustainability. B. Frangopol. London, Taylor & Francis Group: 219-226.
- Applebaum, S. (1976). "Adaptive arrays." IEEE Transactions on Antennas and Propagation, **24**(5): 585-598. September 1976.
- Ashburner, J. (2012). "Image registration." Retrieved 15, September, 2012 from <http://www.slideserve.com/boyce/image-registration-john-ashburner>.
- Barnes, J. and C. Rizos (2007). "Long term performance analysis of a new ground-transceiver positioning network (LocataNet) for structural deformation monitoring applications." Strategic Integration of Surveying Service, FIG Working week, 2007. Hong Kong SAR, China.
- Barnes, J., C. Rizos, et al. (2003). "High precision indoor and outdoor positioning using LocataNet." Journal of Global Positioning Systems. Vol. 2, No. 2: 73-82
- Barnes, J. B. and J. Van Cranenbroeck (2006). "The potential of a ground based transceivers network for water dam deformation monitoring." Dams and Reservoirs, Societies and Environment in the 21st Century, Vols 1 and 2: 1037-1045.
- Boll, S. (1979). "Suppression of acoustic noise in speech using spectral subtraction." IEEE Transactions on Acoustics, Speech and Signal Processing, **27**(2): 113-120.
- Cambridge in colour. (2013). "Understanding camera lenses." Retrieved 14, March, 2013, from <http://www.cambridgeincolour.com/zh-hans/tutorials/bcamera-lenses.htm>.
- Casciati, F., L. Faravelli, et al. (2012). "Structural diagnostic via compressive sensing." Bridge Maintenance, Safety, Management, Resilience and Sustainability. B. Frangopol. London, Taylor & Francis Group: 227-231.
- Casciati, F. and C. Fuggini (2008). "Monitoring an Industrial Steel Building by GPS Receivers." Proceedings of the Fourth European Workshop on Structural Health Monitoring, Cracow, Poland, July 2-4, 2008.

- Casciati, F. and C. Fuggini (2009). "Engineering vibration monitoring by GPS: long duration records." *Earthquake Engineering and Engineering Vibration* **8**(3): 459-467.
- Casciati, F. and C. Fuggini (2011). "Monitoring a steel building using GPS sensors." *Smart Structures and Systems* **7**(5): 349-363.
- Casciati, F. and R. Rossi (2007). "A power harvester for wireless sensing applications." *Structural Control & Health Monitoring* **14**(4): 649-659.
- Casciati, F. and L. J. Wu (2010). "Investigating the potential of LPS in structural mechanics." *The 10th International Conference on Motion and Vibration Control*. Tokyo, Japan.
- Casciati, F. and L. J. Wu (2011a). "A non-contact displacement measurement system based on vision system." *International Symposium on Innovation & Sustainability of Structures in Civil Engineering*. XiaMen, China.
- Casciati, F. and L. J. Wu (2011b). "The Wireless Issue in Positioning Systems." *Proceedings of Eurodyn 2011*. Louvain, Belgium.
- Casciati, F. and L. J. Wu (2013). "Local positioning accuracy of laser sensors for structural health monitoring." *Structural Control and Health Monitoring* **20**(5): 728-739.
- Casciati, S., L. Faravelli, et al. (2009). "Design of a Multi-Channel Real-Time Wireless Connection System for Analog Cable Replacement Application." *Proceedings of the 7th IWSHM*, Stanford, CA USA.
- Casciati, S., L. Faravelli, et al. (2010). "Frequency division multiplexing wireless connection." *6th International Conference on Wireless Communications Networking and Mobile Computing (WICOM2010)*, Chengdu, China.
- Casciati, S., L. Faravelli, et al. (2012). "Energy harvesting and power management of wireless sensors for structural control applications in civil engineering." *Smart Structures and Systems* **10**(3): 299-312.
- CES, W. t. (2012). "WiFi - GPS data logger with WiFi download." Retrieved 16, March, 2013, from <http://www.ceswireless.net/default.htm>.
- Chen, Z. C. (2011). "Structural monitoring and system control using a wireless sensor network." Ph.D. thesis, Department of Structural Mechanics, University of Pavia, Pavia, Italy.
- David, S. (2009). "Method and device for chronologically synchronizing a location network." Japanese Patent JP2009150906, Locata Corporation Pty Ltd.

- De Pasquale, G., G. Bernardini, et al. (2010). "Ambient vibration testing of bridges by non-contact microwave interferometer." *Aerospace and Electronic Systems Magazine*, IEEE 25(3):19-26.
- DecaWave. (2012). "Scensor and Real Time Location Systems (RTLS)." Retrived 15, June, 2012, from <http://www.decawave.com/real-time-location-systems.html>.
- Digi International (2008). "X-CTU Configuration & Test Utility Software User Guide." Retrived 12, December, 2010 from <http://www.digi.com/support/productdetail?pid=3352&osvid=57&type=utilities>
- Du Plessis, J. H. (2008). An all-fibre laser distance measurement system utilising figure-eight fibre lasers with electro-optic amplitude modulation. Master Thesis, Department of Electrical & Electronic Engineering, University of Johannesburg.
- Ellinger, F., R. Eickhoff, et al. (2007). "European project RESOLUTION-local positioning systems based on novel FMCW radar." *Microwave and Optoelectronics Conference*, Brazil.
- Ergen, S. C. (2004). "ZigBee/IEEE 802.15.4 summary." Retrived 10, June, 2010 from <http://www.eecs.berkeley.edu/csinem/academic/publications/zigbee.pdf>.
- Faravelli, L., C. Fuggini, et al. (2010). "Toward a hybrid control solution for cable dynamics: Theoretical prediction and experimental validation." *Structural Control and Health Monitoring* 17(4): 386-403.
- Farrar, C. R. and K. Worden (2007). "An introduction to structural health monitoring." *Philosophical Transactions of the Royal Society a-Mathematical Physical and Engineering Sciences* 365(1851): 303-315.
- Feng, W., J. Li, et al. (2004). Creation of distortion model for digital camera (dmdc) based on 2D DLT. 20th International Society for Photogrammetry and Remote Sensing. O. Altan. Istanbul, Turkey
- Fuggini, C. (2010). Using Satellites Systems for Structural Monitoring: Accuracy, Uncertainty and Reliability. Ph.D. thesis. Department of Structural Mechanics. University of Pavia. Pavia, Italy,
- Fukuda, Y., M. Q. Feng, et al. (2010). "Cost-effective vision-based system for monitoring dynamic response of civil engineering structures." *Structural Control and Health Monitoring* 17(8): 918-936.
- Gao, Y., B. F. Spencer, et al. (2006). "Distributed computing strategy for structural health monitoring." *Structural Control and Health Monitoring* 13(1): 488-507.

- Gentile, C. (2009). "Application of Microwave Remote Sensing to Dynamic Testing of Stay-Cables." *Remote Sensing* **2**(1): 36-51.
- Gentile, C. (2010). "Application of Radar Technology to Deflection Measurement and Dynamic Testing of Bridges." Chapter 8 of *Radar Technology*. Edited by Guy Kouemou, ISBN 978-953-307-029-2, Publisher: InTech. DOI: 10.5772/51712
- Gong, H. (2011). "Study on wireless sensor network for SHM." Master thesis, Department of Communication Engineering, XiaMen, China, XMU.
- González-Aguilera, D., J. Gómez-Lahoz, et al. (2008). "A new approach for structural monitoring of large dams with a three-dimensional laser scanner." *Sensors* **8**(9): 5866-5883.
- Gonzalez, R. C. and R. E. Woods (2002). "Digital image processing(2nd Edition)." Publisher: Prentice Hall, ISBN-10: 0201180758. ISBN-13: 978-0201180756
- Hartley, R. and A. Zisserman (2004). "Multiple view geometry in computer vision(2nd Edition)." Cambridge, Cambridge University Press.
- Hide, C., T. Moore, et al. (2004). "Adaptive Kalman filtering algorithms for integrating GPS and low cost INS." *Position Location and Navigation Symposium*, Monterey, California, April 26-29, 2004
- Hill, J. L. (2003). "System architecture for wireless sensor networks." Ph.D. thesis, Computer Science in the Graduate Division, University of California, Berkeley.
- Houlux. (2013). "M-241 wireless GPS logger." Retrieved 16, March, 2013, from http://www.holux.com/JCore/en/products/products_content.jsp?pno=341.
- Howells, P. (1965). "Intermediate Frequency Side-Lobe Canceller." U. S. . **Patent 3 202 990**.
- Huber, D., M. Krommer, et al. (2009). "Dynamic displacement tracking of a one-storey frame structure using patch actuator networks: Analytical plate solution and FE validation." *Smart Structures and Systems* **5**(6): 613-632.
- Intel. (2012). "Intel® IPP - Open source computer vision library (OpenCV) FAQ." Retrived 14, May, 2012, from <http://software.intel.com/en-us/articles/intel-integrated-performance-primitives-intel-ipp-open-source-computer-vision-library-opencv-faq>.
- Iyer, S. and S. K. Sinha (2005). "A robust approach for automatic detection and segmentation of cracks in underground pipeline images." *Image and Vision Computing* **23**(10): 921-933.

- Jahanshahi, M. R. and S. F. Masri (2012). "Adaptive vision-based crack detection using 3D scene reconstruction for condition assessment of structures." *Automation in Construction* **22**: 567-576.
- Jahanshahi, M. R., S. F. Masri, et al. (2011). "Multi-image stitching and scene reconstruction for evaluating defect evolution in structures." *Structural Health Monitoring* **10**(6): 643-657.
- Jardak, N. and N. Samama (2010). "Short multipath insensitive code loop discriminator." *IEEE Transactions On Aerospace And Electronic Systems* **46**(1).
- Jin-Shyan, L., S. Yu-Wei, et al. (2007). "A comparative study of wireless protocols: Bluetooth, UWB, ZigBee, and Wi-Fi." *Industrial Electronics Society, 2007. IECON 2007. 33rd Annual Conference of the IEEE. Taipei, Taiwan.*
- Jisc Digital Media. (2012). "Digital camera." Retrived 03, March, 2012, from <http://www.jiscdigitalmedia.ac.uk/stillimages/advice/digital-cameras>.
- Jo, H., S. Sim, et al. (2011). "Feasibility of displacement monitoring using low-cost GPS receiver." *Proc. of ASSEM 2011, Seoul, Korea.*
- Johnson, J. B. (1928). "Thermal Agitation of Electricity in Conductors." *Physical Review* **32**(1): 97-109.
- Johnson, T. J., R. L. Brown, et al. (2004). "Distributed structural health monitoring with a smart sensor array." *Mechanical Systems and Signal Processing* **18**(3): 555-572.
- Jurjo, D. L. B. R. (2010). "Identification of structural nonlinear dynamic behavior of flexible metallic columns under the action of self-weight." *Mecánica Computacional, Buenos Aires, Argentina.*
- Jurjo, D. L. B. R., C. Magluta, et al. (2010). "Experimental methodology for the dynamic analysis of slender structures based on digital image processing techniques." *Mechanical Systems and Signal Processing* **24**(5): 1369-1382.
- Kijewski-Correa, T., A. Kareem, et al. (2006). "Experimental Verification and Full-Scale Deployment of Global Positioning Systems to Monitor the Dynamic Response of Tall Buildings." *Journal of Structural Engineering* **132**(8): 1242-1253.
- Kimura, N. and S. Latifi (2005). "A survey on data compression in wireless sensor networks." *International Conference on Information Technology: Coding and Computing, 4-6 April, 2005, Las Vegas, Nevada, USA.*
- Kohut, P. and P. Kurowski (2006). "The integration of vision system and modal analysis for SHM applications." *Proc. Of the IMAC-XXIV a conference and exposition on structural dynamics, St. Louis, USA.*

- Kohut, P. and P. Kurowski (2009). "Application of modal analysis supported by 3D vision-based measurements." *Journal of Theoretical and Applied Mechanics* **47** (4): 855-870.
- Kopparapu, S. K. and M. Satish (2011). "Identifying Optimal Gaussian Filter for Gaussian Noise Removal." Third National Conference on Computer Vision, Pattern Recognition, Image Processing and Graphics (NCVPRIPG). Karnataka, India.
- Krüger, Bahr, et al. (2010). "D3.3 Sensor development and sensor adaption (part 1)." MPA Universität Stuttgart, Germany.
- Kreatit Design, I. (2013). "Wireless data loggers & fleet tracking - GPRS & SMS GSM." Retrieved 16, March, 2013, from <http://www.kreatit.ca/>.
- Krommer, M., Irschik, H., Pichler, U. (2005). "Design of Sensors/Actuators for Structural Control of Continuous CMA Systems." *Proc. of SPIEs 12th Annual International Symposium on Smart Structures and Materials*, March 6-10th, 2005, San Diego, CA, U.S.A., M. Tomizuka, (ed.), *Smart Structures and Materials 2005: Sensors and Smart Structures Technologies for Civil, Mechanical, and Aerospace Systems*, SPIE Vol. 5765, 2005, pp. 130-141.
- Lee, J. and M. Shinozuka (2006). "Real-time displacement measurement of a flexible bridge using digital image processing techniques." *Experimental Mechanics* **46**(1): 105-114.
- Lee, J. J., S. Cho, et al. (2006). "Evaluation of bridge load carrying capacity based on dynamic displacement measurement using real-time image processing techniques." *Steel Structures* **6**: 377-385.
- Lei, Y., C. Liu, et al. (2009). "A new type of intelligent wireless sensing network for health monitoring of large-size structures." Second International Conference on Smart Materials and Nanotechnology in Engineering, Weihai, China
- Lei, Y., L. J. Liu, et al. (2011). "A smart wireless sensor network for structural damage detection." International Symposium on Innovation & Sustainability of Structures in Civil Engineering. XiaMen, China.
- Leica Geosystems AG (2007) "Leica GMX902 GG Streamlined GNSS Monitoring for Critical Structures." Retrived 18, July, 2010. http://www.construlink.com/download_counter.php?Tipo=Catalogo&IdDown=103073&Fich=leica_monitorizacao_estrutural_gmx902_ed2007_2010.pdf
- Leica Geosystems AG (2008) "Leica GPS1200+ user manual." Retrived 3, May, 2011. from http://www.surveyequipment.com/PDFs/GPS1200_User_en.pdf

- Leica Geosystems AG. (2010). "Leica SpiderQC Brochure." Retrived 10, May, 2011. from http://www.leica-geosystems.com/en/downloads-downloads-search_74590.htm?search=true&product=GNSS%20QC%20Software.
- Li, J. (2011). "Real-time crop recognition system for mechanical weeding robot using time-of-flight 3D camera and advanced computation based on field-programmable gate array (FPGA)." Retrived 10, May,2011. from http://class.ece.iastate.edu/cpre583/HW/mini_survey/Crop_recognition.pdf.
- Liao, W. Y. (2012). "Comfort assessment of tower-like slender structures under typhoons and earthquakes." PhD Thesis, Department of Civil and Structural Engineering. Hong Kong, The Hong Kong Polytechnic University.
- Locata (2012). "Locata technology brief." Retrived 10, May, 2012. From <http://locata.com/technology/technical-papers/>
- Lockhart, R. W. (2013, March, 2013). "How Much ADC Resolution Do You Really Need?", Retrived 10, November, 2012. from <http://www.dataq.com/applicat/articles/adc-resolution.html>.
- logicchild. (2009). "Object-oriented programming using MFC." Retrived 10, June, 2012. from <http://www.codeproject.com/Articles/35300/Object-oriented-Programming-Using-MFC>.
- Lynch, J. P. (2002). "Decentralization of wireless monitoring and control technologies for smart civil structures." Ph.D. thesis, The department of civil and environmental engineering, Stanford University.
- Lynch, J. P. and K. J. Loh (2006). "A summary review of wireless sensors and sensor networks for Structural Health Monitoring." *The Shock and Vibration Digest* **38** (2): 91–128.
- Lynch, J. P., A. Sundararajan, et al. (2003). "Field validation of a wireless structural monitoring system on the Alamosa Canyon Bridge." *Smart Structures and Materials 2003: Smart Systems and Nondestructive Evaluation for Civil Infrastructures* **5057**: 267-278.
- Marcelloni, F. and M. Vecchio (2008). "A simple algorithm for data compression in wireless sensor networks." *Communications Letters, IEEE* **12**(6): 411-413.
- Martin, R. (1994). "Spectral Subtraction Based on Minimum Statistics." *Proc. EUSIPCO 94*: 1182-1185.
- Materazzi, A. L. and F. Ubertini (2011). "Eigenproperties of suspension bridges with damage." *Journal of Sound and Vibration* **330**(26): 6420-6434.

- MaxStream, I. (2006) "XStream OEM RF Module - Product Manual v5.x00." Retrived 10, October, 2010 from ftp://ftp1.digi.com/support/documentation/productmanual_xstream_oem_rfmodule_v5.x00.pdf
- mediaCybernetics. (2012). "Image Pro Plus Software Development Kit (SDK)." Retrived 3, October, 2011 from http://www.mediacy.com/index.aspx?page=IPP_SDK.
- Meyer, J., R. Bischoff, et al. (2010). "Wireless sensor networks for long-term structural health monitoring." *Smart Structures and Systems* **6**(3): 263-275.
- Micronas. (2006). "Cypher 7108." 2012, Retrived September, 2012 from http://www.edom.com.tw/vender/product/Cypher7108_product_info_A4.pdf.
- Mohammad Nejad, S. and S. Olyaei (2006). "Comparison of TOF, FMCW and phase-shift laser range-finding methods by simulation and measurement." *Journal of Technology of Education* **1**(1): 11-18.
- Nagayama, T., B. F. Spencer, et al. (2009). "Autonomous decentralized structural health monitoring using smart sensors." *Structural Control and Health Monitoring* **16**(7-8): 842-859.
- Nanotron. (2012). "Product overview." Retrived 3, October, 2012, from http://www.nanotron.com/EN/PR_find.php.
- Ni, Y. Q., Y. Chen, et al. (2002). "Neuro-control of cable vibration using semi-active magneto-rheological dampers." *Engineering Structures* **24**(3): 295-307.
- Ni, Y. Q., W. Y. Liao, et al. (2013). "A vision system for long-distance remote monitoring of dynamic displacement: experimental verification on a supertall structure." *Computer-Aided Civil and Infrastructure Engineering* (in review).
- Ni, Y. Q., K. Y. Wong, et al. (2011). "Health checks through landmark bridges to sky-high structures." *Advances in Structural Engineering* **14**(1): 103-119.
- Nyquist, H. (1928). "Thermal Agitation of Electric Charge in Conductors." *Physical Review* **32**(1): 110-113.
- Olaszek, p. (1999). "Investigation of the dynamic characteristic of bridge structures using a computer vision method." *Measurement* **25**: 227-236.
- OMRON. (2013). "OMRON Laser Displacement Sensor Z4M." Retrived 3, March, 2013, from <http://omronkft.hu/>.
- Otsu, N. (1979). "A threshold selection method from gray-level histograms." *IEEE Transactions on Systems, Man and Cybernetics* **9**(1): 62-66.

- Pakzad, S., G. Fenves, et al. (2008). "Design and implementation of scalable wireless sensor network for structural monitoring." *Journal of Infrastructure Systems* **14**(1): 89-101.
- Park, J.-W., J.-J. Lee, et al. (2010). "Vision-based displacement measurement method for high-rise building structures using partitioning approach." *NDT & E International* **43**(7): 642-647.
- Paulauskas, V. and A. Rackauskas (1989). "Approximation theory in the central limit theorem : exact results in Banach spaces." Kluwer Academic.
- Plessis, J. H. d. (2008). "An all-fibre laser distance measurement system utilizing figure-eight fibre lasers with electro-optic amplitude modulation." Master thesis, The University of Johannesburg, The University of Johannesburg.
- Polytec. (2012). "OFV-5000 modular vibrometer controller." Retrived 3,December, 2012, from <http://www.polytec.com/us/products/vibration-sensors/single-point-vibrometers/modular-systems/ofv-5000-modular-vibrometer-controller/>.
- Ramin, S. A. and Z. M. S. Helmi (2009). "Mass structure deformation monitoring using low cost differential Global Positioning System Device." *American Journal of Applied Sciences* **6**(1): 152-156.
- Rice, J. A. and B. F. Spencer (2009). "Flexiblesmart sensor framework for autonomous full-scale Structural Health Monitoring." NSEL Report Series, Newmark Structural Engineering Laboratory.
- Rizos, C. and B. Li (2011). "Independent testing of Locata: a new high accuracy Indoor Positioning Systems." *ION GNSS 2011*. Portland, Oregon, USA.
- Rizos, C., G. Roberts, et al. (2011). "Locata: A new high accuracy indoor positioning system." *International Conference on Indoor Positioning and Indoor Navigation (IPIN)*. Zürich, Switzerland.
- Robinson, F. N. H. (1962). "Noise in Electrical Circuits." London, Oxford University Press.
- Schoeftner, J. and M. Krommer (2012). "Single point vibration control for a passive piezoelectric Bernoulli-Euler beam subjected to spatially varying harmonic loads." *Acta Mechanica* **223**(9): 1983-1998.
- Schreier, R., J. Silva, et al. (2005). "Design-oriented estimation of thermal noise in switched-capacitor circuits." *IEEE Transactions on Circuits and Systems I: Regular Papers*, **52**(11): 2358-2368.
- Smith, S. W. (1997). "The Scientist and Engineer's Guide to Digital Signal Processing." California Technical Publishing.

- Solomon, G. R., B. R. Wagealla, et al. (2002). "GPS data logger with automatic wireless download." U. States. United States, Axiom Navigation, Inc., Anaheim, CA(US). **US 6,408,233 B1**: 5.
- Swartz, R. and J. Lynch (2009). "Strategic network utilization in a wireless structural control system for seismically excited structures." *Journal of Structural Engineering* **135**(5): 597-608.
- Sysbyte Telecom INC. . (2013). "Wireless datalogger." Retrieved 16, March, 2013 from <http://www.sysbyte.com/wdl/index.htm>.
- Texas Instruments (2007). "CC1110fx. " Retrieved 16, March. 2012 from <http://www.ti.com/>.
- The Institute of Electrical and Electronics Engineers, I. (2012). "IEEE 802.15 WPAN low rate alternative PHY Task Group 4a (TG4a) " Retrieved October, 2012, from <http://www.ieee802.org/15/pub/TG4a.html>.
- Trimble Navigation Limited. (2012). "Trimble AP10 GNSS-Inertial OEM system." Retrieved October, 2012 from http://www.trimble.com/gnss-inertial/pdf/AP10_DS_0312.pdf.
- Ubertini, F. (2010). "Prevention of suspension bridge flutter using multiple tuned mass dampers2010." *Wind & Structures* **13**: 235–256.
- Ubertini, F. (2013). "On damage detection by continuous dynamic monitoring in wind-excited suspension bridges." *Meccanica* **48**(5): 1031-1051.
- Uhl, T., P. Kohut, et al. (2009). "Static and dynamic optical measurement in SHM of civil structures." *Structural Health Monitoring 2009: From System Integration to Autonomous Systems*, Proc. of 7th Int'l Workshop on Structural Health Monitoring, Stanford, DEStech Publications, Inc. .
- Uhl, T., P. Kohut, et al. (2011). "Vision based condition assessment of structures." *Journal of Physics: Conference Series* **305**: 012043.
- Vervisch-Picois, A. and N. Samama (2009). "Interference mitigation in a repeater and pseudolite Indoor Positioning System." *IEEE Journal of Selected Topics in Signal Processing*, **3**(5): 810-820.
- Virag, N. (1999). "Single channel speech enhancement based on masking properties of the human auditory system." *IEEE Transactions on Speech and Audio Processing*, **7**(2): 126-137.
- Waddi, S. K., P. C. Pandey, et al. (2013). "Speech enhancement using spectral subtraction and cascaded-median based noise estimation for hearing impaired listeners." *Communications (NCC), 2013 National Conference on w Delhi, India*.

- Wahbeh, A. M., J. P. Caffrey, et al. (2004). "Direct measurement of displacements in vibrating structures through vision-based approaches." *Emirates Journal for Engineering Research* **2**(9): 6.
- Walton, J. S. D. (1981). "Close-range cine-photogrammetry: a generalized technique for quantifying gross human motion." Ph.D. thesis, Pennsylvania State University.
- Wang, Y. (2007). "Wireless sensing and decentralized control for civil structures: theory and implementation." Ph.D. thesis, The Department Of Civil And Environmental Engineering, Stanford University.
- Wang, Y., J. P. Lynch, et al. (2007). "A wireless structural health monitoring system with multithreaded sensing devices: design and validation." *Structure and Infrastructure Engineering* **3**(2): 103-120.
- Wang, Y. S. and X. P. Xu (2003). "Realization of laser range finding based on phase." *Journal of Beijing University of Technology* **29**(4): 424-427.
- Weng, J., P. Cohen, et al. (1992). "Camera calibration with distortion models and accuracy evaluation." *IEEE Transactions on Pattern Analysis and Machine Intelligence*, **14**(10): 965-980.
- Widrow, B., J. R. Glover, Jr., et al. (1975). "Adaptive noise cancelling: Principles and applications." *Proceedings of the IEEE* **63**(12): 1692-1716.
- Wieger, G., and J. M. Caicedo (2009). "Computer vision method for displacement measurements of large-scale civil structures." XXVII International Modal Analysis Conference. Orlando, Florida.
- Wong, K.-Y. and Y.-Q. Ni (2009). "Modular Architecture of SHM System for Cable-Supported Bridges." *Encyclopedia of Structural Health Monitoring*, John Wiley & Sons, Ltd.
- Yang, Y. B., Y. C. Li, et al. (2012). "Using two connected vehicles to measure the frequencies of bridges with rough surface: a theoretical study." *Acta Mechanica* **223**(8): 1851-1861.
- You-Chiun, W., H. Yao-Yu, et al. (2009). "Multiresolution spatial and temporal coding in a wireless sensor network for long-term monitoring applications." *IEEE Transactions on Computers*, **58**(6): 827-838.
- Zitová, B. and J. Flusser (2003). "Image registration methods: a survey." *Image and Vision Computing* **21**(11): 977-1000.